



TRAO Survey of Nearby Filamentary Molecular Clouds, the Universal Nursery of Stars (TRAO-FUNS). III. Filaments and Dense Cores in the NGC 2068 and NGC 2071 Regions of Orion B

Hyunju Yoo^{1,2}, Chang Won Lee^{2,3}, Eun Jung Chung¹, Shinyoung Kim², Mario Tafalla⁴, Paola Caselli⁵, Philip C. Myers⁶, Kyoung Hee Kim⁷, Tie Liu⁸, Woojin Kwon^{9,10}, Archana Soam^{11,12}, and Jongsoo Kim²

¹Department of Astronomy and Space Science, Chungnam National University, 99 Daehak-ro, Yuseong-gu, Daejeon 34134, Republic of Korea
hyunju527@gmail.com

²Korea Astronomy and Space Science Institute, 776 Daedeokdae-ro, Yuseong-gu, Daejeon 34055, Republic of Korea

³University of Science and Technology, Korea (UST), 217 Gajeong-ro, Yuseong-gu, Daejeon 34113, Republic of Korea

⁴Observatorio Astronómico Nacional (IGN), Alfonso XII 3, E-28014 Madrid, Spain

⁵Max-Planck-Institut für Extraterrestrische Physik, Gießenbachstrasse 1, D-85748 Garching bei München, Germany

⁶Harvard-Smithsonian Center for Astrophysics, 60 Garden Street, Cambridge, MA 02138, USA

⁷The Korea Astronomy Society, 776, Daedeok-daero, Yuseong-gu, Daejeon, Republic of Korea

⁸Key Laboratory for Research in Galaxies and Cosmology, Shanghai Astronomical Observatory, Chinese Academy of Sciences, 80 Nandan Road, Shanghai 200030, People's Republic of China

⁹Department of Earth Science Education, Seoul National University, 1 Gwanak-ro, Gwanak-gu, Seoul 08826, Republic of Korea

¹⁰SNU Astronomy Research Center, Seoul National University, 1 Gwanak-ro, Gwanak-gu, Seoul 08826, Republic of Korea

¹¹Indian Institute of Astrophysics, II Block, Koramangala, Bengaluru 560034, India

¹²SOFIA Science Center, Universities Space Research Association, NASA Ames Research Center, Moffett Field, CA 94035, USA

Received 2022 November 25; revised 2023 August 3; accepted 2023 August 17; published 2023 November 3

Abstract

We present the results of molecular line observations performed toward the NGC 2068 and NGC 2071 regions of the Orion B cloud as the TRAO-FUNS project to study the roles of the filamentary structure in the formation of dense cores and stars in the clouds. Gaussian decomposition for the C¹⁸O spectra with multiple velocity components and the application of a friends-of-friends algorithm for the decomposed components allowed us to identify a few tens of velocity-coherent filaments. We also identified 48 dense cores from the observations of N₂H⁺ using a core finding tool, FellWalker. We performed a virial analysis for these filaments and dense cores, finding that the filaments with N₂H⁺ dense core are thermally supercritical, and the filaments with a larger ratio between the line mass and the thermal critical line mass tend to have more dense cores. We investigated the contribution of the nonthermal motions in dense cores and filaments, showing the dense cores are mostly in transonic/subsonic motions while their natal filaments are mostly in supersonic motions. This may indicate that gas turbulent motions in the filaments have been dissipated at the core scale to form the dense cores there. The filaments with (dynamically evolved) dense cores in infalling motions or with NH₂D bright (or chemically evolved) dense cores are all found to be gravitationally critical. Therefore, the criticality of the filament is thought to provide a key condition for its fragmentation, the formation of dense cores, and their kinematical and chemical evolution.

Unified Astronomy Thesaurus concepts: [Interstellar medium \(847\)](#); [Interstellar filaments \(842\)](#); [Molecular clouds \(1072\)](#); [Star formation \(1569\)](#); [Radio astronomy \(1338\)](#)

Supporting material: data behind figure, figure sets, interactive figure, machine-readable tables

1. Introduction

The prevalence of morphologically elongated structures, so-called filament, has been discovered over a wide range of spatial scales and is generally accepted as a key feature of star formation. According to observations at infrared/submillimeter wavelengths, the interstellar molecular clouds are found to be composed of a network of filamentary structures (André et al. 2010, 2014; Men'shchikov et al. 2010; Molinari et al. 2010; Arzoumanian et al. 2011; Hacar & Tafalla 2011; Hacar et al. 2013, 2018; Arzoumanian et al. 2019). Especially, recent observational facilities (e.g., Herschel Space Observatory, and Atacama Large Millimeter/submillimeter Array) have been expanding the horizon for understanding star formation in the early phase and have provided opportunities to study the relationship between

diffuse filamentary structures and dense cores in-depth (André et al. 2010; Hacar et al. 2018). Analytic approaches have advocated that the formation of filamentary structure in the diffuse medium is a spontaneous phenomenon (Padoan et al. 2001; Gómez & Vázquez-Semadeni 2014; Wareing et al. 2016). Although the importance of filaments in star-forming regions has been emphasized by many observations and numerical simulations in recent years, the role of filamentary structures in the formation of dense cores and/or stars and the formation process of filaments themselves are still debated. The main difficulty in understanding the structure and physical properties of filaments arises from the fact that we are looking at the complexity of the three-dimensional organization of molecular clouds along the line of sight. Even if we spatially resolve the small-scale structure of the molecular cloud with high angular resolution, we still need spectroscopic information to distinguish the multiple components with different velocities overlapped in the line of sight from optically thin molecular line emission. Spatially and spectroscopically adequate observations are highly required for

improving our understanding of the dense core and star formation in filamentary clouds.

The Orion B molecular cloud is the most suitable place to study both ongoing low- and high-mass star formation since it contains not only various evolutionary stages of young stellar objects (YSOs) but also massive stars. Furthermore, its relatively close distance (~ 423 pc; Menten et al. 2007; Zucker et al. 2019) allows us to have less contamination from foreground materials than other massive star-forming clouds.

The large-scale structures of Orion B have been revealed from molecular line observations. In the early studies, the bulk of the molecular gas with CO emission peaks has been shown. However, the velocity gradients and the detailed small-scale gas distribution within substructures have not been resolved due to low spatial and spectral resolution (Kutner et al. 1977; Maddalena et al. 1986; Bally et al. 1991; Wilson et al. 2005). Molecular gas surveys with higher resolution have been carried out to investigate the kinematics and distribution of condensed structures. Lada et al. (1991) identified clumpy substructures and provided a census of dense cores from an unbiased CS (2–1) survey with 1.7 resolution. Dense cores have also been found in the dense gas tracer H^{13}CO^+ (Aoyama et al. 2001; Ikeda et al. 2009; Walker-Smith et al. 2013) and the core properties were listed at the submillimeter regime (Johnstone et al. 2001; Mitchell et al. 2001; Motte et al. 2001; Kirk et al. 2016). The survey observations in the CO isotopologues (Buckle et al. 2010; Walker-Smith et al. 2013; Nishimura et al. 2015) revealed that the Orion B molecular cloud is composed of filamentary structures in the form of overdense gas.

A large-scale molecular line survey has been carried out to map over 1.9 deg^2 around the NGC 2023 and NGC 2024 regions in the Orion B molecular cloud with the IRAM 30 m telescope in the context of the ORION B project (Pety et al. 2017). Among their various molecular transitions observed at the 3 mm wavelength band, Orkisz et al. (2019) used $\text{C}^{18}\text{O}(1-0)$ integrated intensity map to search for a network of filaments and study the kinematical properties and statistical characteristics of the filaments in the NGC 2023 and NGC 2024 regions. We note that the region observed by Pety et al. (2017) is the southern part of the Orion B complex (i.e., L1630N) and the target region for this paper is the northern part of the Orion B, which includes two bright reflection nebulae NGC 2068 and NGC 2071 (see overview by Bally 2008; Gibb 2008 and references therein).

Using the extensive imaging from the Herschel Gould Belt Survey, Schneider et al. (2013) obtained a probability distribution function (PDF) from the column density map and presented that the PDF of Orion B (covering both NGC 2023/24 and NGC 2068/71) shows a log-normal distribution with a power-law tail at a high column density range. They explained that the existence of the power-law tail may be caused by the global gravitational collapse of large covering areas like filaments and ridges. Based on the column density map at $18''2$ angular resolution, Könyves et al. (2020) identified filament networks in Orion B and presented the distributions of dense cores.

As highlighted in Hacar et al. (2013), however, the spectral information from optically thin molecular lines (e.g., $\text{C}^{18}\text{O}(1-0)$) is required to reveal multiple velocity components overlapped along the line of sight. Even the filaments identified by the Herschel continuum image in high spatial resolution can reveal the detailed structure of the molecular cloud; however,

they suffer from a lack of information on kinematic properties and thus in some cases multiple identities overlap the line of sight. Therefore, it is essential to present spectroscopic observations toward Orion B in part to explore complex gas kinematics in the three-dimensional position-position-velocity (PPV) space, and also to study evolutionary signatures in Orion B. In this paper, we present the physical properties of the filamentary structures identified by the $\text{C}^{18}\text{O}(1-0)$ line and dense cores defined from $\text{N}_2\text{H}^+(1-0)$ emission.

This paper is organized as follows. We summarize the previous studies on the observing regions in Section 1 and describe the observation and data reduction in Section 2. The results of the identification and physical properties of filaments and dense cores are given in Section 3. We discuss the kinematic and chemical properties of filaments and dense cores in Section 4 and provide a summary of the study in Section 5.

2. Observation and Data Reduction

2.1. TRAO-FUNS Survey

The mapping observations toward the star-forming molecular cloud of Orion B were carried out using the multibeam receiver SEcond QUabbin Observatory Imaging Array (SEQUOIA) of the Taeduk Radio Astronomy Observatory (TRAO),¹³ which is a 14 m single-dish radio telescope located in South Korea. The receiver SEQUOIA-TRAO is equipped with 16-pixel Monolithic Microwave Integrated Circuit preamplifiers in a 4×4 array and provides an observing frequency range of 85–115 GHz. The backend system, a fast Fourier transform spectrometer, has 8192 channels with a spectral resolution of ~ 15 kHz, which corresponds to a velocity resolution of $\sim 0.04 \text{ km s}^{-1}$ at 110 GHz and a full spectral bandwidth of ~ 60 MHz. The narrow-band second IF modules enable the observation of two frequencies simultaneously within the 85–100 or 100–115 GHz bands. The main beam efficiencies of the telescope are 0.48 at 98 GHz, and 0.46 at 110 GHz, respectively (Jeong et al. 2019). The observations were made from 2016 December to 2018 October as part of the TRAO Key Science Program, TRAO Survey of Nearby Filamentary Molecular clouds, and the Universal Nursery of Stars (TRAO-FUNS).

In order to investigate the physical properties and the chemical characteristics of the dense cores and surrounding filamentary structures in Orion B, including two reflection nebulae (NGC 2071 and NGC 2068), we selected eight molecular lines; $^{13}\text{CO}(1-0)$, $\text{C}^{18}\text{O}(1-0)$, $\text{N}_2\text{H}^+(1-0)$, ortho- $\text{NH}_2\text{D}(1_{11}-1_{01})$, CS (2–1), SO (3_2-2_1), $\text{HCO}^+(1-0)$, and $\text{H}^{13}\text{CO}^+(1-0)$. $^{13}\text{CO}(1-0)$ and $\text{C}^{18}\text{O}(1-0)$ lines were chosen to trace the distribution of molecular gas in the star-forming interstellar molecular cloud. Systematic observations of CS (2–1) and $\text{HCO}^+(1-0)$ lines were performed to examine the evidence of infall motion in dense cores. The $\text{N}_2\text{H}^+(1-0)$ and $\text{H}^{13}\text{CO}^+(1-0)$ lines can be used to determine the systemic velocities of the dense cores since they are usually optically thin. Furthermore, SO (3_2-2_1) and ortho- $\text{NH}_2\text{D}(1_{11}-1_{01})$ were selected to test the chemical state of the dense cores. The observational details including the rest frequency, FWHM beam size, observing area, pixel size, channel width, and rms noise level for each transition are given in Table 1.

¹³ <https://radio.kasi.re.kr/trao/>

Table 1
Information on TRAO Observations

Molecular Line	Frequency (GHz)	θ_B (arcsec)	Area (deg ²)	Pixel Size (arcsec)	Δv (km s ⁻¹)	RMS (K)	RMS _{m0} (K km s ⁻¹)	n_{crit} (cm ⁻³)
(1)	(2)	(3)	(4)	(5)	(6)	(7)	(8)	(9)
ortho-NH ₂ D (1 ₁₁ -1 ₀₁)	85.9262780	57.0	0.106	22	0.1	0.049	0.031	6.5×10^4
H ¹³ CO ⁺ (1-0)	86.7542884	56.6	0.106	22	0.06	0.067	0.026	6.2×10^4
HCO ⁺ (1-0)	89.1885247	55.6	0.559	22	0.06	0.069	0.041	6.8×10^4
N ₂ H ⁺ (1-0)	93.1737637	54.1	0.559	22	0.1	0.053	0.034	6.1×10^4
CS (2-1)	97.9809533	52.4	0.394	22	0.06	0.068	0.037	1.3×10^5
SO (3 ₂ -2 ₁)	99.2998700	51.9	0.394	22	0.1	0.053	0.036	1.9×10^3
C ¹⁸ O (1-0)	109.7821734	48.7	1.365	22	0.1	0.114	0.075	1.9×10^3
¹³ CO (1-0)	110.2013543	48.6	1.365	22	0.1	0.109	0.064	3.5×10^5

Note. Column 1: the molecular line transition. Column 2: the rest frequencies are from Lovas (2004) for ¹³CO (1-0), Pickett et al. (1998) for SO (3₂-2₁), Lee et al. (2001) for C¹⁸O (1-0), N₂H⁺ (1-0), and CS (2-1). We refer to Müller et al. (2001) for HCO⁺ (1-0), ortho-NH₂D (1₁₁-1₀₁), and H¹³CO⁺ (1-0). Column 3: the half-power beamwidth (HPBW). Column 4: the total area of the observed region. Column 5: the pixel size in arcsec. Column 6: the velocity channel width. Columns 7 and 8: the noise levels of the data cubes and integrated intensity maps, respectively, in T_A^{*}. Column 9: the critical densities are from Wielen et al. (2021) for ortho-NH₂D (1₁₁-1₀₁), Shirley (2015) for H¹³CO⁺ (1-0), HCO⁺ (1-0), N₂H⁺ (1-0), and CS (2-1), and Chung et al. (2021) for SO (3₂-2₁), C¹⁸O (1-0), and ¹³CO (1-0).

On-the-fly (OTF) mapping observations were carried out and shown in the regions marked in Figure 1 with the Herschel 250 μm continuum (André et al. 2010; HGBS Team 2020) on the background, making the telescope system continuously scan the mapping region along the scanning axis at a smooth and rapid speed. This observing mode benefits from the speedy observing capability of a large area with the minimum change in the setup of the observing system and improves the observing efficiency. We observed the widest area in ¹³CO and C¹⁸O lines (~ 1.37 deg², white box in Figure 1) to trace all the most extended faint structures. N₂H⁺ and HCO⁺ lines (~ 0.56 deg², red box in Figure 1) and CS and SO lines (~ 0.39 deg², yellow box in Figure 1) were observed toward the dense core areas including their nearby envelopes. Finally, the observations of NH₂D and H¹³CO⁺ lines were focused toward the densest regions in the cloud (~ 0.11 deg², green boxes in Figure 1).

2.2. Data Reduction

The raw data were obtained in the shape of a tile, an OTF scan individually observed, toward line emitting regions for each set of molecular lines (see Figure 1). After a first-order baseline correction using the OTFTOOL, the raw data were re-gridded to a cell size of 22'' and converted into the CLASS format. Noise weighting is applied to obtain a better signal-to-noise ratio (S/N). After the preprocessing, the baselines of the spectra were removed by an iterative second-order polynomial fitting. The spectra were resampled with a channel width of 0.06 km s⁻¹. The velocity range was cropped to have the brightest emission of ¹³CO (~ 9 km s⁻¹) at the line center and a full coverage of 60 km s⁻¹. Then, all the tiles were combined to make one averaged scan map for each transition. The observation was continuously performed until the rms level of each average tile was $\lesssim 0.1$ K [$T_{A,\text{rms}}^*$] at the 0.1 km s⁻¹ channel width for C¹⁸O (1-0) and ¹³CO (1-0), $\lesssim 0.07$ K [$T_{A,\text{rms}}^*$] at the 0.1 km s⁻¹ channel width for SO (3₂-2₁) and ortho-NH₂D (1₁₁-1₀₁), and $\lesssim 0.07$ K [$T_{A,\text{rms}}^*$] at the 0.06 km s⁻¹ channel width for N₂H⁺ (1-0), HCO⁺ (1-0), H¹³CO⁺ (1-0), and CS (2-1). In the final step, spectra for four molecular lines (those of ortho-NH₂D (1₁₁-1₀₁), SO (3₂-2₁), N₂H⁺ (1-0), C¹⁸O (1-0), and ¹³CO (1-0) transition) were smoothed to have

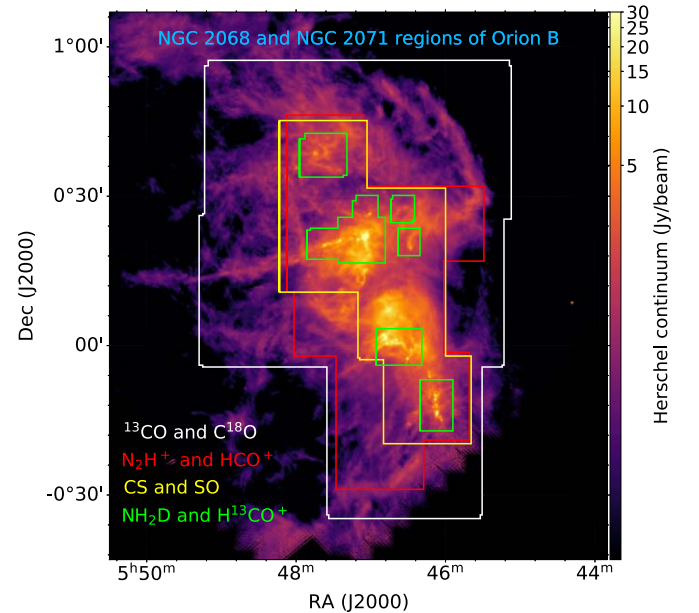


Figure 1. The survey areas of Orion B. The areas observed with various molecular lines are marked in white (¹³CO and C¹⁸O), red (N₂H⁺ and HCO⁺), yellow (CS and SO), and green (NH₂D and H¹³CO⁺) boxes on the Herschel 250 μm continuum image.

their channel width be 0.1 km s⁻¹. The channel widths of the H¹³CO⁺ (1-0), HCO⁺ (1-0), and CS (2-1) molecular lines remained at 0.06 km s⁻¹ (see Table 1).

3. Results

3.1. Filamentary Structures

The overall distribution of molecular emission in Orion B can be best traced with ¹³CO and C¹⁸O lines simultaneously observed. Figure 2 indicates that the ¹³CO emission depicts the large-scale distribution of molecular gas in Orion B (middle left panel), while the C¹⁸O emission traces dense filamentary structures (middle right panel).

Panels (a)–(f) in Figure 2 show various aspects of ¹³CO and C¹⁸O line profiles. We find that the multiple velocity components are common in the Orion B region and the

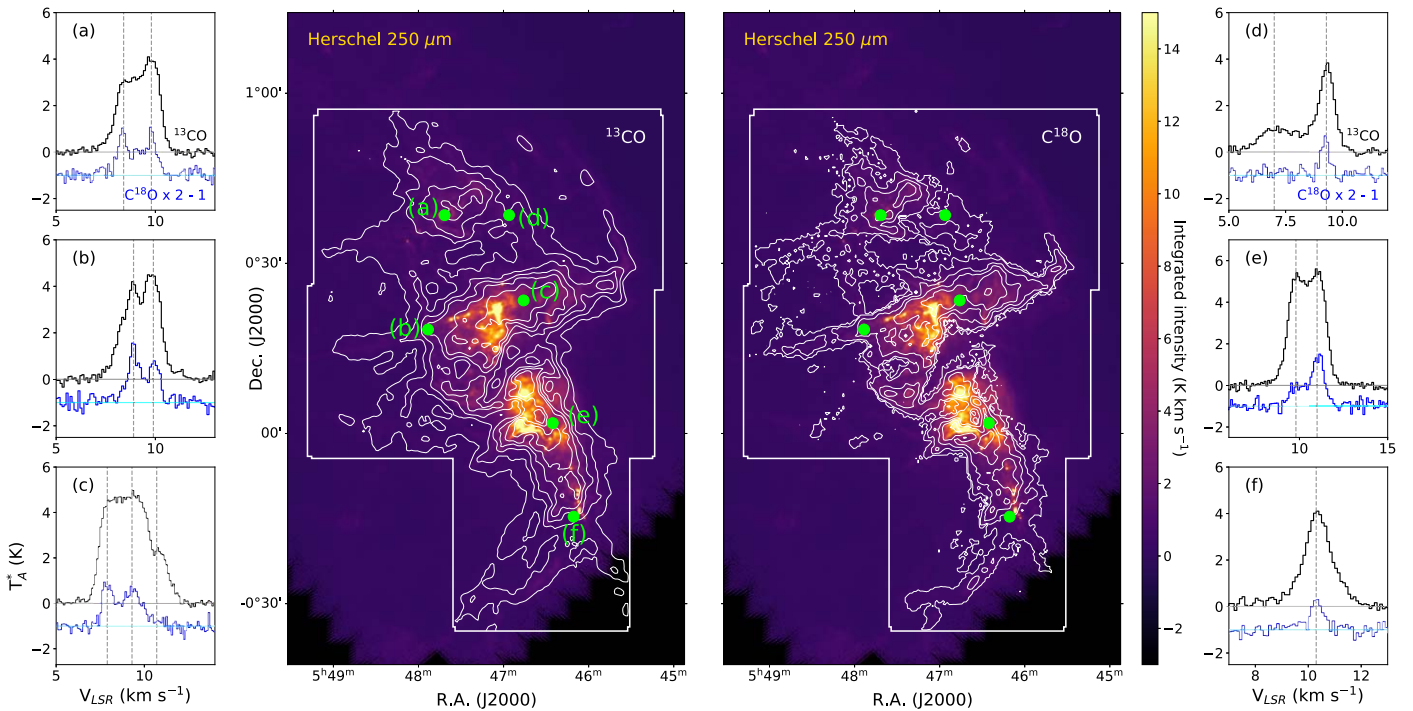


Figure 2. The color scale presents a Herschel 250 μm continuum image of the Orion B region. Contours are from the integrated intensity maps of ^{13}CO (middle left panel) and C^{18}O (middle right panel). The contour levels for the ^{13}CO integrated intensity map are [1, 3, 5, 7, 9, 11] K km s^{-1} and those for the C^{18}O integrated intensity map are [0.25, 0.75, 1, 1.5, 2.2, 3.5, 6] K km s^{-1} . Panels (a)–(f) show representative spectra of ^{13}CO (black line) and C^{18}O (blue line) at the central positions marked with green dots in the middle left panel and the middle right panel. In panel (a)–(f), the C^{18}O spectrum is scaled up by a factor of 2 and shifted by -1 in intensity. The gray and cyan horizontal lines represent baselines of the ^{13}CO and C^{18}O spectra, respectively.

double-peaked profile in C^{18}O spectrum is more clearly separable than ^{13}CO spectrum. The distribution of both molecular transitions in the middle panels and the undetected emission peaks in panels (c) and (d) indicate that the $\text{C}^{18}\text{O}(1-0)$ transition is tracing a more compact region with higher density than the $^{13}\text{CO}(1-0)$ transition and the ^{13}CO emission is extended over a wider region, tracing the bulk motion of less dense molecular gas. Meanwhile, in panels (b) and (e), two peaks in the ^{13}CO emission have comparable intensities. On the other hand, the C^{18}O emission peaks have different intensity levels. This may arise from optical depth effects or from different excitation. Panel (f) shows that both the ^{13}CO and C^{18}O emissions have the same velocity centroid at $\sim 10.3 \text{ km s}^{-1}$ but the ^{13}CO emission has almost a 2 times wider line width. Based on the spectral information, the dips of ^{13}CO spectra in panels (a)–(e) are not self-absorption features, but due to multiple velocity components. For the purpose of this paper, the $\text{C}^{18}\text{O}(1-0)$ line is used to resolve velocity components on the line of sight and identify velocity-coherent filamentary structures in Orion B in Section 3.1.1.

3.1.1. Identification of Velocity-coherent Filaments

In order to identify velocity-coherent structures in the Orion B, which are seen as overlapping the line of sight, we decompose the multiple velocity components of the $\text{C}^{18}\text{O}(1-0)$ spectrum at each pixel by using the automated Gaussian decomposing code FUNStools.Decompose,¹⁴ which is an optimally developed Python class for TRAO-FUNS data. The brief step-by-step description of the procedure is as follows (see the details in Kim et al., in preparation):

1. *Step1:* In the beginning, we do not know how many multiple velocity components exist and where their centroid velocities are located in a single spectrum, and thus initial guesses for those are required. First, the velocity smoothing process in a spectrum is performed to improve its S/N, which would reduce the confusion from noise spikes. Then, spatial smoothing process is made using a two-dimensional Gaussian kernel to make spatial continuity and avoid local fluctuation for the determination of the number of velocity components. From the smoothed spectrum, the peak velocity positions of the expected Gaussian components are determined by applying the find peaks algorithm in the scipy.signal package to find zero-second derivatives of the spectrum. Based on the number of components and their velocity positions, initial multiple Gaussian fits are performed to the smoothed spectra. The final returns at *Step1* are the initial guesses for each decomposed Gaussian component for the next step. In this step, smoothing parameters should be selected depending on the characteristics (e.g., distribution and dynamic range of emissions) of the molecular cloud and the spectral resolution.
2. *Step2:* Using the initial guesses determined from *Step1*, a Gaussian fitting for the spectra is performed using these initial guesses to find the best-fit spectrum and returns the resulting Gaussian fitting parameters for each velocity component of the spectrum.
3. *Step3:* A final Gaussian fitting is performed to enhance the spatial continuity of the decomposed results. The initial guesses for parameters are modified based on the best-fit parameters of the surrounding pixels obtained from *Step2*. Then, a multiple Gaussian fit is performed again with the adjusted initial guesses. Note that both the velocity and spatial smoothing factors in this step are

¹⁴ <https://github.com/radioshiny/funstools>

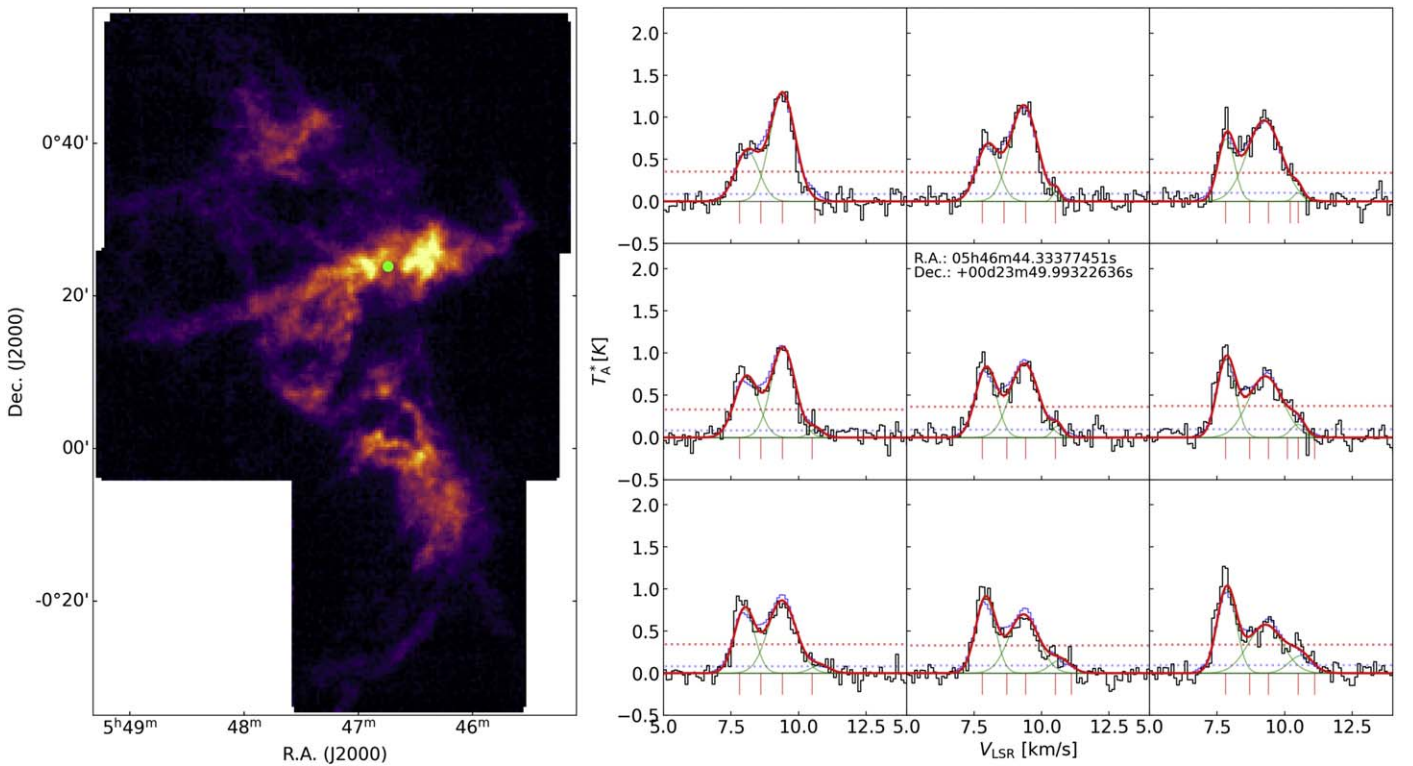


Figure 3. Left panel: integrated intensity map of the C^{18}O (1–0) line of Orion B. The green dot denotes the position of the central pixel of the 3×3 spectra in the right panel. Right panel: representative spectra are shown with results from the step-by-step decomposing procedure described in Section 3.1.1. Black solid line: original spectrum at each pixel. Blue solid line: smoothed profile with the initial smoothing parameters (Step1). Red vertical line: initial guesses of velocity component found in Step1. Green solid line: decomposed Gaussian profiles determined in Step3 with modified initial guesses from Step2. Red thick solid line: the profiles combined by decomposed Gaussian components. Red and blue horizontal dotted lines: 3σ levels of original and smoothed profiles, respectively.

recommended to be smaller than the parameters in Step1 of this tool.

In order to improve the reliability of Step1, the original spectrum was smoothed with 4 channels (0.4 km s^{-1}) in velocity after extracting the spectra above 3σ level in their intensity. The spatial smoothing factor adopted in the step is adopted as a scale of 4 pixels ($88''$), which corresponds to the FWHM of a Gaussian kernel in Step1. In the case of Step3, smoothing in smaller ranges, 2 channels (0.2 km s^{-1}) in velocity and 2 pixels ($44''$) in space, was performed to make a better fit to the original spectrum. The multiple Gaussian functions were used to fit the observed line profile with the initial guesses described in Step1. The optimization of the Gaussian fit to the observed line profile was performed using the Python routine `curve_fit` in the `scipy.optimize` package. The routine adopts the nonlinear least-squares fit based on the TRF (Trust Region Reflective) algorithm. Figure 3 presents an example of the Gaussian decomposing around the position marked with a green dot in the left panel. The green Gaussian profiles are the velocity components decomposed from `FUNStools.Decompose` and the red spectra are the profiles combined by the decomposed components. Using the automated Gaussian decomposing code, 10,756 Gaussian components were identified with their peak intensities of an $S/N > 3$.

Figure 4 presents the averaged ^{13}CO and C^{18}O spectra over the entire observing region. After a careful decomposition of multiple Gaussians with line observations with a $22''$ grid size obtained by our TRAO-FUNS survey, we find that there are multiple velocity components with a wide range of velocity ($\sim 7.8\text{--}11.5 \text{ km s}^{-1}$) and present a histogram of the decomposed velocity components in Figure 5.

With the decomposed velocity components, identification processes of the filaments using the friends-of-friends (FoF) algorithm were performed to eventually find velocity-coherent filamentary structures. The detailed processes of identifying the filaments are summarized as follows: first, all velocity components decomposed from the Gaussian fits are compared with a reference velocity component at the pixel with the brightest emission. If the velocity difference (V_{diff}) between the component and the reference one is less than the spectral resolution $\sim 0.1 \text{ km s}^{-1}$ and the positional distance between two comparing pixels is $\leq \sqrt{2}$ pixel size (maximum distance between the reference pixel and one of neighboring 8 pixels) for their continuous positional connection, they become a part of a velocity-coherent structure. Here, we set the number of pixels for a velocity-coherent structure to be at least larger than 25, which corresponds to the number of pixels in a $5 \times \theta_B$ area (here, θ_B is the HPBW of C^{18}O (1–0) $\sim 49''$). This process was iteratively done until no component was left to be compared. The parameters can be empirically determined, and probably would be dependent on the properties of the molecular cloud.

Now we explain how we identify the velocity-coherent filaments in the Orion B region by using the FoF algorithm (Figure 6). In the starting run of the FoF, we set the difference between adjacent velocity centroids of the Gaussian components to be less than 0.1 km s^{-1} . Then, all the velocity components, except one small part of the cloud, are identified as one big velocity-coherent structure (see panel (a) in Figure 6). The shaded parts in the gray region are meant to indicate that those regions have two or more velocity components at the single pixel (i.e., at the same line-of-sight direction), but are chosen as a part of one velocity-coherent

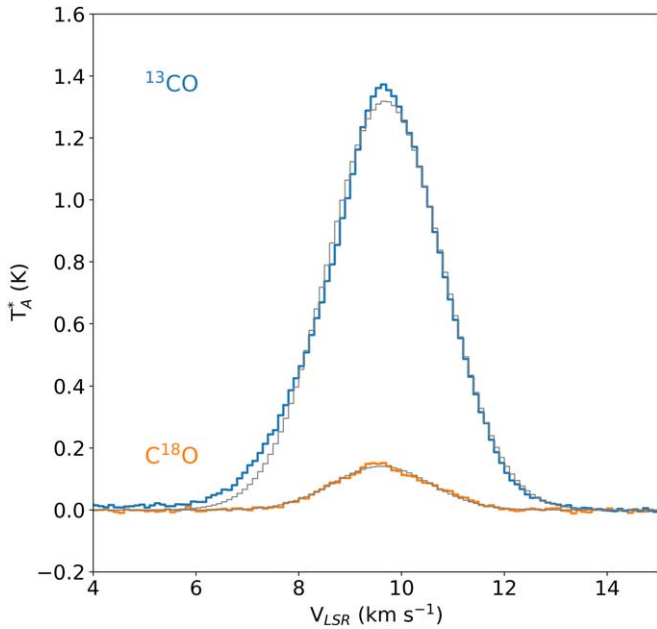


Figure 4. The averaged $J = 1-0$ line profiles of ^{13}CO (blue) and C^{18}O (orange) throughout the whole line emitting region. Gray lines indicate the best-fit Gaussian profiles.

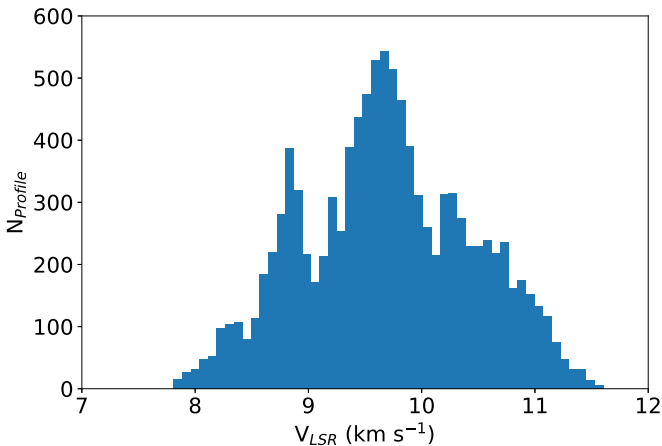


Figure 5. The velocity distribution of C^{18}O (1–0) Gaussian-fit components decomposed by the Gaussian decomposition process (see Section 3.1.1).

structure. As the inset of Figure 6(a) shows, the spectrum shows obvious double-peaked components. We simply assume that the C^{18}O (1–0) line is mostly optically thin and thus any asymmetric C^{18}O (1–0) line emission would be due to a sum of multiple Gaussian components. Hence, every single filament identified here corresponds to a cloud component that has a well-defined velocity at each pixel position. This forces us to run the FoF algorithm again with a different, in this case, smaller V_{diff} parameter to enable us to distinguish these multiple velocity components. Therefore, for the gray filamentary structure (with multiple velocity components) obtained in the previous step (see Figure 6(a)), we perform FoF again with V_{diff} of 0.08 km s^{-1} , being able to identify more independent structures having single velocity component (colored regions in Figure 6(b)). However, even in the second run of the FoF, we find several regions where multiple velocity components still exist even after identifying a velocity-coherent structure. For example, in the middle region inset of panel (b) of Figure 6, the pink-colored region is identified as a velocity-coherent

structure, but the gray-colored structure still contains two velocity components. Because of this problem, a third trial of FoF for these structures is performed with a parameter of $V_{\text{diff}} = 0.06 \text{ km s}^{-1}$ in panel (b). In this way, we perform the FoF until every identified filamentary structure contains a single velocity component only. Panel (d) shows the results of our last trial of FoF performed with a V_{diff} of 0.045 km s^{-1} after multiple tests with V_{diff} of 0.03, 0.035, 0.04, 0.045, and 0.05 km s^{-1} , indicating that the cloud regions previously marked by gray velocity profiles (insets in panel (b) and (c) in Figure 6) are finally well decomposed. Lastly, we check whether any Gaussian components with significant emission ($\sim 3\sigma$) are missed during the FoF running by visual inspection and recover those in the final filamentary structure.

Through all these steps, a total of 30 velocity-coherent structures were finally identified as filaments in the Orion B region. Figure 7 presents morphologies, velocity structures, spine structures of the filaments, and the distribution of YSOs classified by Furlan et al. (2016) in the filaments. These will be the main constituents for the discussion of the physical properties of the filaments in the following sections.

In order to display how all the filamentary structures are related to the velocity structure in detail, we provide the velocity channel maps of the C^{18}O (1–0) emission with intervals of 0.4 km s^{-1} from 7.3 – 12.3 km s^{-1} in Figure 8. The northern part of the molecular cloud is dominated by the lower velocity component and the middle and southern parts have bright emission at the higher velocity ranges. As in Figure 8, Figure 5 and the upper-right panel of Figure 7 illustrate that the filaments in Orion B have velocity ranges from ~ 7.8 to $\sim 11.5 \text{ km s}^{-1}$ with gradually increasing LSR velocities from north to south. For velocity centroids of the overlapping regions in Figure 7(b), we present the detailed information for each filament in Appendix A and provide a three-dimensional visualization in Figure 9. The ranges of the velocity centroids and the averaged line dispersions for each filament are tabulated in Table 2.

The position–velocity (PV) plots shown in Figure 10 along the R.A. and decl. directions indicate that the C^{18}O (1–0) velocity centroid for individual filaments smoothly changes in velocity and position with interesting oscillatory patterns in a single structure. The PV diagram drawn using the ^{12}CO (2–1) molecular line survey (Nishimura et al. 2015) has also revealed such oscillating features in V_{LSR} (see also L1630N in the upper panel of Figure 3 in Großschedl et al. 2021). While the ^{12}CO (2–1) LSR velocity shows the averaged large-scale bulk motion of the cloud, our decomposed C^{18}O (1–0) LSR velocity is able to reveal individual motions of substructures along the line of sight (Figures 9 and 10). We provide a link to the interactive viewing mode of velocity centroids in three-dimensional PPV space in Figure 9. Further analysis and discussion of these velocity oscillations are presented in Section 4 (especially in Section 4.5).

3.1.2. Lengths and Widths of the Filaments

Here we attempt to quantify the properties of the filaments. For this purpose, we define the main structures of the filaments using the Python package filfinder (Koch & Rosolowsky 2015), which extracts the main structure from the two-dimensional image via a medial axis transform (Blum 1967). First, we produce the integrated intensity image for each filament from their resultant parameters (e.g., the amplitude, the velocity centroid, and the velocity dispersion) derived from the multiple Gaussian fits to the spectra for each filament (see panels (a)–(c) in Figure 11). The

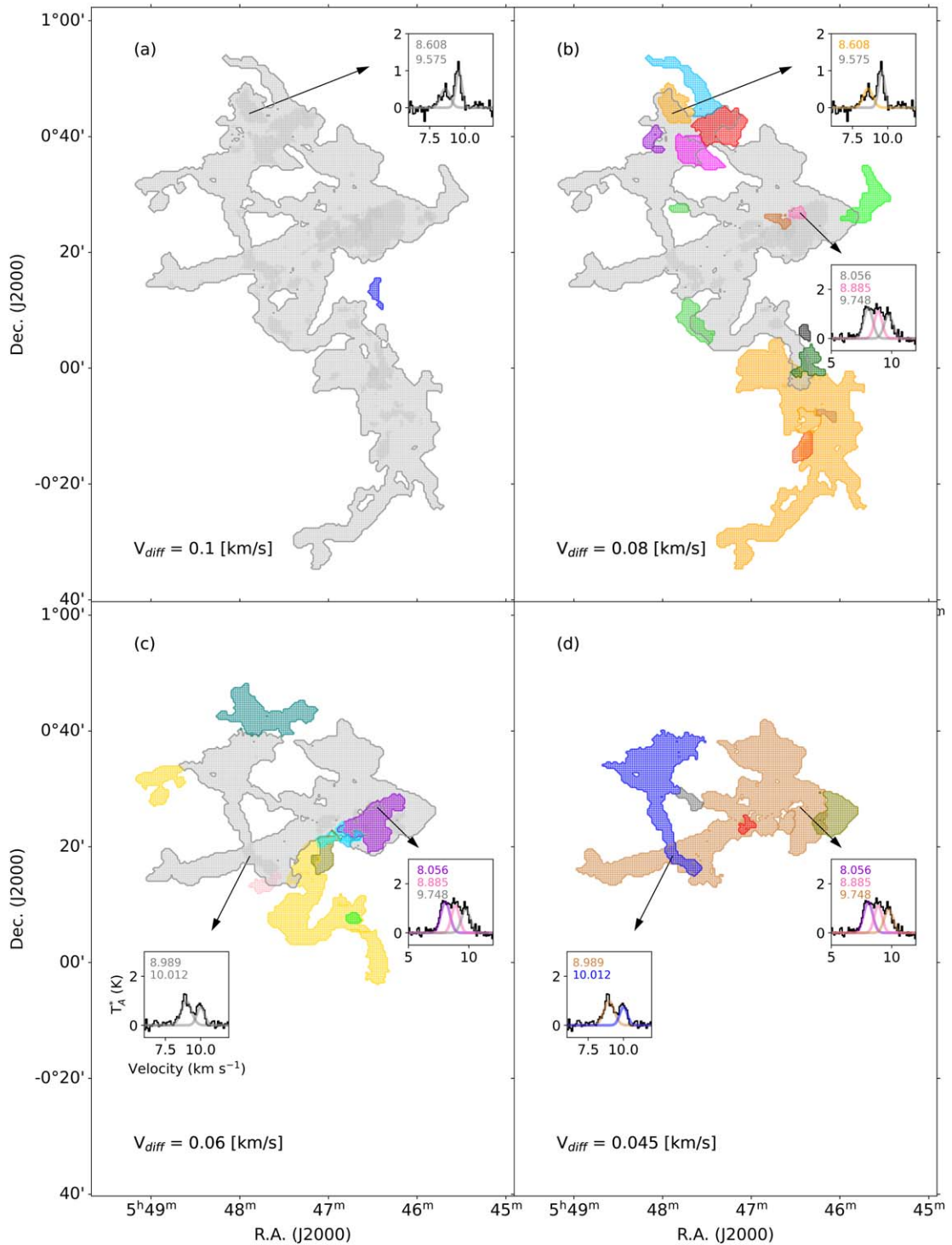


Figure 6. Procedures identifying velocity-coherent filamentary structures with the FoF algorithm in the Orion B region. The colored regions denote the filamentary structures identified from FoF with the criteria for spatial separation ($\sqrt{2}$ pixel size) and velocity difference V_{diff} (from 0.1–0.045 km s^{-1}) written on the bottom of the panels. The gray region in each panel is a continuously connected structure within the velocity criteria and the shades (darker regions) in the gray region indicate that there are multiple velocity components in the line of sight in the velocity-coherent structure. The insets in the panels denote C^{18}O (1–0) spectra and their decomposed Gaussian components at a pixel point. The numbers in the insets indicate the velocity centroids of the Gaussian components at the start point of the arrow. The colors of the velocity centroid numbers and Gaussian-fit profiles correspond to the colors of the filamentary structures.

filfinder algorithm not only provides the information on the spine of the filaments (see the lower-left panel in Figure 7) but also the ones for the branches stretched out from the spine. We use the length of the spine for each filament as the filament’s length l , and list them in Table 2. The largest length of the filament is ~ 6.5 pc and the median length for the entire sample of the filaments is

0.8 pc. This median length of the filaments is comparable to the case of B213-L1495 in Taurus (1.0 ± 0.2 pc) but longer than the cases of integral shape filament in Orion (0.2 ± 0.1 pc) or NGC 1333 in Perseus (0.4 ± 0.2 pc) (Hacar et al. 2018).

We use the averaged radial profile to estimate the filament’s width. Along each spine, we chose the sampling points on the

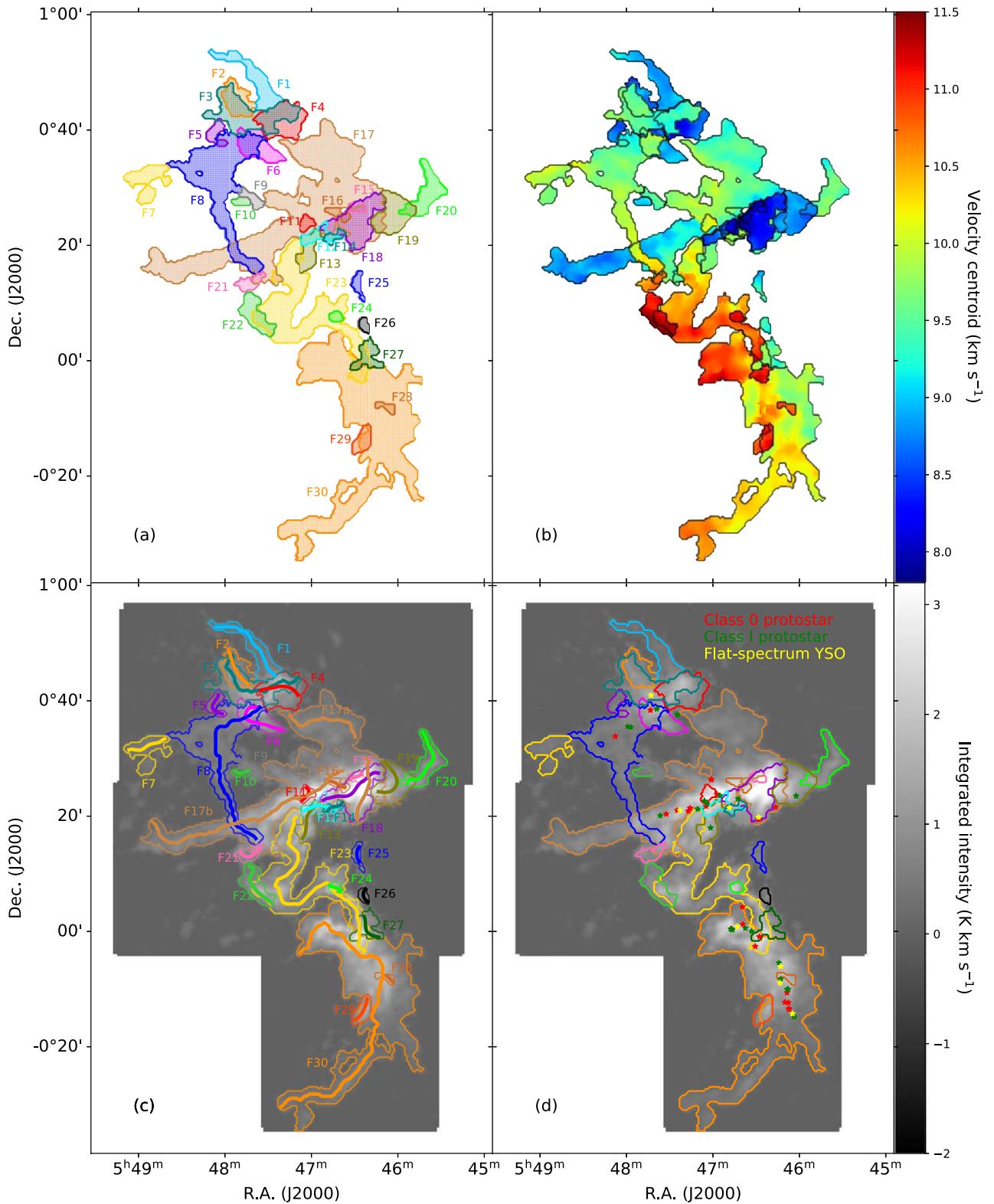


Figure 7. Velocity-coherent filaments in Orion B identified with the FoF algorithm. (a) Morphologies of the filaments. The filament names are labeled with the same colors as each filament. (b) The distribution of velocity centroids ranges from 7.8–11.5 km s⁻¹ within identified filaments. (c) The spines of each filament are drawn with thick lines. (d) The distribution of YSOs identified and classified in Furlan et al. (2016). Red asterisk symbol: Class 0 protostars. Green asterisk symbol: Class I protostars. Yellow asterisk symbol: flat-spectrum YSOs. The colored contours delineate the filaments identified in this study. Gray tones in the two lower panels indicate the distribution of the integrated intensity of C¹⁸O (1–0) line.

spine with an interval of 25'' and made a cut across the spine to build the transversal profile. In Figure 11(d), the cyan curve indicates the smoothed line of the spine of Filament 20, and the black lines indicate the transversal lines used to produce the

radial profiles in Figure 12. The gray lines in Figure 12 denote individual radial profiles obtained across the cuts in Figure 11(d) and the black line denotes an average one of these radial profiles. Once the average profile is produced using

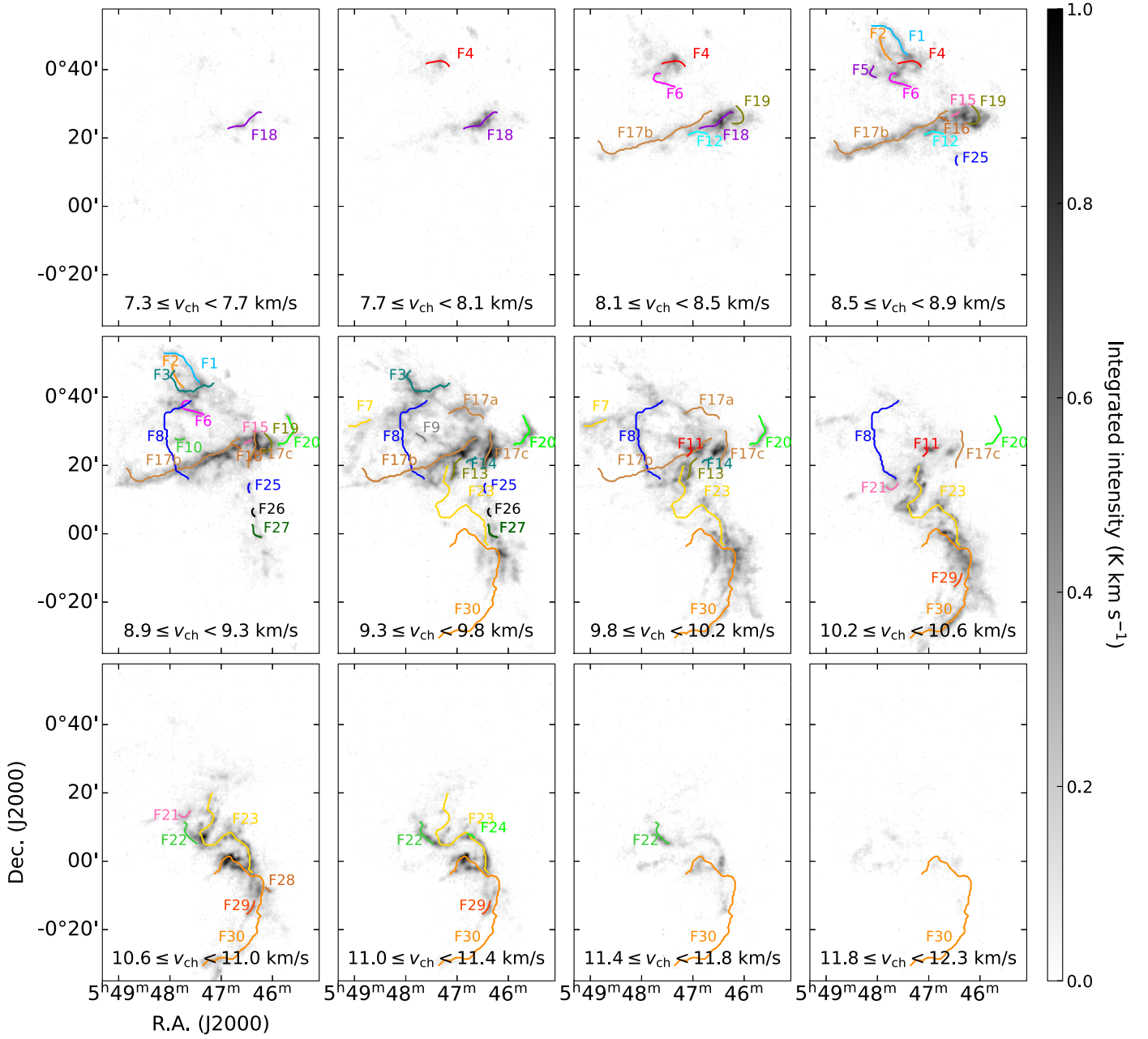


Figure 8. The velocity channel maps of C^{18}O (1–0) emission in relation to the identified filamentary structures. The velocity ranges of integration are indicated in the bottom of each panel. The filament spines covering the velocity channel range of each panel are overlaid with the same colors as the ones for the filaments in Figure 7.

all the transversal profiles, the 1D-Gaussian model fits the averaged profile to determine the FWHM as a width (W) of the filament. The median value of the filament widths is estimated to be 0.1 pc with a range of 0.05–0.26 pc. It should be noted that the TRAO beam $\sim 50''$ is comparable to the physical scale of the median width of the filaments (~ 0.1 pc) at the distance of Orion B, and hence this measured width is likely affected by our observing beam size (see also Panopoulou et al. 2022).

The aspect ratio, which is defined as the ratio of the length l and the width W of the filament ($\text{AR} = l/W$), is used to define how the filamentary structure is elongated (André et al. 2014). In our study, we define the C^{18}O structures as filaments if their aspect ratios (ARs) are larger than 3. Note that F17 has a quite large and complicated structure. Therefore, we divide it into three parts (F17a, F17b, and F17c) in this case for calculating their physical parameters. The lengths, widths, and ARs for the

entire velocity-coherent structures are given in Table 2. The uncertainty on length comes mostly from the uncertainty on distance ($\sim 5\%$; Zucker et al. 2019).

3.1.3. Column Densities, Masses, and Line Masses of Filaments

The C^{18}O column densities of the filaments were estimated using the following equation obtained under the assumption of local thermodynamic equilibrium (e.g., Garden et al. 1991 and Pattle et al. 2015):

$$N(\text{C}^{18}\text{O}) = \frac{3k_B}{8\pi^3 B \mu_D^2} \frac{e^{hB J(J+1)/k_B T_{\text{ex}}}}{J+1} \times \frac{T_{\text{ex}} + \frac{hB}{3k_B}}{1 - e^{-h\nu/k_B T_{\text{ex}}}} \int \tau dv, \quad (1)$$

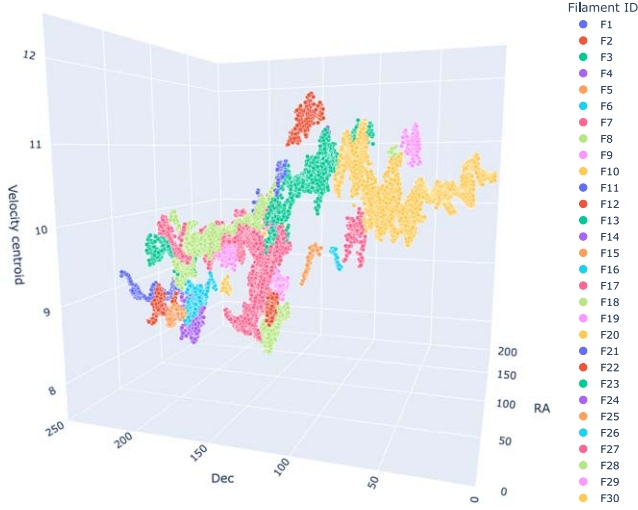


Figure 9. The distribution of the $C^{18}O$ (1–0) velocity centroids of 30 identified filaments in three-dimensional PPV space in the units of pixels (along the R.A. and decl. directions) and kilometers per second (for velocity centroid). The colors of the dots are not identical to the colors of the filaments in Figure 7. Please refer to the colors and names in the legend in the viewing mode. The interactive viewing mode of this figure is available at <https://hyunjuyoo.github.io/Orion-Filaments/>

(An interactive version of this figure is available.)

where k_B is the Boltzmann constant, $B = 5.79384 \times 10^{10} \text{ s}^{-1}$ is the rotational constant, $\mu_D \sim 0.112 \text{ D}$ is the permanent dipole moment of the molecule, and J is the lower rotational level of the $C^{18}O$ (1–0) transition. The excitation temperature T_{ex} is assumed to be the same as the dust temperature T_{dust} obtained from the Herschel dust continuum emission in the Orion B region (Schneider et al. 2013; Könyves et al. 2020). In the UV-dominated regions, the gas kinematic temperature and the dust temperature are difficult to derive. However, the $C^{18}O$ excitation temperature becomes closer to T_{dust} in the dense cloud regions where T_{dust} is lower than 20 K (Roueff et al. 2020). In our observed region, most T_{dust} values are lower than 20 K (see Figure 13), and thus, we use T_{dust} as T_{ex} in the column density calculation (see the averaged dust temperature used for calculation for each filament in Table 2).

The integration of the optical depth, which is the rightmost term of the Equation (1), can be expressed as below:

$$\int \tau dv = \frac{1}{J(T_{\text{ex}}) - J(T_{\text{bg}})} \int \frac{\tau(v)}{1 - e^{-\tau(v)}} T_{\text{mb}}(v) dv$$

$$\approx \frac{1}{J(T_{\text{ex}}) - J(T_{\text{bg}})} \frac{\tau(v_0)}{1 - e^{-\tau(v_0)}} \int T_{\text{mb}}(v) dv, \quad (2)$$

where $J(T) = T_0/(e^{T_0/T} - 1)$ is the source function ($T_0 = h\nu/k_B$), $T_{\text{bg}} = 2.73 \text{ K}$ is the cosmic microwave background temperature, $T_{\text{mb}}(v)$ is the observed main beam temperature at velocity v , and v_0 is the centroid velocity. Here, the ranges of integrated velocity are determined by each decomposed $C^{18}O$ spectrum for individual filaments.

The optical depth at the central velocity $\tau(v_0)$ in Equation (2) is derived by the following relation, assuming that the ^{13}CO and $C^{18}O$ lines trace similar densities and are excited with the same

temperature:

$$\frac{T_{\text{max}}^{C^{18}O}}{T_{\text{max}}^{^{13}\text{CO}}} \approx \frac{1 - e^{-\tau^{C^{18}O}}}{1 - e^{-\tau^{^{13}\text{CO}}}}, \quad (3)$$

where $T_{\text{max}}^{C^{18}O}$ and $T_{\text{max}}^{^{13}\text{CO}}$ are the intensities of the $C^{18}O$ (1–0) and ^{13}CO (1–0) transitions at the centroid velocity of the $C^{18}O$ line profiles, respectively. Here, we use an isotopic ratio $[^{13}\text{CO}/C^{18}O] = 10$ to calculate the optical depth, although the value $[^{13}\text{CO}/C^{18}O] = 5.5$ (Frerking et al. 1982) is widely used. This is because the abundance ratio of $C^{18}O$ in the Orion molecular cloud is believed to be different from the terrestrial one (Nishimura et al. 2015). For example, the abundance ratios in the NGC 2023 and NGC 2024 regions of Orion B and the Orion A giant molecular cloud are reported to range from 8–50 with a mean value of 12.5 (Roueff et al. 2020), and from 5.7–33 with mean values of a factor of 2–3 larger than the terrestrial value, respectively, depending on the effect of the selective photodissociation of $C^{18}O$ by the far-UV radiation (Shimajiri et al. 2014). In this way, the $C^{18}O$ column densities for the filaments were estimated and found to be in the wide range between 10^{14} and 10^{16} cm^{-2} .

The masses of the velocity-coherent filaments are estimated from the Herschel column density map (André et al. 2010; Könyves et al. 2020), which is convolved to the resolution of the TRAO beam ($\theta_B = 48.''7$ for $C^{18}O$ (1–0)). Since decomposed velocity components cannot be distinguished in the Herschel continuum map, we modify the Herschel masses based on the fraction of the intensity of $C^{18}O$ emission associated with the specific structure used to calculate the filament’s mass.

The H_2 column densities of the velocity-coherent filaments range from 2.8×10^2 to $1.4 \times 10^{22} \text{ cm}^{-2}$ with a median of $6.1 \times 10^{21} \text{ cm}^{-2}$. The minimum and maximum masses of these filaments are 2.5 and $700 M_{\odot}$ with a median of $35 M_{\odot}$. Line masses (M_{line}), which are masses within the velocity-coherent structures divided by the lengths, are calculated to range between 14 and $175 M_{\odot} \text{ pc}^{-1}$ (Table 2). The uncertainties of M and M_{line} are estimated from the observational rms error and uncertainty on the length. The typical uncertainties of M and M_{line} are $\sim 13\%$ and $\sim 12\%$, respectively.

3.1.4. Velocity Dispersion

We introduce four velocity dispersions in describing the kinematical information of the clouds and cores in Orion B such as the observed, thermal, nonthermal, and total velocity dispersions (σ_{obs} , σ_{th} , σ_{nth} , and σ_{tot} , respectively). The observed velocity dispersion (σ_{obs}) can be given with the FWHM (Δv_{obs}) of the line profile observed at the position of the peak emission, in the relation of $\Delta v_{\text{obs}} = \sqrt{8 \ln 2} \sigma_{\text{obs}}$. The thermal velocity dispersion is defined as $\sigma_{\text{th}} = \sqrt{k_B T_{\text{dust}}/m_{\text{obs}}}$ for the observing molecule with a mass of m_{obs} and can be related to the nonthermal contribution (σ_{nth}) in the turbulent clouds as follows (Myers et al. 1991):

$$\sigma_{\text{nth}} = \sqrt{\sigma_{\text{obs}}^2 - \sigma_{\text{th}}^2}$$

$$= \sqrt{\frac{\Delta v_{\text{obs}}^2}{8 \ln 2} - \frac{k_B T_{\text{dust}}}{m_{\text{obs}}}}. \quad (4)$$

Table 2
Physical Properties of the Filaments in Orion B

Fil. ID (1)	l (2)	W (3)	AR (4)	$\langle V_{\text{LSR}} \rangle_{\text{min}}^{\text{max}}$ (5)	$\langle T_{\text{dust}} \rangle$ (6)	σ_{tot} (7)	M (8)	M_{line} (9)	$M_{\text{line}}^{\text{tot,crit}}$ (10)	$M_{\text{line}}^{\text{th,crit}}$ (11)	$N_{\text{H}_2}^{\text{Herschel}}$ (12)	$N_{\text{H}_2}^{\text{C}^{18}\text{O}}$ (13)	Core (14)	YSO (15)
F1	1.8	0.09	19.3	$8.9_{8.8}^{9.3}$	14.7	0.35 ± 0.03	45 ± 6	26 ± 4	57 ± 10	25 ± 11	4.2	9.6	0	0
F2	0.8	0.18	4.8	$8.7_{8.5}^{9.0}$	14.3	0.38 ± 0.04	27 ± 5	40 ± 6	67 ± 14	23 ± 14	4.0	9.1	0	0
F3	2.0	0.15	13.5	$9.5_{9.0}^{9.8}$	13.9	0.38 ± 0.03	106 ± 13	66 ± 7	67 ± 11	23 ± 10	6.2	14.1	3	1
F4	0.9	0.26	3.4	$8.5_{8.1}^{8.9}$	13.9	0.39 ± 0.03	79 ± 9	95 ± 11	71 ± 11	23 ± 10	6.1	13.8	1	0
F5	0.6	0.07	7.8	$8.7_{8.5}^{8.9}$	14.4	0.31 ± 0.03	10 ± 2	15 ± 3	45 ± 9	23 ± 8	2.8	6.3	0	0
F6	1.1	0.16	6.7	$8.8_{8.4}^{9.2}$	13.3	0.43 ± 0.03	86 ± 7	64 ± 7	86 ± 12	23 ± 12	7.1	16.2	4	2
F7	0.8	0.11	7.3	$9.8_{9.6}^{10.1}$	15.1	0.35 ± 0.03	19 ± 5	40 ± 6	57 ± 10	25 ± 11	3.6	8.2	0	0
F8	3.5	0.12	28.5	$9.7_{9.0}^{10.6}$	14.3	0.37 ± 0.03	185 ± 25	56 ± 7	64 ± 10	23 ± 10	4.7	10.8	2	5
F9	0.4	0.07	5.8	$9.5_{9.3}^{9.6}$	14.3	0.47 ± 0.05	10 ± 2	27 ± 4	103 ± 22	23 ± 20	4.9	11.2	1	0
F10	0.3	0.07	4.9	$9.1_{9.0}^{9.2}$	14.2	0.33 ± 0.03	6 ± 1	14 ± 2	51 ± 9	23 ± 8	3.4	7.7	0	0
F11	0.3	0.07	4.6	$10.1_{9.9}^{10.3}$	14.3	0.46 ± 0.03	16 ± 1	49 ± 5	98 ± 13	23 ± 12	8.6	19.6	0	2
F12	0.7	0.07	9.7	$8.6_{8.4}^{8.9}$	16.2	0.47 ± 0.04	36 ± 3	41 ± 5	103 ± 17	27 ± 18	7.5	17.0	0	2
F13	0.8	0.10	8.4	$9.6_{9.4}^{9.9}$	20.1	0.54 ± 0.03	62 ± 5	97 ± 7	136 ± 15	31 ± 15	12.9	29.4	1	2
F14	0.4	0.07	5.8	$9.8_{9.6}^{9.9}$	15.7	0.50 ± 0.04	6 ± 1	28 ± 3	116 ± 19	25 ± 19	6.6	15.1	0	1
F15	0.3	0.06	4.3	$8.9_{8.8}^{9.1}$	12.8	0.39 ± 0.02	9 ± 1	41 ± 4	71 ± 7	21 ± 8	7.6	17.3	0	0
F16	0.3	0.05	6.6	$8.8_{8.7}^{8.9}$	13.6	0.48 ± 0.03	11 ± 1	44 ± 4	107 ± 13	23 ± 14	8.2	18.6	0	0
F17a	1.4	0.21	6.8	$9.5_{9.1}^{9.9}$	14.8	0.34 ± 0.07	84 ± 13	77 ± 10	54 ± 22	25 ± 24	4.8	11.0	0	0
F17b	4.6	0.14	32.6	$9.3_{8.6}^{10.1}$	14.6	0.48 ± 0.06	565 ± 42	134 ± 11	107 ± 27	25 ± 28	10.2	23.3	10	10
F17c	1.4	0.15	9.2	$9.4_{8.9}^{10.1}$	13.9	0.41 ± 0.05	132 ± 10	175 ± 9	78 ± 19	23 ± 20	14.5	33.0	2	3
F18	1.4	0.15	8.9	$8.2_{7.8}^{8.6}$	13.9	0.42 ± 0.03	90 ± 11	112 ± 9	82 ± 12	23 ± 10	8.9	20.2	1	3
F19	1.0	0.17	6.3	$8.8_{8.5}^{9.0}$	14.6	0.45 ± 0.02	66 ± 8	128 ± 8	94 ± 8	25 ± 11	11.2	25.5	0	1
F20	1.4	0.10	13.7	$9.6_{9.1}^{9.8}$	14.7	0.36 ± 0.03	49 ± 6	43 ± 5	60 ± 10	25 ± 9	5.7	13.0	0	0
F21	0.5	0.08	6.9	$10.6_{10.3}^{10.8}$	14.9	0.36 ± 0.04	13 ± 2	21 ± 3	60 ± 13	25 ± 13	3.8	8.7	0	0
F22	1.0	0.12	8.1	$11.3_{11.0}^{11.6}$	14.6	0.37 ± 0.03	43 ± 4	46 ± 5	64 ± 10	25 ± 11	5.9	13.4	2	0
F23	4.7	0.13	37.0	$10.6_{9.7}^{11.3}$	18.2	0.48 ± 0.03	352 ± 34	104 ± 8	107 ± 13	29 ± 14	9.8	22.3	8	2
F24	0.3	0.07	3.7	$11.1_{11.1}^{11.2}$	22.3	0.34 ± 0.02	3 ± 1	16 ± 2	54 ± 6	36 ± 8	3.7	8.4	0	0
F25	0.3	0.06	5.3	$9.2_{8.9}^{9.5}$	16.5	0.43 ± 0.04	8 ± 1	27 ± 4	86 ± 16	27 ± 18	4.5	10.2	0	0
F26	0.3	0.07	4.8	$9.3_{9.1}^{9.5}$	21.1	0.42 ± 0.03	6 ± 1	22 ± 3	82 ± 12	34 ± 13	5.5	12.5	0	0
F27	0.6	0.13	4.9	$9.7_{9.2}^{10.3}$	18.8	0.51 ± 0.04	33 ± 4	70 ± 7	121 ± 19	31 ± 19	8.0	18.3	0	1
F28	0.2	0.06	3.1	$10.8_{10.9}^{10.9}$	14.3	0.33 ± 0.03	3 ± 1	21 ± 4	51 ± 9	23 ± 10	3.1	7.1	0	0
F29	0.5	0.10	53.8	$11.0_{10.7}^{11.3}$	14.1	0.50 ± 0.04	19 ± 3	49 ± 5	116 ± 19	23 ± 18	6.8	15.6	0	0
F30	6.5	0.24	26.7	$10.3_{9.5}^{11.3}$	15.5	0.42 ± 0.03	700 ± 67	130 ± 12	82 ± 12	25 ± 11	7.6	17.2	8	23

Notes. Column 1: filament ID. Column 2 and Column 3: filament length and width in units of parsecs. Column 4: aspect ratio (AR) is defined as the ratio between the length and the width of the filament. Column 5: the average LSR velocity of the filament with its maximum and minimum values in units of kilometers per second. Column 6: averaged dust temperature of the filament in units of kelvins. Column 7: the average total velocity dispersion (estimated with Equation (5)) of the filament in units of kilometers per second. Column 8: mass of the filament derived from the C^{18}O (1–0) emission in units of solar mass. Column 9: line mass of the filament (calculated by l/W) in units of solar mass per parsec. Column 10: the total critical line mass of the filament in units of solar mass per parsec, which corresponds to the virial mass of filament per unit length (Fiege & Pudritz 2000). Column 11: the thermal critical line mass of the filament in units of solar mass per parsec. Column 12 and Column 13: the average H_2 and C^{18}O column densities in units of 10^{21} cm^{-2} and 10^{14} cm^{-2} , respectively. Column 14: the number of N_2H^+ dense cores whose positions and LSR velocities coincide with those of the filaments. Column 15: the number of YSOs whose positions coincide with the filaments (Furlan et al. 2016). (This table is available in machine-readable form.)

In the case of the C^{18}O (1–0) line, $m_{\text{obs}} = \mu_{\text{C}^{18}\text{O}} m_{\text{H}}$ is used, where $\mu_{\text{C}^{18}\text{O}} = 30$ is the molecular weight of C^{18}O and $m_{\text{H}} = 1.67 \times 10^{-24} \text{ g}$ is the hydrogen mass.

The total velocity dispersion σ_{tot} of the mean molecules including both thermal and nonthermal effects is expressed as below:

$$\sigma_{\text{tot}} = \sqrt{\sigma_{\text{nth}}^2 + \frac{k_{\text{B}} T_{\text{dust}}}{m_{\text{H}} \mu_{\text{mean}}}}, \quad (5)$$

where μ_{mean} is the mean molecular weight per free particle ($=2.37$) assuming the mean mass of gas with the cosmic composition of 71% of hydrogen, 27% of helium, and 2% of metal (Kauffmann et al. 2008). The average total velocity dispersion ($\langle \sigma_{\text{tot}} \rangle$) of the filaments is in the range of

0.31–0.54 km s^{-1} . The uncertainty on σ_{tot} is estimated from the uncertainty on the observed velocity dispersion (Table 2).

3.1.5. Critical Line Mass

Assuming that the filamentary structure is a self-gravitating isothermal cylinder with an infinite length, the thermal critical line mass of the filament in an equilibrium state under thermal and gravitational pressure, and the nonthermal critical line mass supported by turbulence can be estimated as below:

$$M_{\text{line}}^{\text{th,crit}} = 2c_s^2/G, \quad (6)$$

$$M_{\text{line}}^{\text{nth,crit}} = 2\sigma_{\text{nth,C}^{18}\text{O}}^2/G, \quad (7)$$

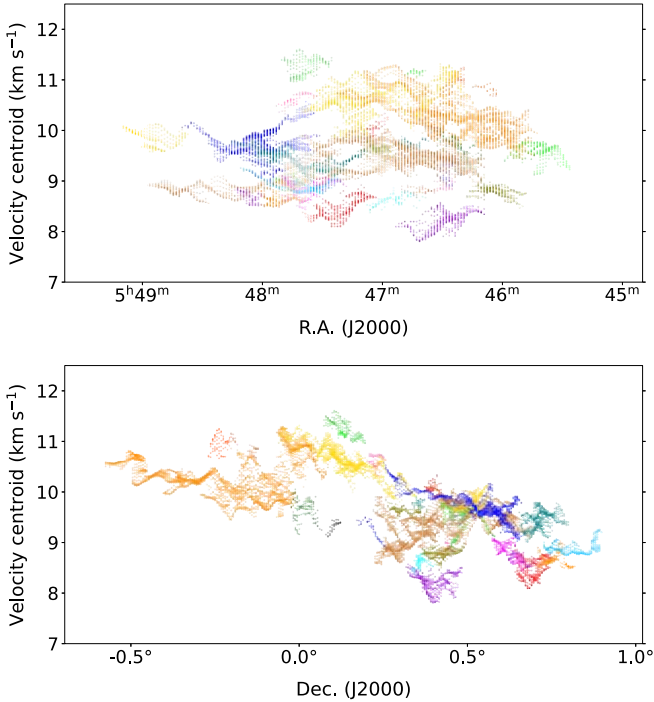


Figure 10. The oscillatory features of the C^{18}O (1–0) velocity centroids of the filaments along the R.A. (upper panel) and decl. (lower panel) directions. The colors of the dots are identical to the colors of the filaments in the upper-left panel of Figure 7.

where c_s is the isothermal speed of sound using the typical dust temperature inside the filament, G is the gravitational constant, and σ_{nth} is the average nonthermal velocity dispersion of filaments traced by C^{18}O (1–0) emission using Equation (4). $M_{\text{line}}^{\text{th,crit}}$ and $M_{\text{line}}^{\text{nth,crit}}$ are found in the ranges of $21\text{--}36 M_{\odot} \text{pc}^{-1}$ with a median value of $24 M_{\odot} \text{pc}^{-1}$ and $17\text{--}102 M_{\odot} \text{pc}^{-1}$ with a median value of $55 M_{\odot} \text{pc}^{-1}$, respectively.

The stability of the filament can be examined by both thermal and nonthermal contributions in comparison with the virial mass of the filament below where the average total velocity dispersion plays an important role (Bertoldi & McKee 1992; Ohashi et al. 2016):

$$M_{\text{vir}}^{\text{fil}} = \frac{2l}{G} \sigma_{\text{tot,C}^{18}\text{O}}^2, \quad (8)$$

where l is the filament length, and $\sigma_{\text{tot,C}^{18}\text{O}}$ is the average total velocity dispersion from the C^{18}O (1–0) emission calculated using Equation (5) with C^{18}O molecular weight ($\mu_{\text{obs}} = 30$). The filament virial mass per unit length ($=M_{\text{vir}}^{\text{fil}}/l$) is referred to as $M_{\text{line,vir}} = 2\sigma_{\text{tot,C}^{18}\text{O}}^2/G$ (Fiege & Pudritz 2000; Arzoumanian et al. 2013), which is $M_{\text{line}}^{\text{tot,crit}}$ in here. $M_{\text{line}}^{\text{tot,crit}}$ is found in the range of $45\text{--}136 M_{\odot} \text{pc}^{-1}$ with a median value of $80 M_{\odot} \text{pc}^{-1}$. The proportions of critical filaments among filaments with/without N_2H^+ dense cores are 92% and 65%, respectively, indicating the criticality of filament is an important condition of dense core formation (see details in Section 4.2). The uncertainties of thermal, nonthermal, and total critical line masses are estimated from the uncertainties on the thermal, nonthermal, and total velocity dispersions, respectively.

3.2. Identification of Dense Cores and Their Virial Parameters

N_2H^+ is a common dense gas tracer that gets excited at relatively high densities ($\simeq 10^5 \text{cm}^{-3}$ for $J=1\text{--}0$), and thus, the bright N_2H^+ (1–0) emission can reveal the distribution and morphologies of dense cores. We use the FellWalker algorithm (Berry 2015) in the CUPID package (Berry et al. 2007) in the Starlink software to define the clumpy structures as dense cores in the N_2H^+ (1–0) integrated intensity map. The N_2H^+ (1–0) integrated intensity map of Orion B presented in the background of Figure 14 is produced including intensities of all the hyperfine components. We identified 48 N_2H^+ dense cores in the observed region (see polygons in Figure 14). To determine the LSR velocity and velocity dispersion for each dense core, we perform a hyperfine line fitting using the `curve_fit` function in the SciPy module (Virtanen et al. 2020). The physical information of the identified cores such as the peak intensity positions, and major and minor axes of the cores, their LSR velocities and line widths determined by the hyperfine fitting of the N_2H^+ (1–0) profile, their average N_2H^+ column densities and average H_2 column densities, their average dust temperatures, observed masses, and virial masses, and virial parameters are listed in Table 3.

We derive the N_2H^+ column densities of the dense cores using the N_2H^+ (1–0) emission, following the equation from Caselli et al. (2002) as below:

$$N(\text{N}_2\text{H}^+) = \frac{8\pi W_{\text{int}} g_l}{\lambda^3 A g_u} \frac{1}{J_{\nu}(T_{\text{ex}}) - J_{\nu}(T_{\text{bg}})} \times \frac{1}{1 - \exp(-h\nu/k_B T_{\text{ex}})} \frac{Q_{\text{rot}}}{g_l \exp(-E_l/k_B T_{\text{ex}})}, \quad (9)$$

where W_{int} is the integrated intensity of the N_2H^+ (1–0) emission, λ and ν are the wavelength and frequency of the observed transition, respectively, A is the Einstein coefficient ($=3.628 \times 10^{-5} \text{s}^{-1}$), Q_{rot} is the partition function, and E_l is the energy of the lower level. The statistical weights of the lower-level g_l and the upper-level g_u are 1 and 3, respectively. Using our N_2H^+ (1–0) column density map derived from the N_2H^+ integrated intensity where the S/N ratio exceeds 7 and Herschel H_2 column density, the N_2H^+ fractional abundance $[\text{N}_2\text{H}^+]/[\text{H}_2]=1.6 \pm 0.6 \times 10^{-10}$ is obtained. In deriving the N_2H^+ fractional abundance of the cores using their H_2 column densities, we considered that cores have a single velocity component since the N_2H^+ line profile is not resolved into multiple components. Then, we estimate the H_2 column densities $N(\text{H}_2)$ over the cores using the determined N_2H^+ fractional abundance and observed N_2H^+ (1–0) column densities to calculate the core mass M_{core} by adding the H_2 column densities $N(\text{H}_2)$ over the cores. In these calculations, we used the mean molecular weight per hydrogen molecule μ_{H_2} of 2.8 (Kauffmann et al. 2008). The N_2H^+ core masses range from $0.37\text{--}247 M_{\odot}$ with a median value of $7 M_{\odot}$ and the average uncertainty of core mass is 43%. Note that the several bright N_2H^+ cores in this study are not fully resolved with the current resolution.

Here we examine whether the dense cores form stars or not, by identifying YSOs. Furlan et al. (2016) presented a catalog of 330 YSOs using their $1.2\text{--}870 \mu\text{m}$ spectral energy distributions from the Spitzer Orion Survey (Megeath et al. 2012) and

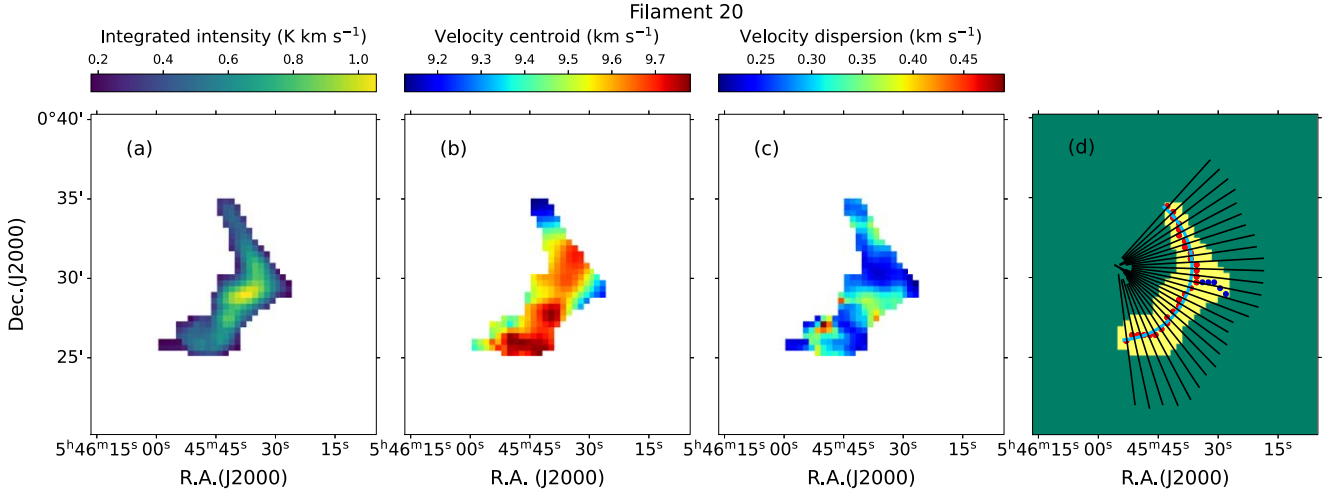


Figure 11. Defining the main properties of the identified velocity-coherent filament. Here, F20 is given as an example. (a) The integrated intensity (for Gaussian area) image. (b) The velocity centroids distribution. (c) The distribution of velocity dispersion. (d) Spine and branch, filament length, and radial cuts of the filament to produce the radial profiles. The path of the spine and branch are indicated with red points and blue points in panel (d). The red dots indicate an additional branch, and the curve (sky blue color) indicates the smoothed path of the spine, which is used for estimating the length of the filament. The black straight thin lines in panel (d) are drawn perpendicularly across the spine at the evenly sampled data points for drawing radial profiles in Figure 12.

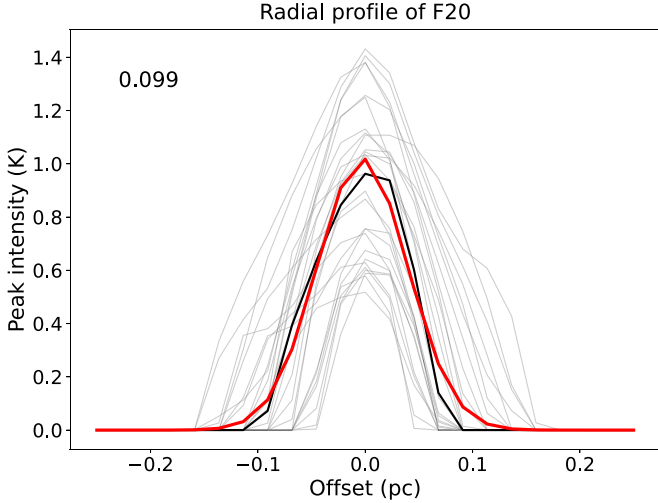


Figure 12. The radial profiles of F20 drawn along the black line cuts in Figure 11(d), which are evenly made with an interval of $25''$. The gray lines represent individual radial profiles and the black line represents the average profile. The red line depicts the Gaussian-fitted profile. The number in the figure is the FWHM of the Gaussian-fitted profile in the unit of pc.

Herschel Orion Protostar Survey (HOPS). In this study, we use this catalog to examine whether the dense cores are protostellar or starless. Among the HOPS sources, 22 Class 0 protostars, 21 Class I protostars, and eight flat-spectrum YSOs are located in the observed cores of this study (see asterisks in Figure 7(d) in red, green, and yellow colors, respectively). If a N_2H^+ dense core has positional coincidence with any protostars, we define it as a N_2H^+ dense core with YSOs. If not, we define it as a starless dense core.

In order to quantify the dynamical balance of the dense core, we determine the virial mass of the N_2H^+ cores using the equation (MacLaren et al. 1988):

$$M_{\text{vir}}^{\text{core}} = \left(\frac{5 - 2e}{3 - e} \right) \frac{3 R_{\text{core}}}{G} \sigma_{\text{tot}, \text{N}_2\text{H}^+}^2, \quad (10)$$

where $R_{\text{core}} (= \sqrt{(R_{\text{maj}} \times R_{\text{min}})^2 - \theta_B^2})$ is the deconvolved radius of the core determined by beam deconvolution of the geometric mean radius of the major radius (R_{maj}) and minor radius (R_{min}) of

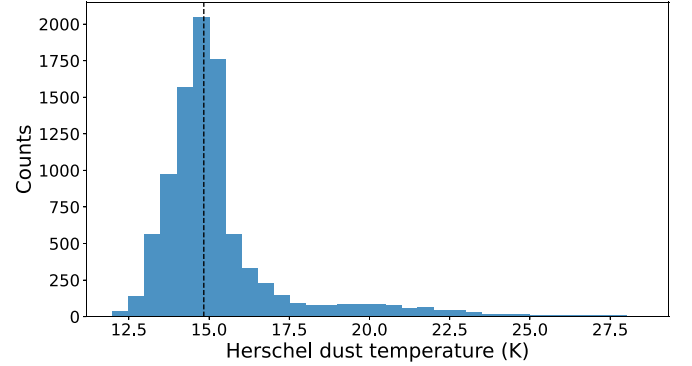


Figure 13. The dust temperatures obtained using the Herschel data toward the filamentary structures. The column densities for the filaments were calculated using these dust temperatures. The cyan vertical line indicates the median value (14.8 K) of the Herschel dust temperature distribution toward the filaments.

the core. $\sigma_{\text{tot}, \text{N}_2\text{H}^+}$ is the total velocity dispersion estimated from Equation (5) using the averaged N_2H^+ (1–0) spectrum of the core, θ_B is the HPBW, and e is a constant depending on the density profile, $\rho(r) \propto r^{-e}$. Assuming that the dense cores have an isothermal density profile in the form of $\rho(r) \propto r^{-2}$, we obtain a correction factor $(5 - 2e)/(3 - e)$ to 1 in this work. The virial parameter, the ratio of virial mass to core mass, $\alpha_{\text{vir}}^{\text{core}} = M_{\text{vir}}^{\text{core}}/M_{\text{core}}$, is measured to examine the dynamical state of the N_2H^+ dense cores. Dense cores with YSOs show the virial parameter in the range of 0.05–1.5 and starless dense cores show the virial parameter in the range of 0.27–7.75 (see Section 4.3 for details). The average uncertainty in $M_{\text{vir}}^{\text{core}}$ is 16% and that in $\alpha_{\text{vir}}^{\text{core}}$ is 46%. The information on the identified dense cores and their estimated physical quantities are listed in Table 3.

4. Discussion

4.1. Comparison of C^{18}O Filaments with Herschel Continuum Filaments

Using the continuum data obtained by the Herschel Gould Belt Survey, Arzoumanian et al. (2019) and Könyves et al. (2020)

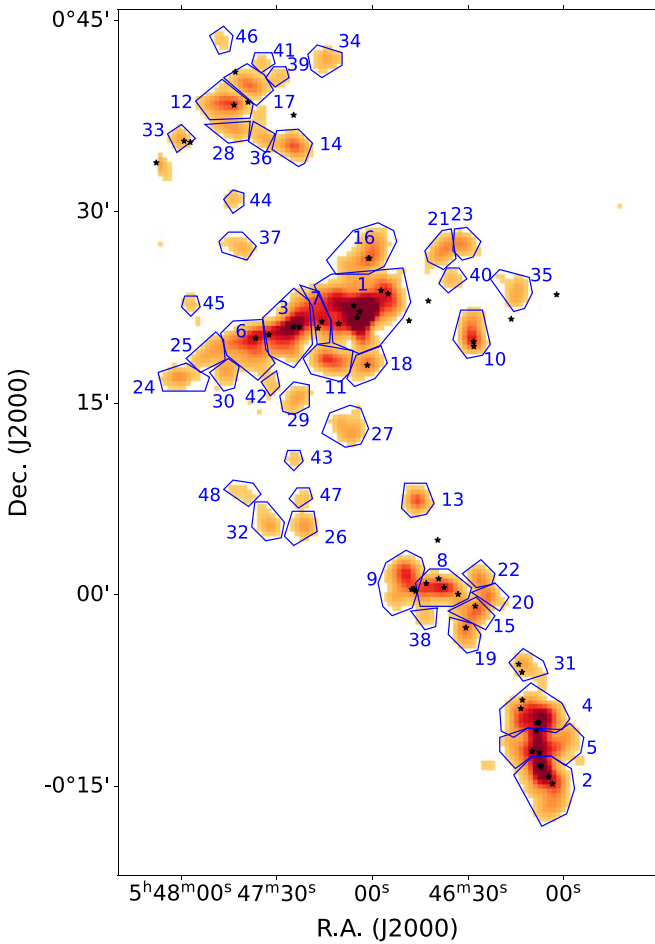


Figure 14. The distribution of N_2H^+ dense cores identified by the FellWalker algorithm in the Orion B region (blue polygons). The color tones indicate the integrated intensity image of the N_2H^+ . Asterisks denote YSOs from Furlan et al. (2016) represented regardless of evolutionary stage. The dense core ID is labeled in a decreasing sequence of peak brightness.

identified filament networks toward the NGC 2068 and NGC 2071 regions. We compare the velocity-coherent filaments identified in this study with the Herschel continuum filaments in Figure 15. Although both the identification methods and the data are different, they are found to be coincident, especially in high-density regions.

Figure 15 shows that Herschel filaments exist not only in the regions where bright C^{18}O filaments are discernible but also in the other regions where C^{18}O filaments are not well defined due to their faintness, mostly due to the better sensitivity in Herschel continuum data. Some Herschel continuum filaments are identified in a single filament only through multiple velocity-coherent filaments where evidently different velocity components exist (e.g., the olive line between F2 and F3, the green line between F19 and F20, and the orange line between F23 and F25). Chung et al. (2021) compared the Herschel continuum filaments and C^{18}O filaments in the IC 5146 molecular cloud, finding similar results. Those results place an important emphasis on the need for velocity information for identifying velocity-coherent structures and studying their dynamical state.

We note that our observations have a coarser spatial resolution than previous studies of similar systems (Hacar et al. 2013; Tafalla & Hacar 2015; Hacar et al. 2018), so they may be missing some smaller-scale fibers like those seen by

previous authors. Observation with higher spatial resolution will be helpful in understanding how large velocity-coherent filaments consist of smaller fiber structures and how they form with their relations.

4.2. Gravitational Stability in Filaments

As the filamentary structures in the clouds are regarded as playing a key role in the formation of dense cores and stars there, it would be highly important to examine whether our identified filaments are gravitationally stable or unstable. In this section, we discuss this matter by looking into the criticalities of the filaments. Most importantly, before determining the gravitational stability of filaments, we divide the filaments into two groups according to the existence of dense cores to explore how gravitational fragmentation occurs along the filament. For this, we determine which core is related to which filament using the velocity centroid of the filament in decomposed C^{18}O (1–0) spectra and the V_{LSR} derived from the hyperfine fitting of the N_2H^+ spectrum at the peak-intensity position in the dense core. Refer to the figures in Appendix B to find the positional and spectral coincidences of dense cores and filaments that lead to define two groups, *the filaments with N_2H^+ dense cores* and *the filaments without N_2H^+ dense cores* (*coreless filaments*).

In Figure 16, filaments having positional coincidences with N_2H^+ dense cores, which we call *the filaments with N_2H^+ dense cores*, are shown in the left panel and *the filaments without N_2H^+ dense cores* are shown in the right panel. The virial parameter of the filament $\alpha_{\text{fil}}^{\text{vir}} = M_{\text{line}}^{\text{crit}}/M_{\text{line}}$ is defined as $M_{\text{line}}^{\text{tot,crit}}/M_{\text{line}}$ and presented in Figure 16 with blue circles with additionally presented $M_{\text{line}}^{\text{th,crit}}/M_{\text{line}}$ (red asterisks) and $M_{\text{line}}^{\text{nth,crit}}/M_{\text{line}}$ (green plus symbols) depending on the contributing motion. For the critical value of $M_{\text{line}}^{\text{tot,crit}}/M_{\text{line}}$, we draw a blue dashed horizontal line at $\alpha = 2$, which is the lowest critical virial parameter proposed for non-magnetized clouds (Kauffmann et al. 2013). Arzoumanian et al. (2013) also used the same criteria for the virial parameter of filament. The estimated critical line masses are tabulated in Table 2, and the given uncertainties of $M_{\text{line}}^{\text{th,crit}}/M_{\text{line}}$, $M_{\text{line}}^{\text{nth,crit}}/M_{\text{line}}$, and $M_{\text{line}}^{\text{tot,crit}}/M_{\text{line}}$ are calculated from the propagation of uncertainties of observational velocity dispersion and line mass.

If the thermal critical line mass $M_{\text{line}}^{\text{th,crit}}$ is larger than the filament’s line mass M_{line} , the filament is thermally supported against the gravitational collapse (i.e., thermally subcritical). On the other hand, the ratio $M_{\text{line}}^{\text{th,crit}}/M_{\text{line}}$ less than unity would indicate that the filamentary structure is under radial collapse or fragmentation (i.e., thermally supercritical).

In the case of the filaments with N_2H^+ cores (left panel of Figure 16), the virial parameters are less than 2, indicating the filamentary structures are gravitationally bound and have environments in which dense cores can be formed. The nonthermal velocity dispersions in units of the speed of sound (σ_{nth}/c_s) for each filament show that most of the filamentary structures are transonic/supersonic (see Section 4.5 and Appendix A). The outlier F9 was identified as a filament containing a core; however, its virial parameter is estimated to be large due to its large nonthermal contribution. The nonthermal velocity dispersion of F9 at the center of Core 37 is probably overestimated since the core spans two nearby filaments, F9 and F10 (see locations of F9 and F10 in the figures in Appendix B). We adopt the critical value of

Table 3
Physical Properties of the Dense Cores in Orion B

Core ID (1)	R.A. (J2000) (2)	Decl. (J2000) (3)	R_{core} (4)	$\langle V_{\text{LSR}} \rangle_{\text{min}}^{\text{max}}$ (5)	$\langle T_{\text{dust}} \rangle$ (6)	σ_{tot} (7)	M_{core} (8)	M_{vir} (9)	$\alpha_{\text{vir}}^{\text{core}}$ (10)	Fil. ID (11)
C1	05:47:03.40	+00:21:59.98	0.13	$9.4_{8.7}^{9.8}$	15.5	0.56 ± 0.03	246.6 ± 96.6	33.1 ± 3.6	0.13 ± 0.05	17
C2	05:46:07.66	-00:13:33.97	0.06	$10.3_{10.1}^{10.4}$	13.6	0.28 ± 0.01	91.0 ± 35.7	5.4 ± 0.4	0.06 ± 0.02	30
C3	05:47:25.40	+00:20:53.98	0.08	$9.3_{9.0}^{9.8}$	15.3	0.42 ± 0.03	101.2 ± 39.7	13.2 ± 1.9	0.13 ± 0.05	17
C4	05:46:07.66	-00:09:31.98	0.03	$10.1_{9.3}^{10.6}$	14.0	0.38 ± 0.02	63.5 ± 25.0	3.6 ± 0.4	0.06 ± 0.02	30
C5	05:46:07.66	-00:12:05.97	0.04	$10.0_{9.7}^{10.3}$	13.5	0.37 ± 0.02	81.4 ± 31.9	5.0 ± 0.5	0.06 ± 0.03	30
C6	05:47:37.13	+00:20:09.97	0.03	$9.2_{9.0}^{9.4}$	14.7	0.28 ± 0.02	54.2 ± 21.3	2.9 ± 0.4	0.05 ± 0.02	17
C7	05:47:16.60	+00:21:37.98	0.09	$9.3_{9.1}^{9.8}$	15.3	0.42 ± 0.03	34.8 ± 13.6	14.5 ± 2.1	0.42 ± 0.17	17
C8	05:46:38.46	+00:00:44.00	0.10	$10.4_{10.0}^{10.8}$	18.7	0.40 ± 0.01	31.3 ± 12.3	15.3 ± 0.8	0.49 ± 0.19	30
C9	05:46:48.73	+00:01:28.00	0.10	$10.9_{10.7}^{11.1}$	19.9	0.25 ± 0.01	37.0 ± 14.6	8.5 ± 0.7	0.23 ± 0.09	30
C10	05:46:28.20	+00:20:09.99	0.08	$9.5_{9.4}^{9.6}$	14.0	0.18 ± 0.01	24.5 ± 9.7	4.5 ± 0.5	0.18 ± 0.08	17
C11	05:47:13.66	+00:18:19.98	0.09	$10.2_{10.1}^{10.4}$	20.5	0.31 ± 0.02	23.7 ± 9.3	9.8 ± 1.3	0.41 ± 0.17	23
C12	05:47:44.46	+00:38:29.91	0.09	$8.9_{8.6}^{9.7}$	13.4	0.37 ± 0.02	26.0 ± 10.3	11.4 ± 1.2	0.44 ± 0.18	6
C13	05:46:45.80	+00:07:19.99	0.06	$10.6_{10.6}^{10.7}$	22.4	0.21 ± 0.01	9.4 ± 3.8	5.0 ± 0.5	0.53 ± 0.22	23
C14	05:47:25.40	+00:35:11.94	0.07	$9.0_{8.9}^{9.1}$	13.8	0.17 ± 0.01	13.8 ± 5.5	3.8 ± 0.4	0.27 ± 0.11	6
C15	05:46:26.73	-00:01:05.99	0.08	$10.4_{10.0}^{10.7}$	15.6	0.59 ± 0.04	14.2 ± 5.6	21.2 ± 2.9	1.50 ± 0.62	30
C16	05:47:01.93	+00:26:23.98	0.05	$9.8_{9.6}^{9.9}$	14.3	0.21 ± 0.01	26.6 ± 10.7	2.8 ± 0.3	0.11 ± 0.04	17
C17	05:47:38.60	+00:39:57.91	0.08	$9.5_{9.3}^{9.6}$	13.4	0.26 ± 0.02	12.4 ± 5.0	5.8 ± 0.9	0.47 ± 0.20	...
C18	05:47:01.93	+00:17:57.99	0.07	$9.6_{9.4}^{9.7}$	21.1	0.29 ± 0.03	9.8 ± 3.9	7.7 ± 1.6	0.79 ± 0.36	13
C19	05:46:31.13	-00:02:33.99	0.07	$10.3_{10.2}^{10.6}$	14.9	0.28 ± 0.02	12.2 ± 4.8	6.0 ± 0.8	0.49 ± 0.21	30
C20	05:46:23.79	+00:00:00.00	0.06	$10.3_{9.5}^{11.0}$	20.1	0.82 ± 0.05	4.8 ± 1.9	31.5 ± 3.8	6.58 ± 2.77	...
C21	05:46:37.00	+00:27:07.99	0.07	$9.1_{8.8}^{9.2}$	12.9	0.28 ± 0.04	12.7 ± 5.1	5.6 ± 1.6	0.44 ± 0.22	17
C22	05:46:26.73	+00:01:06.00	0.06	$11.1_{11.1}^{11.2}$	17.5	0.24 ± 0.02	3.5 ± 1.4	4.6 ± 0.8	1.33 ± 0.59	23
C23	05:46:32.60	+00:27:29.99	0.06	$8.9_{8.8}^{9.0}$	13.0	0.31 ± 0.03	5.4 ± 2.2	5.5 ± 1.1	1.02 ± 0.46	17
C24	05:48:00.59	+00:16:51.97	0.07	$8.6_{8.5}^{8.8}$	13.6	0.30 ± 0.03	8.0 ± 3.3	6.5 ± 1.3	0.81 ± 0.37	...
C25	05:47:47.39	+00:19:25.97	0.08	$9.0_{8.9}^{9.2}$	13.6	0.28 ± 0.03	11.7 ± 4.6	7.0 ± 1.5	0.59 ± 0.27	17
C26	05:47:20.99	+00:05:29.99	0.06	$10.9_{10.8}^{10.9}$	15.0	0.21 ± 0.02	6.0 ± 2.5	4.1 ± 0.8	0.68 ± 0.31	23
C27	05:47:06.33	+00:12:27.99	0.08	$10.5_{10.4}^{10.6}$	17.1	0.29 ± 0.02	8.7 ± 3.6	8.0 ± 1.1	0.93 ± 0.41	23
C28	05:47:43.00	+00:36:17.92	0.07	$9.0_{8.8}^{9.0}$	12.9	0.21 ± 0.02	7.7 ± 3.1	4.3 ± 0.8	0.56 ± 0.25	6
C29	05:47:23.93	+00:15:23.98	0.06	$10.0_{10.0}^{10.1}$	17.3	0.19 ± 0.02	4.6 ± 1.9	4.0 ± 0.8	0.87 ± 0.41	23
C30	05:47:45.93	+00:17:35.97	0.06	$9.0_{8.8}^{9.2}$	14.0	0.30 ± 0.03	6.9 ± 2.8	5.6 ± 1.1	0.82 ± 0.37	17
C31	05:46:13.53	-00:05:29.99	0.07	$9.6_{9.5}^{9.7}$	15.2	0.22 ± 0.02	3.9 ± 1.7	4.4 ± 0.8	1.12 ± 0.53	30
C32	05:47:32.73	+00:05:29.99	0.07	$11.4_{11.3}^{11.5}$	14.3	0.15 ± 0.01	4.5 ± 2.0	3.2 ± 0.4	0.70 ± 0.32	22
C33	05:48:00.60	+00:35:55.91	0.05	$9.6_{9.6}^{9.7}$	14.0	0.20 ± 0.02	2.7 ± 1.1	3.1 ± 0.6	1.15 ± 0.53	8
C34	05:47:15.13	+00:42:09.92	0.06	$8.6_{8.5}^{8.7}$	13.7	0.17 ± 0.01	4.9 ± 2.1	3.2 ± 0.4	0.65 ± 0.29	4
C35	05:46:15.00	+00:23:27.99	0.07	$9.6_{9.4}^{11.0}$	14.0	0.16 ± 0.01	5.2 ± 2.3	3.5 ± 0.4	0.68 ± 0.31	17
C36	05:47:34.20	+00:35:55.93	0.06	$9.0_{8.9}^{9.0}$	13.2	0.18 ± 0.01	3.7 ± 1.6	3.4 ± 0.4	0.91 ± 0.39	6
C37	05:47:41.53	+00:27:29.95	0.06	$9.2_{9.1}^{9.2}$	13.8	0.10 ± 0.01	3.6 ± 1.6	3.2 ± 0.6	0.88 ± 0.43	9
C38	05:46:42.86	-00:01:49.99	0.05	$11.2_{11.2}^{11.3}$	15.6	0.43 ± 0.01	1.4 ± 0.7	8.2 ± 0.4	5.90 ± 2.89	30
C39	05:47:29.80	+00:40:41.91	0.05	$9.2_{9.2}^{9.2}$	13.4	0.19 ± 0.02	1.2 ± 0.6	2.7 ± 0.6	2.20 ± 1.09	3
C40	05:46:35.53	+00:24:33.99	0.05	$8.0_{8.0}^{8.0}$	13.4	0.13 ± 0.01	1.8 ± 0.8	2.1 ± 0.3	1.18 ± 0.55	18
C41	05:47:34.20	+00:41:47.90	0.04	$9.3_{9.3}^{9.3}$	13.6	0.17 ± 0.01	0.6 ± 0.4	2.2 ± 0.3	3.64 ± 2.29	3
C42	05:47:31.26	+00:16:29.98	0.05	$9.4_{9.3}^{9.4}$	16.5	0.26 ± 0.02	0.5 ± 0.3	4.1 ± 0.6	7.75 ± 4.19	17
C43	05:47:23.93	+00:10:37.99	0.04	$10.6_{10.6}^{10.7}$	16.1	0.11 ± 0.01	0.5 ± 0.2	1.6 ± 0.3	3.54 ± 1.95	23
C44	05:47:43.00	+00:30:47.94	0.04	$9.2_{9.2}^{9.3}$	15.1	0.18 ± 0.02	1.1 ± 0.5	2.5 ± 0.6	2.34 ± 1.17	...
C45	05:47:57.66	+00:22:43.95	0.04	$10.0_{10.0}^{10.0}$	14.5	0.10 ± 0.01	0.7 ± 0.4	1.6 ± 0.3	2.31 ± 1.28	8
C46	05:47:47.40	+00:43:37.88	0.05	$9.8_{9.8}^{9.8}$	14.0	0.10 ± 0.01	0.8 ± 0.6	1.9 ± 0.4	2.33 ± 1.75	3
C47	05:47:20.99	+00:07:41.99	0.05	$10.6_{10.6}^{10.6}$	15.3	0.10 ± 0.01	0.7 ± 0.4	2.0 ± 0.4	2.67 ± 1.66	23
C48	05:47:40.06	+00:08:03.99	0.07	$11.2_{11.2}^{11.3}$	13.6	0.19 ± 0.03	0.4 ± 0.2	3.1 ± 1.0	8.35 ± 4.53	22

Notes. Column 1: core name given in order of its peak intensity, from the highest to the lowest. Column 2 and Column 3: coordinates at peak intensity positions of cores. Column 4: the deconvolved core size as the geometric mean of major and minor axis size assuming its elliptical shape in units of parsecs. Column 5: the LSR velocity obtained from hyperfine fitting of the N_2H^+ (1–0) spectrum in units of kilometers per second. Column 6: the average dust temperature of the dense core in units of kelvin. Column 7: the average total velocity dispersion of the dense core from the N_2H^+ (1–0) line profiles. Column 8 and Column 9: the core mass and its virial mass in units of solar mass. Column 10: the core virial parameter, the ratio of the core mass to the virial mass. Column 11: the name of the filament surrounding the core.

(This table is available in machine-readable form.)

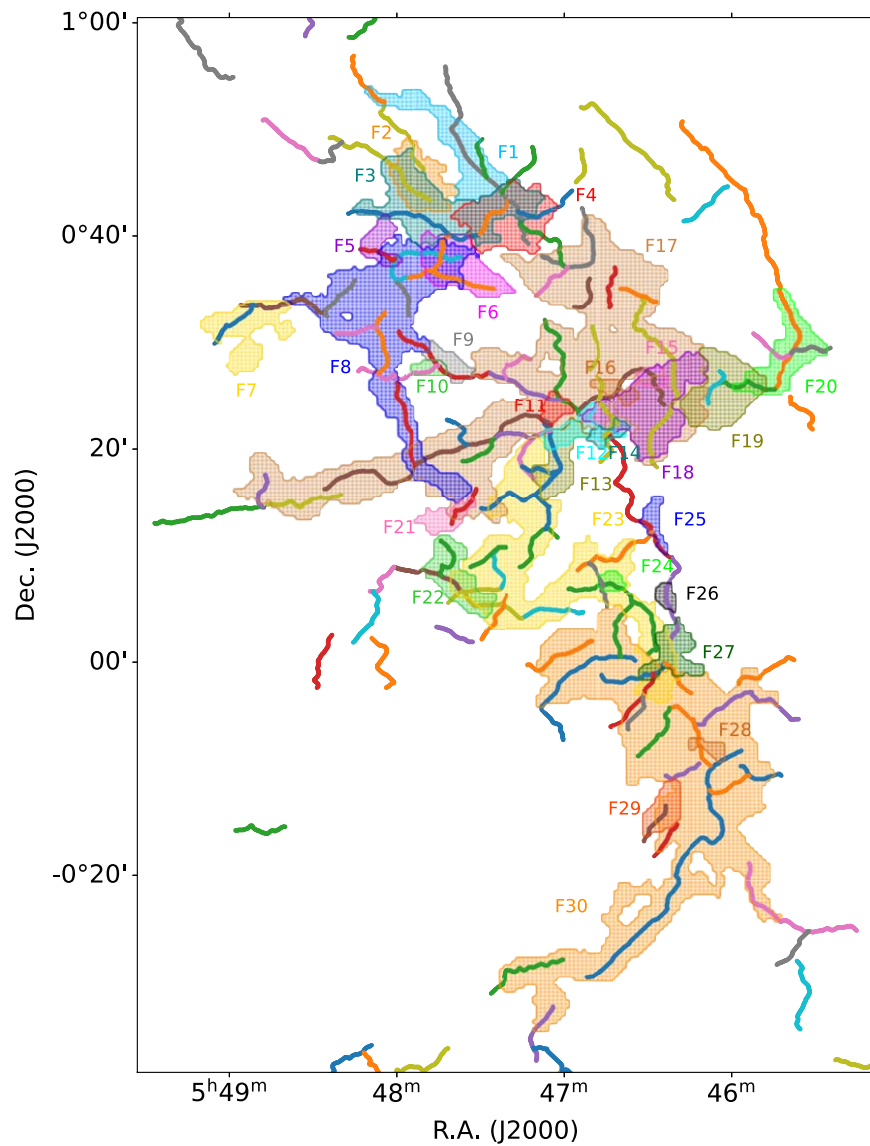


Figure 15. The velocity-coherent filaments and Herschel continuum filaments. The velocity-coherent filaments identified with the $C^{18}O$ (1–0) line emission in this study are presented by colored shades with their filament names. The Herschel continuum filaments defined by Arzoumanian et al. (2019) using a Herschel column density map are indicated with curved lines.

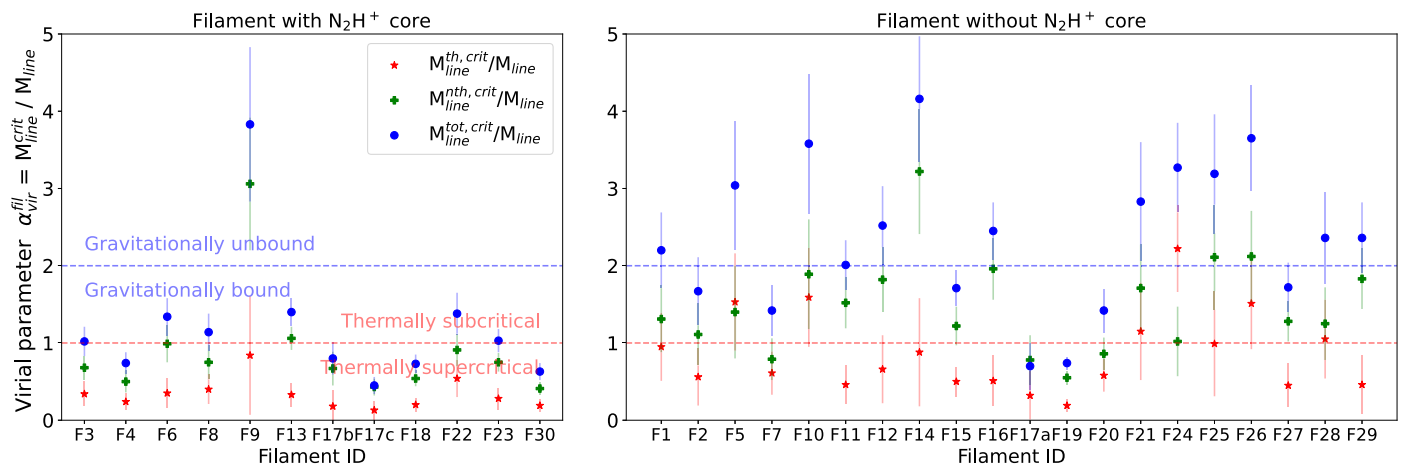


Figure 16. Virial parameters for the filaments with (left panel) and without (right panel) dense cores. The virial parameters for the filaments derived considering thermal support only, nonthermal support only, and both thermal plus nonthermal support are represented by a red asterisk, green plus, and blue circle symbols, respectively. The horizontal lines indicate the filament’s virial parameter (M_{line}^{crit}/M_{line}) of 2 (blue dashed line) and unity (red dashed line).

$M_{\text{line}}^{\text{th,crit}}/M_{\text{line}} \sim 1$ (red dashed horizontal line) to judge whether the filament is in a thermally subcritical or supercritical state (Arzoumanian et al. 2013). As shown in the left panel of Figure 16, the ratio between $M_{\text{line}}^{\text{th,crit}}$ and M_{line} (red asterisks) presents that filaments with dense cores are all thermally supercritical as several previous studies have shown that dense cores form mostly within supercritical filaments (André et al. 2010; Polychroni et al. 2013; Könyves et al. 2015). On the other hand, coreless filaments (right panel of Figure 16) do not present consistent features. Some filaments (F2, F19, F20, and F27) are thermally supercritical and present virial parameters, for all the filaments but F9, less than 2 (gravitationally bound). Those filaments may have an environment potentially capable of forming dense cores. The other filaments (F5, F12, F14, F16, F21, F25, and F29) are gravitationally unbound and may disperse due to nonthermal contribution. Note that several filaments, F1, F7, and F17a, were not fully observed in N_2H^+ (1–0), and thus the existence of N_2H^+ cores could not be tested.

All filaments (except F5) have larger $M_{\text{line}}^{\text{nth,crit}}$ than $M_{\text{line}}^{\text{th,crit}}$ by a factor of 2–4, indicating that the effects of nonthermal motions are significant throughout the entire molecular cloud. The Mach numbers ($=\sigma_{\text{nth}}/c_s$) along the filament’s spine indicate that the filament has transonic or supersonic motions over those regions (see also the figures in Appendix A for details of the properties of each filament).

In the Taurus L1495/B213 molecular cloud, one group of their filaments (sterile fibers) does not contain cores, but the other group (fertile fibers) contains around three cores on average (Tafalla & Hacar 2015). According to their result, filaments either have no cores or have multiple cores, indicating that the distribution of cores between filaments may not be made randomly, but somehow systematically. This is consistent with the idea that if a filament is unstable ($M_{\text{line}} > M_{\text{line}}^{\text{th,crit}}$) for fragmentation, it will likely make several cores, while if it is stable ($M_{\text{line}} < M_{\text{line}}^{\text{th,crit}}$), it will make none. Figure 17 shows the number of cores per filament. The number of dense cores is zero for filaments in a stable state ($M_{\text{line}}/M_{\text{line}}^{\text{crit}} < 1$). For filaments in an unstable state ($M_{\text{line}}/M_{\text{line}}^{\text{crit}} > 1$), the larger $M_{\text{line}}/M_{\text{line}}^{\text{crit}}$ tends to have a large number of dense cores in the filament. Hence, understanding the criticality of a filament can provide insights into the fragmentation of filaments and the formation of dense cores /YSOs. Note that the presence of YSOs in filaments with no dense core, F11, F12, F14, F19, and F27 (green star symbol in Figure 17) is ambiguous to properly interpret, since some YSOs are located in the overlapping region between two filaments (e.g., F11, F12, and F14 are sharing YSOs with F17b, and F27 shares a YSO with F30).

4.3. Virial State of the N_2H^+ Dense Cores

In molecular clouds that are gravitationally collapsing, gravity dominates the energy balance, and the kinetic energy and the absolute value of gravitational energy become comparable, putting the system in virial equilibrium. The equipartition between gravity and kinetic energy approaches $\alpha_{\text{vir}}^{\text{core}} (=M_{\text{vir}}^{\text{core}}/M_{\text{core}}) = 2$ for nonmagnetic, uniformly density spheres (Vázquez-Semadeni et al. 2007; Ballesteros-Paredes et al. 2011; Ramírez-Galeano et al. 2022).

In the case of $\alpha_{\text{vir}}^{\text{core}} < \alpha_{\text{crit}}$, the gravitational binding energy is more significant than the kinetic energy, and thus, the dense core is gravitationally unstable and can collapse. On the other hand, if $\alpha_{\text{vir}}^{\text{core}} > \alpha_{\text{crit}}$, the kinetic energy is dominant over the

gravitational energy, so that the dense core is gravitationally unbound and unlikely to form young stars.

Figure 18 presents the virial parameters of dense cores as a function of the core mass derived from N_2H^+ (1–0). The virial parameter is inversely proportional to the core mass, with a power-law index of -0.7 for this region. N_2H^+ cores with YSOs (left panel of Figure 18) have $\alpha_{\text{vir}}^{\text{core}}$ of 0.05–1.5 (the average value of $\alpha_{\text{vir}}^{\text{core}}$ is 0.44). All cores with YSOs have $\alpha_{\text{vir}}^{\text{core}}$ lower than the critical value, indicating that they are likely gravitationally bound. On the other hand, starless N_2H^+ cores (right panel of Figure 18) have $\alpha_{\text{vir}}^{\text{core}}$ of 0.27–7.75 with an average value of 1.85, indicating that some of them are gravitationally bound and others are not. It is also noted that starless cores over $2 M_{\odot}$ tend to be gravitationally unstable.

In a study by Ohashi et al. (2016), dense cores in the infrared dark cloud G14.225-0.506 and their parental filaments show a trend that their virial parameters decrease with decreasing scales from filament to clump to dense cores (see Figure 6 in Ohashi et al. 2016). Figure 19 shows the virial parameters of the characteristic scales of dense cores (the deconvolved radius R_{core}) and filaments (the filament lengths L). In Ohashi et al. (2016), the virial parameters of prestellar cores and protostellar cores were indistinguishable. In our result, however, this is not the case. All the dense cores with YSOs have $\alpha_{\text{vir}}^{\text{core}} < 2$ while nearly half of the starless cores have $\alpha_{\text{vir}}^{\text{core}} > 2$. In the case of filaments, we divide them into filaments with (blue dots) and without (black open circles) dense cores. The filaments in the gravitationally bound state ($\alpha_{\text{vir}}^{\text{fil}} < 2$) tend to produce dense cores, and dense cores with a virial parameter less than its critical value tend to be in a more active star-forming environment. We also observed a decreasing trend with decreasing characteristic scale from filament to core when we take gravitationally bound samples (blue dots and red dots in Figure 19).

However, we note that the virial parameter alone cannot strongly represent the environmental feature of star formation (note also the large uncertainty of $\alpha_{\text{vir}}^{\text{core}} \sim 46\%$). Further investigation of the dynamical and chemical status of the dense cores with molecular lines can provide supplementary factors for understanding the evolutionary status of the dense cores (Section 4.7). Furthermore, the N_2H^+ dense cores identified in this study are not fully resolved with the current angular resolution ($\theta_B \sim 54''$). Therefore, observation with higher angular resolution is needed to better examine core properties with virial analysis.

4.4. Kinematic Information of Filaments

Discussions on the difference between the systemic velocities of filaments and dense cores have been made in several studies to investigate how the cores form in the filaments. (Kirk et al. 2007; Hacar & Tafalla 2011; Chung et al. 2019, 2021). A core-to-envelope velocity difference less than the speed of sound may imply that they share similar kinematics from core to filament scale. Figure 20 shows that the systemic velocities of C^{18}O (1–0) and N_2H^+ (1–0) have a tight correlation with a difference of less than 0.23 km s^{-1} (speed of sound at 14.8 K, the median value of dust temperature in Figure 13). The systemic velocities of C^{18}O and N_2H^+ spectra were obtained from either single Gaussian fits for each component in C^{18}O or multiple Gaussian fits for the hyperfine components in N_2H^+ spectra, respectively. We independently give the initial guesses and conditions for

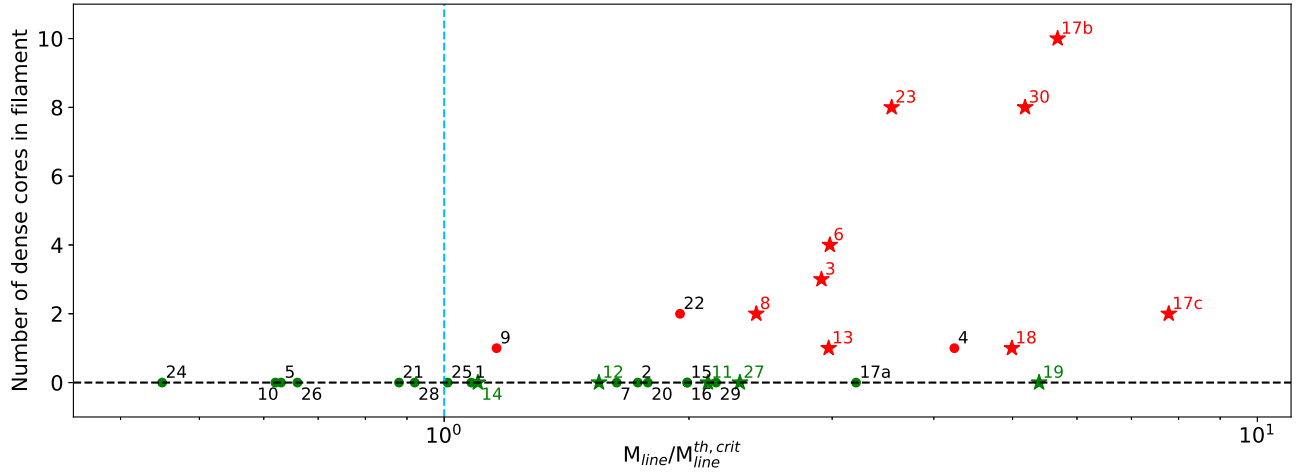


Figure 17. Number of dense cores in each filament as a function of the ratio between M_{line} and $M_{\text{line}}^{\text{th,crit}}$. The cyan vertical line indicates the location where the M_{line} equals $M_{\text{line}}^{\text{th,crit}}$ and the black dashed line shows the location where the filament does not contain any dense core. The circle and asterisk symbols indicate that the filaments do not contain any YSOs and do contain YSOs, respectively. Colors distinguish the filaments with dense cores (red) from the filaments without dense cores (green). The numbers indicate the filament’s ID.

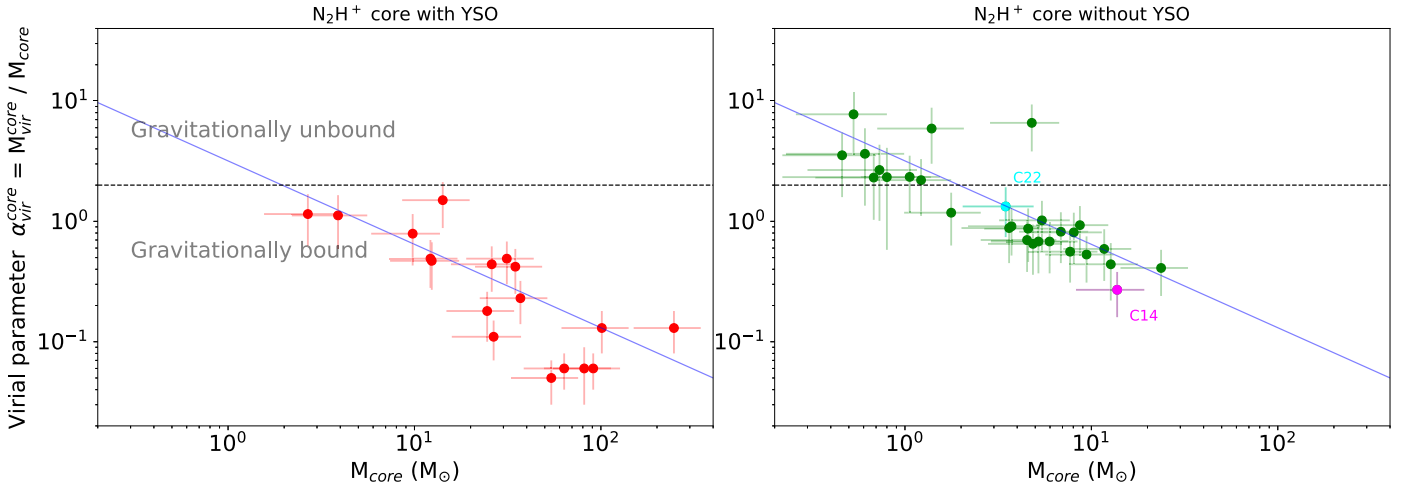


Figure 18. Virial parameters for the dense cores with (left panel) and without (right panel) YSOs. The horizontal line marks the location of the critical value of the virial parameter, $\alpha_{\text{crit}} = 2$. The blue line indicates the best fit of data points with a power-law index of -0.7 . Magenta and cyan circles are to indicate the starless dense cores C14 and C22 with NH_2D detection (see Section 4.7).

finding best-fit results. The velocity coincidence between filaments and related dense cores indicates that dense cores and the surrounding filaments move together with a close kinematical relation between two objects. We are not able to find any significant difference between the two groups, the dense cores with (green dots) and without (blue dots) YSOs.

The outlier in Figure 20 (dense core C37) is located at the border between F9 and F10 (see also the note in Section 4.2). F9 and F10 have slightly different velocity ranges within the speed of sound (refer to Column 5 in Table 2). However, they are distinguishable by identification criteria in this study. Since the position of the emission peak of C37 belongs to the region of F9, we define that the dense core C37 is related to F9. The ambiguity may be solved in further studies with higher angular and spectral resolutions.

As we mentioned in the last paragraph of Section 3.1.1, the V_{LSR} spans $\sim 4 \text{ km s}^{-1}$ throughout the entire cloud material and the average range of internal velocities of each filament is about 0.7 km s^{-1} (see Column 5 in Table 2). In order to evaluate whether the velocity change comes from velocity dispersion due to internal structures or the large-scale velocity gradient

along the filament, we trace the changes of intensity and velocity centroid along the spine of the filaments in the right-middle panel of Figure 21 (see also the figures in Appendix A). In the case of F23 in Figure 21, for example, there is a large-scale change of systemic velocity along the filament from south to north, with the approximate end-by-end velocity gradient of $0.26 \text{ km s}^{-1} \text{ pc}^{-1}$. Monotonic large-scale gradients are also seen in F8 ($0.4 \text{ km s}^{-1} \text{ pc}^{-1}$) and F17b ($0.2 \text{ km s}^{-1} \text{ pc}^{-1}$) with local velocity fluctuations at the sub-parsec scale (see also the figures in Appendix A for the properties of the other filaments harboring dense cores). If the gas flow is converging to the core center, the velocity field would reverse at the density peak position of the core. Such a pattern of velocity field is observed in surrounding filaments around several N_2H^+ cores (e.g., C39 and C41 in F3, C12 in F6, C14 in F6, C33 in F8, C40 in F18, C27 in F23, and C26 in F23).

In most filaments and their dense cores, the velocity dispersions are smaller in dense cores than in the surrounding filament clouds, while the velocity centroids of the filaments and cores are nearly identical. However, in the case of F17b (Figure 28), the velocity centroids for massive dense cores

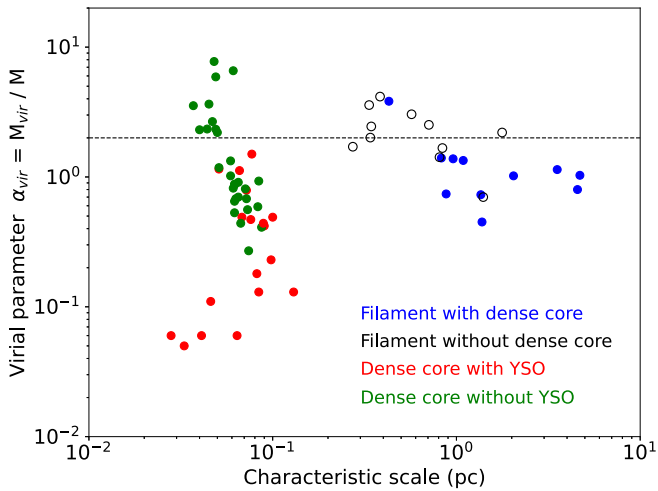


Figure 19. Virial parameters for the dense cores and filaments as a function of their characteristic scales. The characteristic scale is given as the deconvolved core radius R_{core} for dense cores and the filament length L for filaments. Red and green-filled circles indicate dense cores with and without YSOs, respectively. Blue-filled and black open circles indicate filaments with and without dense cores, respectively. The horizontal line marks the virial parameter of 2.

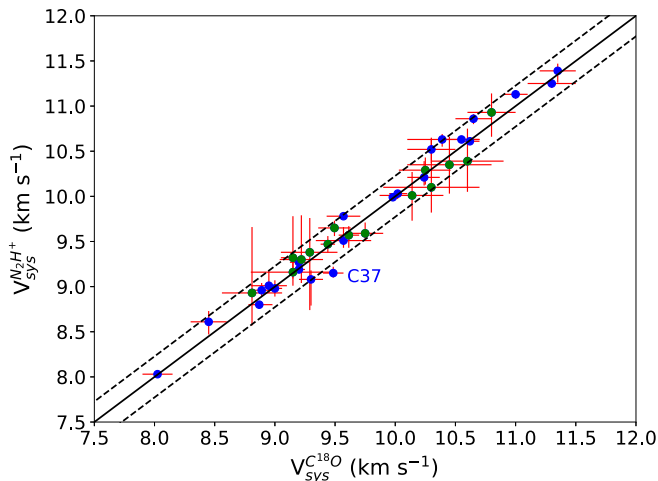


Figure 20. The systemic velocities of dense cores measured by N_2H^+ (1–0) spectra in comparison with those of surrounding filaments obtained by C^{18}O (1–0) spectra. Green and blue dots represent dense cores with and without YSOs. Red bars indicate 1σ error bars for both data sets. A solid line indicates the result for the least-squares fit for the data and dashed lines show the range from the fit result by the speed of sound of 0.23 km s^{-1} , at the average dust temperature of 14.8 K .

(especially for C1, C3, and C7) spread over a remarkably larger range than those in the dense cores along other filaments. Moreover, the nonthermal velocity dispersions of these cores (C1, C3, and C7) are larger than that of F17b, contrary to the expectation that the turbulent motions of dense cores would be usually lower than their surrounding filaments. One of the most massive filaments, F30, also contains massive cores (C2, C4, and C5), which have a wide range of velocity dispersion. These distributions of centroid velocities and velocity dispersions of the cores can be explained as these cores are in a very complex location with a large number of YSOs and possible inflows along the filaments. The density and velocity structures given by F17, F18, and other several small filaments around the brightest dense core C1 appear to be very dynamic, almost like those shown in a hub-filament system (Myers 2009;

Peretto et al. 2013). It is likely possible that these structures can be split into a number of individual overlapping filaments as a result of our choice of low-velocity difference used in the last step of the FoF algorithm in this study.

4.5. A Possible Longitudinal Fragmentation in a Filament

The left panel of Figure 21 shows how the dense cores (polygons) are distributed in the filament F23 (color tone). Eight dense cores (C22, C13, C26, C47, C43, C27, C29, and C11) from south to north, marked with blue polygons) are located along the curved filament with similar V_{LSR} . We also found the other dense cores of the filament in space or velocity dimension, which are drawn with green polygons. Note that the dense cores associated with the filament F23 do not contain any YSOs, implying that the dense cores in F23 are not yet fully evolved to form protostars.

The right three panels of Figure 21 show the distributions of integrated intensity of F23, velocity centroids, and Mach number, defined as σ_{nth}/c_s , along the spine of filament and dense cores located in the filament. The red arrow in the left panel of Figure 21 indicates the scanning direction along the spine of the filament to trace the property changes. We present the locations of dense cores along F23 with blue dashed vertical lines in the three right panels. The right-upper panel of Figure 21 shows the variation of C^{18}O (1–0) integrated intensity distribution along the filament main axis. The positions of dense cores are generally well matched to the filament’s intensity peaks along the spine. However, along the density fluctuation, there are three additional bumps at offset ~ 1 , ~ 1.9 , and $\sim 2.3 \text{ pc}$ (see purple vertical dashed lines) where no dense cores are detected. So we believe that these are less dense fragments (H1, H2, and H3) where the N_2H^+ (1–0) emission is not strong enough to be detected, but possibly any dense core may form in the future. Using the positions of both identified dense cores and possible core-forming regions in the future, we derive an average separation of 0.39 pc (vertical line in Figure 22) from the quasiperiodic locations of the fragments on the plane of the sky.

To explain the quasiperiodic inter-core separation, we bring an analytic theory on the instability that describes the gravitational collapse of isothermal filaments. Inutsuka & Miyama (1992) proposed that a self-gravitating cylinder becomes unstable when the line mass is greater than its thermal critical line mass and then fragments with a separation of 4 times the width of the cylinder. Observational evidence supporting the gravitational fragmentation scenario has been reported on various scales (Wang et al. 2011; Tafalla & Hacar 2015; Orkisz et al. 2019; Shimajiri et al. 2019; Zhang et al. 2020).

The line mass of F23 ($104 M_{\odot}$) is 3.6 times larger than its thermal critical line mass ($29 M_{\odot}$). Sufficient line mass supports the underlying condition of the theory on longitudinal fragmentation. The width of F23 is estimated to be 0.13 pc and the average separation is 0.39 pc , which is in fairly good agreement with the expectation from the theory ($4 \times$ width of F23 $\sim 0.52 \text{ pc}$).

However, several issues need to be addressed before reaching a definitive conclusion about the fragmentation process associated with the formation of dense cores in the filamentary clouds in Orion B.

First of all, our measured separation is the one projected on the plane of the sky. Thus, this separation would be fairly

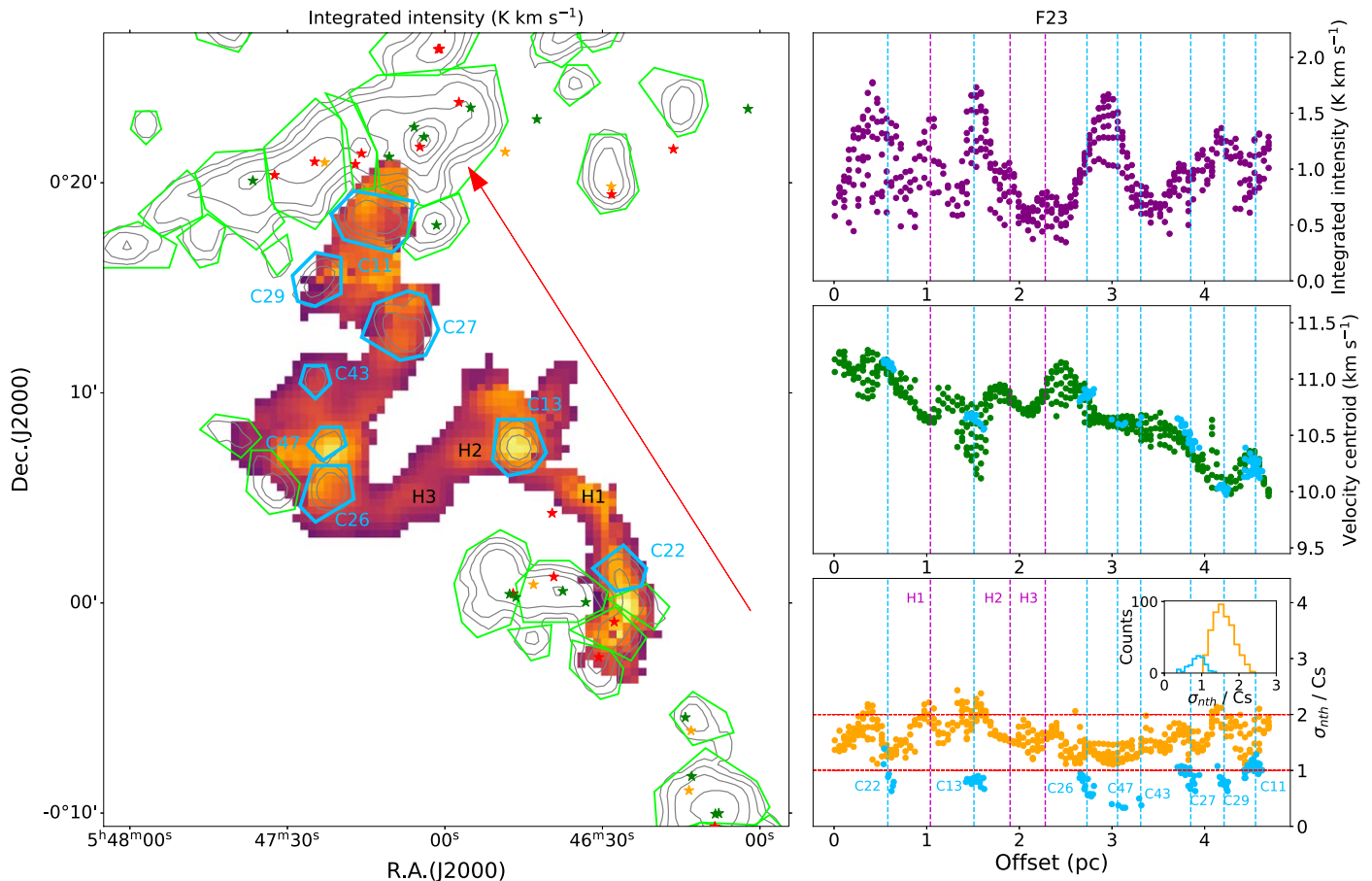


Figure 21. Left panel: the distribution of the YSOs and the dense cores in the $C^{18}O$ (1–0) filament F23. The color tone indicates the image of the $C^{18}O$ (1–0) integrated intensity. The contours indicate the integrated intensity levels of N_2H^+ (1–0) [0.08, 0.3, 0.8, 2.0, 4.0, 6.0, 8.0, 10.0] $K km s^{-1}$ in. The blue and green polygons display the dense cores seemingly associated with the filament in LSR velocities and the dense cores not associated with the filament, respectively. The asterisks indicate YSOs classified in Furlan et al. (2016). Red: Class 0 protostars. Green: Class I protostars. Orange: flat-spectrum YSOs. Right-upper panel: the variation of the integrated intensity along the filament spine. The red line displays the averaged intensity variation. Right-middle panel: The variation of the velocity centroids along the filament spine from $C^{18}O$ (1–0) (green dots) and the dense cores from N_2H^+ (1–0) (blue dots) associated with the filament. Right-lower panel: the variation of the nonthermal velocity dispersion divided by the speed of sound along the spine of the filament. The orange and blue dots are estimated from $C^{18}O$ (1–0) (for filaments) and N_2H^+ (1–0) (for dense cores), respectively. The vertical dashed lines are representative positions of the dense cores embedded in the filament (the blue polygons in the left panel). Red horizontal lines indicate the locations for the Mach numbers ($=\sigma_{nth}/c_s$) of 1 and 2. The inset shows histograms of the Mach number distributions of filaments and cores with the same colors as the ones in the main plots.

consistent with the theoretical separation that can result from the gravitational fragmentation in the isothermal filament, when the inclination angle between the filament’s major axis and the plane of the sky is close to 40° . Since the filament is not perfectly straight, the geometrical effect can also influence the oscillation pattern and the evolution of clumps (Gritschneider et al. 2017).

We also note the theoretical expectation in Inutsuka & Miyama (1992) does not consider the effects of magnetic fields. A magnetic field perpendicular to the filament axis can suppress fragmentation and reduce the growth rate of instability (Hanawa et al. 2017). On the other hand, a magnetic field parallel to the filament axis does not suppress the instability of the filament (Hanawa et al. 1993), and can even produce a core spacing comparable to the filament diameter, if it has a high magnetic field strength (Nakamura et al. 1993). In fact, the study of Könyves et al. (2020) may show the case. In that study the cores were identified as 3 times smaller scale than ours (see also Section 4.1) for the same region of Orion B as our study and the median value of ~ 0.14 pc Herschel core separation is equivalent to the typical width (~ 0.10) pc of Herschel

filaments, implying that the core separation can be dependent with the tracing scale or some physical conditions that are not well known. Hence, further studies including information on magnetic fields (e.g., orientation, strength) are needed to understand the fragmentation of the internal structure of the filament in the Orion B.

In order to study the dynamics of the dense cores and the surrounding material, we compare the velocity centroids of N_2H^+ and $C^{18}O$ emissions in the right-middle panel of Figure 21. As the figure shows, the systemic velocities of N_2H^+ cores present a close correlation with those of the surrounding material of the filament.

The Mach number along the filaments estimated with $C^{18}O$ spectra is distributed between 1 and 2, indicating that the motions in the filament are mostly transonic (see panel (i) of Figure 28 in Appendix A). On the other hand, the Mach number measured from N_2H^+ (1–0) inside the dense cores associated with the filament is $\lesssim 1$ indicating that the N_2H^+ dense cores are transonic/subsonic. The inset in the right-bottom panel of Figure 21 presents the histograms for the distribution of the measurements of Mach numbers for both

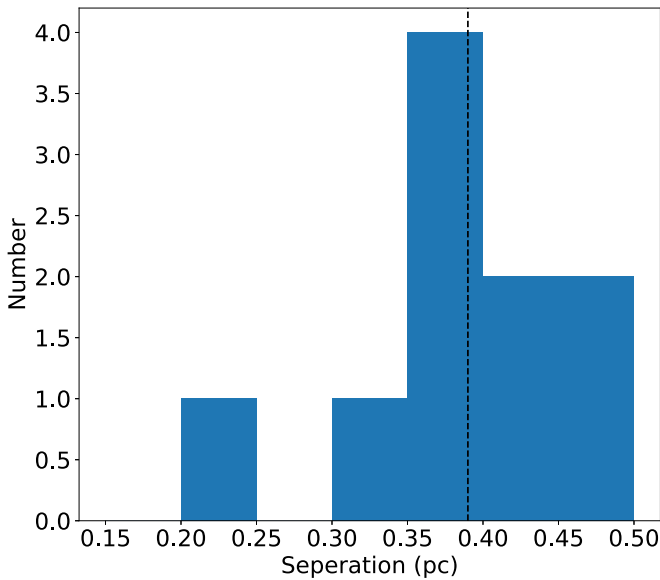


Figure 22. The histogram of core-to-core separations in the filament F23 using offset positions of identified N_2H^+ dense cores and less dense, but possible core-forming regions in the future. The vertical line indicates the median value of the separation (0.39 pc).

lines (orange for C^{18}O and blue for N_2H^+). Considering the insignificant velocity shift between the C^{18}O and N_2H^+ lines and the lower Mach numbers in dense cores than those in surrounding filaments, turbulence dissipation may have been processed to form the dense cores in the filament.

4.6. Cores in Infalling Motions

One way to diagnose how much the dense cores have evolved is to see whether they are experiencing gas infalling motions that may play a role in enhancing the evolution of the dense cores by helping to condense gaseous material in the cores. Thus, we attempted to search for *blue asymmetries* in the line profile of the optically thick molecular species (Evans 2003). In order to make sure that the asymmetric double-peaked line profile is not coming from multiple velocity components along the line of sight, we need to compare the optically thick line profile with an optically thin line. Since HCO^+ (1–0), which is often used as a tracer of infall motion in molecular clouds, is optically thick (Shimajiri et al. 2017) and H^{13}CO^+ (1–0) is optically thin in the observed region (Aoyama et al. 2001), we searched for infall signatures toward our dense cores using these two isotopologues of HCO^+ .

Figure 23 shows HCO^+ (1–0) and H^{13}CO^+ (1–0) spectra of the two dense cores C18 and C28 over the N_2H^+ (1–0) integrated intensity maps in color tones. The HCO^+ spectra around the bright core region (see central 3×3 spectra) show double-peaked profiles with higher blue peaks (so-called blue profiles), indicating the core is undergoing contraction motions. Cores C13, C14, C25, C26, C27, C29, and C36 also present such blue profiles in HCO^+ (1–0) lines (see Figure 32 in Appendix C). Among them, C18 is the only protostellar dense core. The other eight dense cores are all starless dense cores. The filaments (F6, F13, F17, and F23), which contain nine dense cores presenting infall asymmetry in the HCO^+ (1–0) line profile, are all thermally critical in virial analysis (see Figures 16 and 17).

Figure 24 shows an interesting case where infalling gas motions are seen in HCO^+ (1–0) toward a fragment at H1 region of filament F23, which seems not yet condensed enough to be detected in the N_2H^+ (1–0) line. Probably the gravitationally critical status of its parent filament F23 may be triggering the condensing process toward a fragment to produce a future prestellar core. We may be watching for a moment of very early condensing process before the stage of a prestellar core. Indeed, there are several Herschel robust prestellar cores identified on the high-resolution continuum map in Könyves et al. (2020) (see also Section 4.7). In the cases of H2 and H3, HCO^+ (1–0) spectra do not present any significant infall signatures and there are no Herschel prestellar cores. We think that these may be even younger fragments than H1 and their destinies cannot be determined at this moment.

4.7. Chemical Differentiation in the Dense Cores

Chemical differentiation between the dense gas tracers can also be an important factor in examining how the dense cores evolved. In this section, we discuss how our molecular tracers show different or similar distributions in the dense cores and what the distributions would imply.

In dense cores with relatively low temperature ($T \sim 10\text{--}20$ K), C-bearing molecules (e.g., CO) are easily depleted and the abundance of H_3^+ can be enhanced because of less abundant CO as the main destroyer of H_3^+ . The reaction of H_3^+ with HD can produce gas-phase progenitors of the deuterated species (H_2D^+ , D_2H^+ , and D_3^+) and lead to NH_2D molecule formation from the reaction of the deuterated ions with NH_3 and the dissociative recombination of NH_3D^+ (Lepp et al. 1987; Pagani et al. 1992; Caselli et al. 2003; Sipilä et al. 2015). Moreover, the ammonia molecule is less susceptible to freeze-out onto dust grains than C- or O-bearing molecules. Deuterated ammonia (NH_2D) molecules are especially good in tracing dynamically evolved starless cores (or prestellar cores; see, e.g., Crapsi et al. 2005; Harju et al. 2017) although it has been recently found that NH_2D (as well as ammonia and other volatiles) significantly freezes out in the central few thousands astronomical units of prestellar cores (Caselli et al. 2022; Pineda et al. 2022). Therefore, NH_2D can be used to trace highly evolved starless cores in cold molecular clouds (the critical density of ortho- NH_2D ($1_{11}\text{--}1_{01}$) transition is $6.52 \times 10^4 \text{ cm}^{-3}$ at ~ 10 K; Wienen et al. 2021).

On the other hand, the sulfur monoxide (SO) molecule is proposed to be the most sensitive indicator of the evolutionary status of dense cores and can be used as a tracer of very young cores (Tafalla et al. 2006). Frau et al. (2012) showed that dense cores abundant in oxo-sulfurated (e.g., SO, SO_2) species are in a chemical transitional stage between the less dense cloud and the more evolved dense core. However, note that the molecule SO is well detected in shocks in star-forming regions (see, e.g., Sakai et al. 2014).

Figure 25 presents distributions of SO ($3_2\text{--}2_1$) and ortho- NH_2D ($1_{11}\text{--}1_{01}$) around N_2H^+ dense cores of Orion B. Harju et al. (2020) highlighted that the production of NH_2D is efficient inside the CO-depleted zone, where N_2H^+ is bright. In fact, the ortho- NH_2D ($1_{11}\text{--}1_{01}$) emission is highly confined at the brightest part of N_2H^+ dense cores (see polygons and black contours in Figure 25). In Figure 26, the NH_2D emission also shows a strong correlation at the region with high H_2 column densities. On the other hand, the SO emission is widely

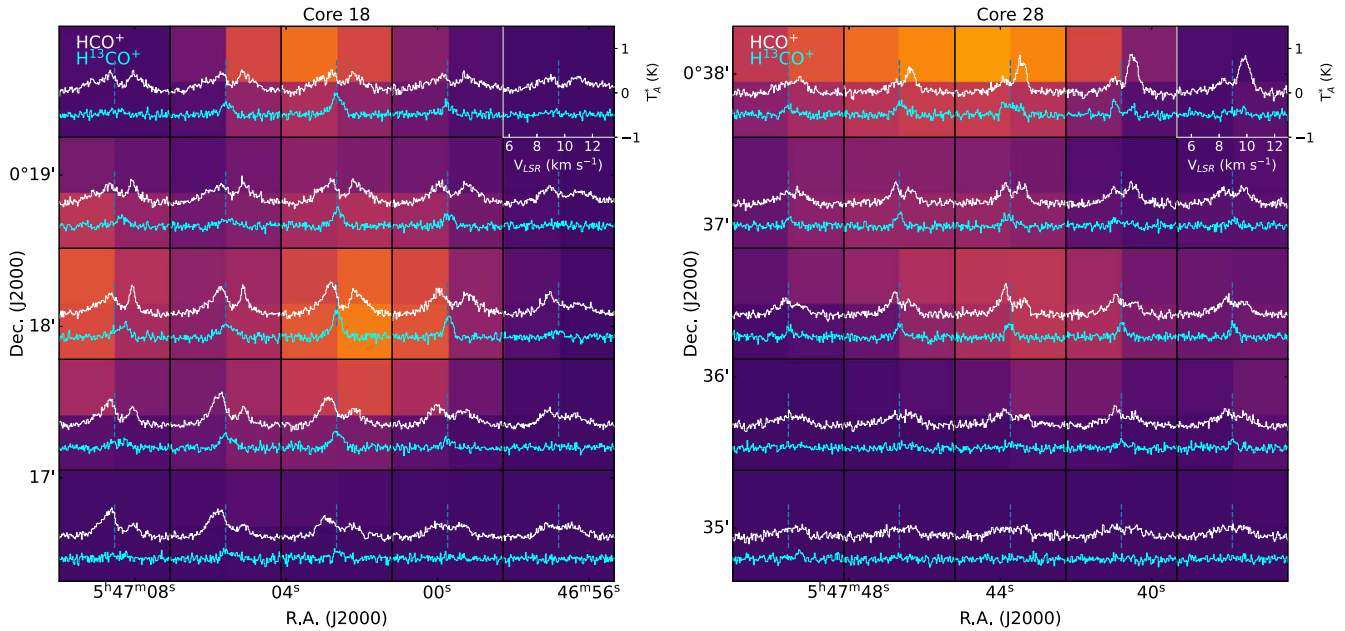


Figure 23. Infall asymmetries appeared in the HCO^+ (1–0) (white) and H^{13}CO^+ (1–0) (cyan) line profiles toward C18 (central 3×3 spectra in left panel) and C28 (central 3×3 spectra in right panel). The color tones in the background indicate the N_2H^+ (1–0) integrated intensity. The dashed blue vertical line at the center indicates the systemic velocity measured from the hyperfine fitting of N_2H^+ (1–0). Each spectrum is the average of the spectra for the 2×2 pixels shown in the background of each spectrum. H^{13}CO^+ (1–0) is shown with an offset of -0.5 K in the y-axis.

distributed from the boundary to the central region of the H_2 column density distribution to its center.

In total, 15 dense cores were detected over 3σ in ortho- NH_2D ($1_{11}-1_{01}$). We call the smaller regions where ortho- NH_2D ($1_{11}-1_{01}$) was detected in the dense core as “ NH_2D bright cores” in particular. Among these NH_2D , 13 NH_2D bright cores were found to coincide with YSOs (Core IDs C1, C2, C3, C4, C5, C7, C8, C9, C10, C12, C15, C16, and C19) and two NH_2D bright cores were identified as starless cores (C14 and C22 in panels (a) and (c) of Figure 25). We note that the NH_2D bright cores are located in filaments F6, F17, F23, and F30, which are all thermally supercritical and have YSOs (see Figures 16 and 17), indicating that the criticality of the filament may have a good correlation with the chemical maturity of its embedded dense cores. In the virial analysis, C14 is gravitationally bound and C22 is marginally in virial equilibrium (see the magenta and cyan circles in the right panel of Figure 18). According to the ortho- NH_2D ($1_{11}-1_{01}$) detection and the gravitationally unstable status by the virial analysis, we suggest that C14 is the most evolved starless dense core in the Orion B cloud and a good candidate site of star formation.

The brightest N_2H^+ core (C1) presents an anticorrelation between the SO (3_2-2_1) and ortho- NH_2D ($1_{11}-1_{01}$) emission (see the panel (b) in Figure 25). Note that the region where the ortho- NH_2D ($1_{11}-1_{01}$) emission is strong tends to contain more YSOs inferring strong star formation activity. This could indicate that in these regions icy mantles, where NH_2D is expected to be mostly adsorbed during the prestellar stage of the core, have been recently sublimated, returning significant fractions of NH_2D into the gas phase (Caselli et al. 2022). The distributions of both SO (3_2-2_1) and ortho- NH_2D ($1_{11}-1_{01}$) emission with multiple contour peaks in C1 show that there are several SO cores around multiple NH_2D cores at the central region of the N_2H^+ core suggesting two possibilities. The first one is that there may be strong chemical differentiation in SO and NH_2D . The second one is that active star formation

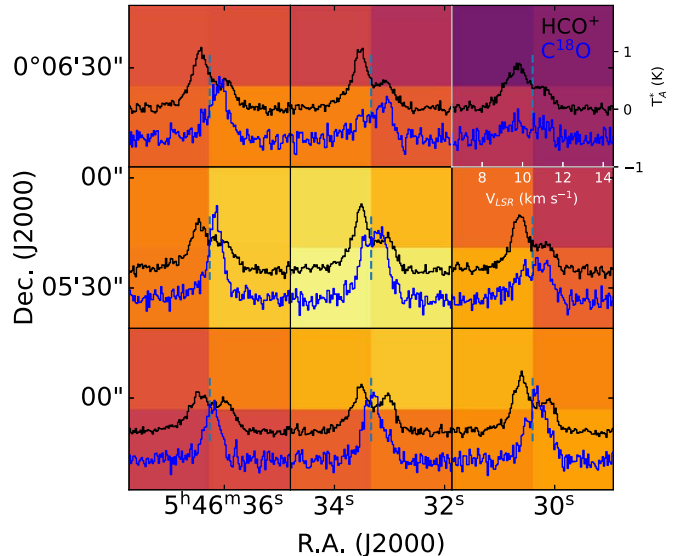


Figure 24. Infall asymmetries shown HCO^+ (1–0) (black) and C^{18}O (1–0) (blue) line profiles at the region of H1 marked in Figure 21. Each line profile is the average of the spectra for the 2×2 pixels shown in the background of each spectrum. The background color scale indicates the C^{18}O (1–0) integrated intensity. The baselines of HCO^+ (1–0) and C^{18}O (1–0) are set to be zero and -0.5 K, respectively.

unresolved with our current resolution may have been undergoing inside the region. Indeed, SO is copiously formed in shock regions (where icy mantles are sputtered) and it is used as a tracer of accretion shocks (Sakai et al. 2014).

The different distribution between NH_2D and SO is also remarkably seen in the bulk cloudy region in the southernmost part of the cloud, where N_2H^+ dense cores (C2, C4, and C5) are embedded. This region has been named LBS23 in the CS molecular survey (Lada et al. 1991) and is known to contain HH objects such as HH24, HH25, and HH26 (Herbig 1974;

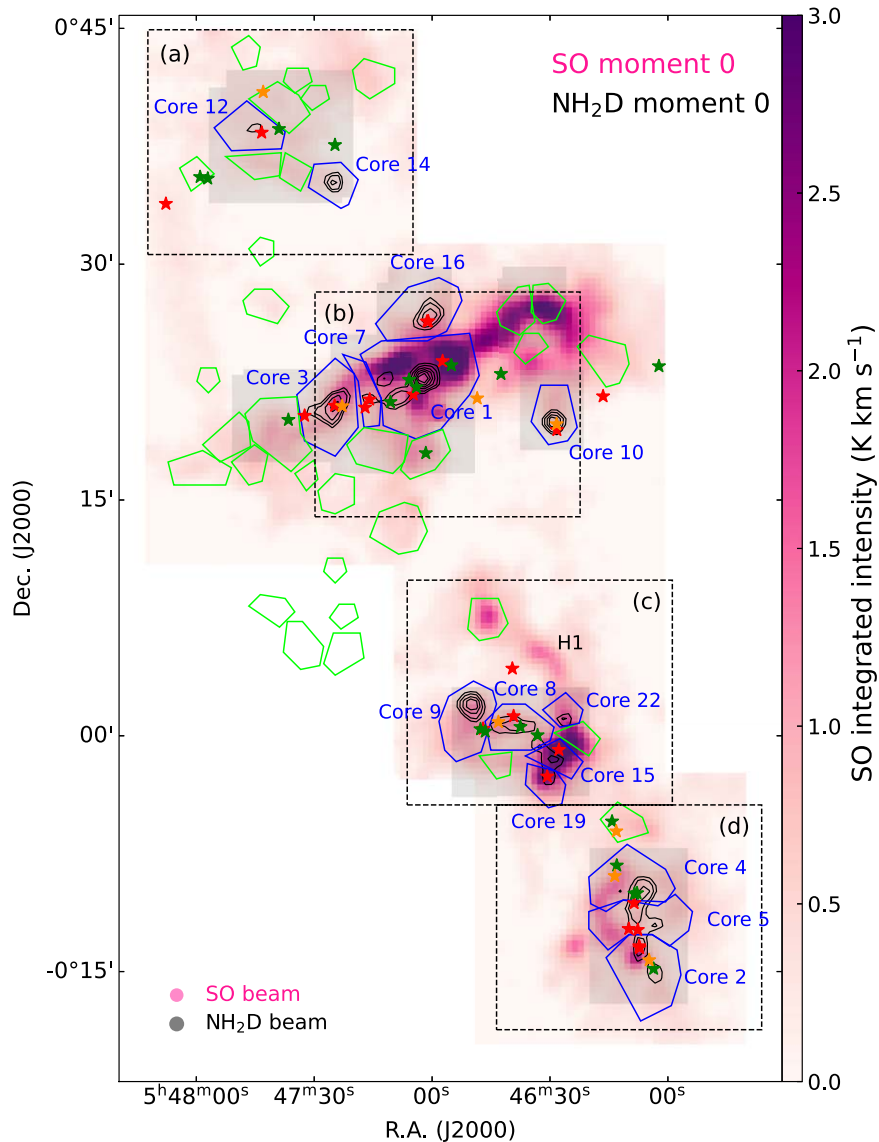


Figure 25. The distributions of SO and NH_2D in N_2H^+ dense cores. The integrated intensities of SO (3_2-2_1) and ortho- NH_2D ($1_{11}-1_{01}$) are shown in magenta color tones and black contours with levels of $0.031 \text{ K km s}^{-1} \times [3, 5, 8, 11, 14, 17]$, respectively. N_2H^+ dense cores are drawn in blue or green depending on whether NH_2D is detected or not detected. Small gray shaded areas indicate the ortho- NH_2D ($1_{11}-1_{01}$) observed regions. The YSOs from Furlan et al. (2016) are shown with asterisk symbols (red for Class 0 protostars, green for Class I protostars, and orange for flat-spectrum YSOs). Core names are labeled only for NH_2D detected dense cores. Boxes drawn with dashed lines with labels (a)–(d) are the regions of close-up views in Figure 26.

Matthews & Little 1983). In Figure 26(d), the distribution of ortho- NH_2D ($1_{11}-1_{01}$) in the region shows a good correlation with H_2 column density, while SO (3_2-2_1) emission shows a distinct arc-like feature with an offset to the east side from the main distribution of ortho- NH_2D ($1_{11}-1_{01}$).

We found bright SO emission in some regions where NH_2D and N_2H^+ lines were not detected. For example, we find bright SO emission at the position of the fragment H1 where there is no detection of NH_2D and N_2H^+ lines (see panel (c) in Figure 25) implying that it is chemically very young. Because of the infall signatures detected here as shown in Figure 24 and the chemical youth inferred from the bright SO emission, the fragment H1 seems to be still gathering material.

Moreover, in Figure 26 we compare distributions of the Herschel H_2 column density, our NH_2D and SO emissions, YSOs (Furlan et al. 2016), and Herschel prestellar cores (Könyves et al. 2020). Since the angular resolution of Herschel data is about three times higher, some column density

enhancements can be explained by the local fragmentation, which cannot be seen in our observing resolution.

To demonstrate chemical differentiation, we present the averaged integrated intensities of dense cores in N_2H^+ ($1-0$) and SO (3_2-2_1), and ortho- NH_2D ($1_{11}-1_{01}$) lines as a function of H_2 column density in Figure 27. The integrated intensities and H_2 column densities were averaged within the TRA0 beam size ($\theta_B \sim 52''$ for SO (3_2-2_1)) at the emission peak positions. Starless dense cores are marked with red circles. From the virial analysis, we divide them into gravitationally bound (red filled circle) and gravitationally unbound (red open circle). The dense cores having positional coincidence with YSOs are indicated with blue star symbols and they are all found to be gravitationally bound in virial analysis. The left and middle panels in Figure 27 show that N_2H^+ emission and SO emission tends to be stronger at high H_2 column density regions as also seen in the emission distribution of N_2H^+ and SO in Figure 26(a)–(c).

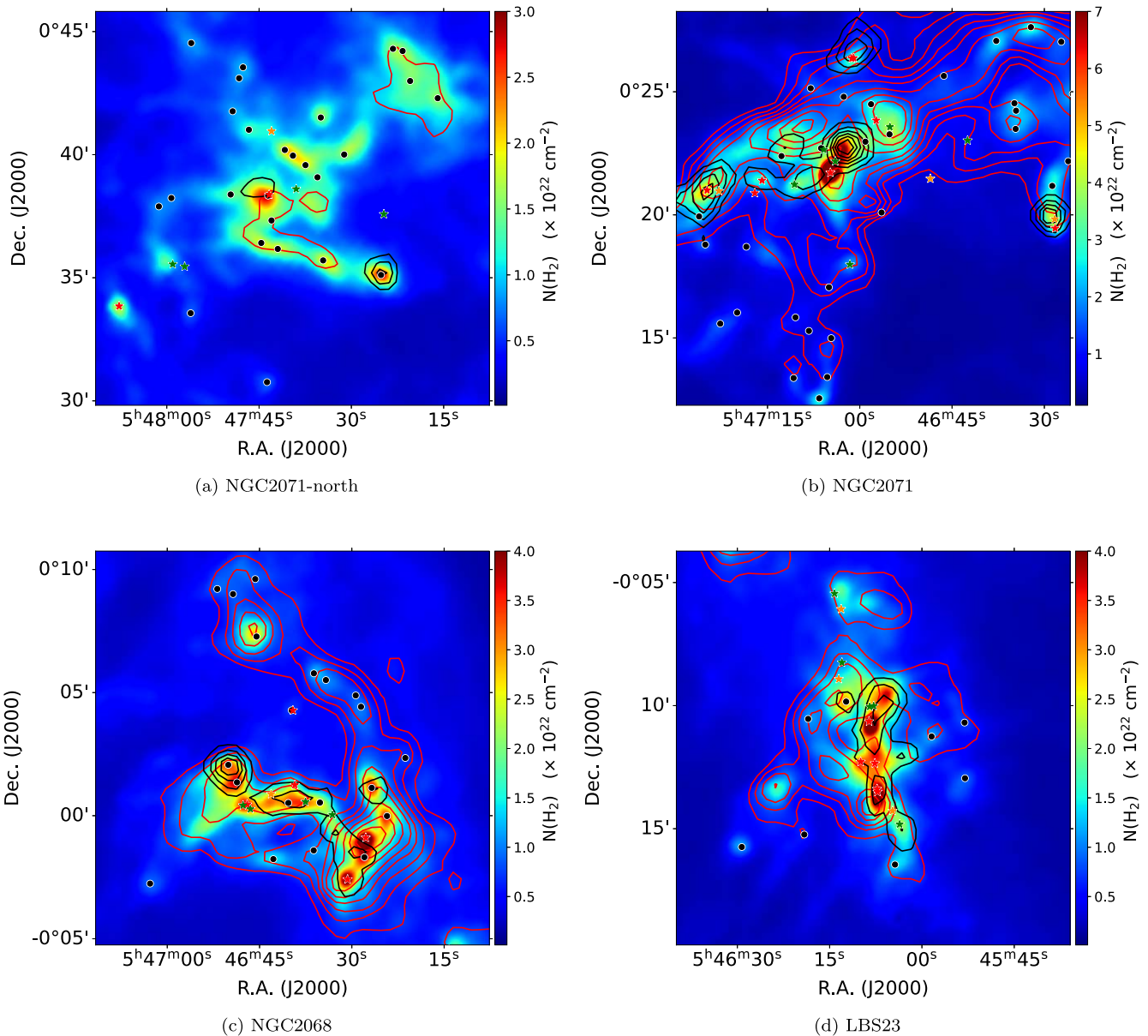


Figure 26. Zoom-in distribution of SO and NH₂D in Orion B. The integrated intensities of ortho-NH₂D ($1_{11}-1_{01}$) and SO (3_2-2_1) lines are shown in black and red contours, respectively. The background color tones represent the H₂ column density distribution (Arzoumanian et al. 2019; Könyves et al. 2020). The contour levels for NH₂D data are $0.031 \text{ K km s}^{-1} \times [2, 5, 8, 11, 14, 17]$ and those for SO data are $0.036 \text{ K km s}^{-1} \times [15, 22, 30, 40, 50, 65, 80, 95]$. The H₂ column density level in the background is indicated in the color bar. The YSOs from Furlan et al. (2016) are shown with asterisk symbols (red for Class 0 protostars, green for Class I protostars, and orange for flat-spectrum YSOs). Black circles denote the Herschel robust prestellar cores presented in Könyves et al. (2020).

Understanding the chemical behavior in NH₂D is more complicated. Recently, Caselli et al. (2022) presented the first evidence that NH₂D is almost totally frozen within the central 2000 au of the prestellar core and showed that ortho-NH₂D ($1_{11}-1_{01}$) line emission is not reproducible by the chemical models without NH₂D depletion at the central region. In their study, the frozen NH₂D preserves its chemical composition until it is in the protostellar stage and can be released back into the gas phase to the neighborhood of protostellar objects or shocked region. That may explain the limited detection of NH₂D found in dense cores with YSOs (blue stars in Figure 27), due to the poor angular resolution of the present observations. In prestellar cores (red circles and red arrows in Figure 27), NH₂D intensity could indeed be too faint to be detected and the line profile could be too narrow to be resolved by our moderate spectral resolution, so that the line profile can be also affected by spectral dilution. As NH₂D,

SO will be depleted onto dust grain surfaces and return back to the gas phase when the ice sublimates or to shocked regions (e.g., at the centrifugal radius, as explained by Sakai et al. 2014, or along the outflow). However, unlike NH₂D, SO can also be present in the more extended and less dense material surrounding the dense cores, where sulfur is not yet heavily frozen onto dust grains (e.g., Spezzano et al. 2017; Laas & Caselli 2019; Lattanzi et al. 2020).

Further detailed analysis and discussion on the chemical differentiation are beyond the scope of this paper and will be given in a future study of chemical tracers at higher angular/spectral resolutions.

4.8. Implications of the Survey on Star Formation

The primary aim of TRAO-FUNS survey is to obtain the velocity distribution of low-dense filaments and their dense cores for the study of their formation mechanism. Since the observed

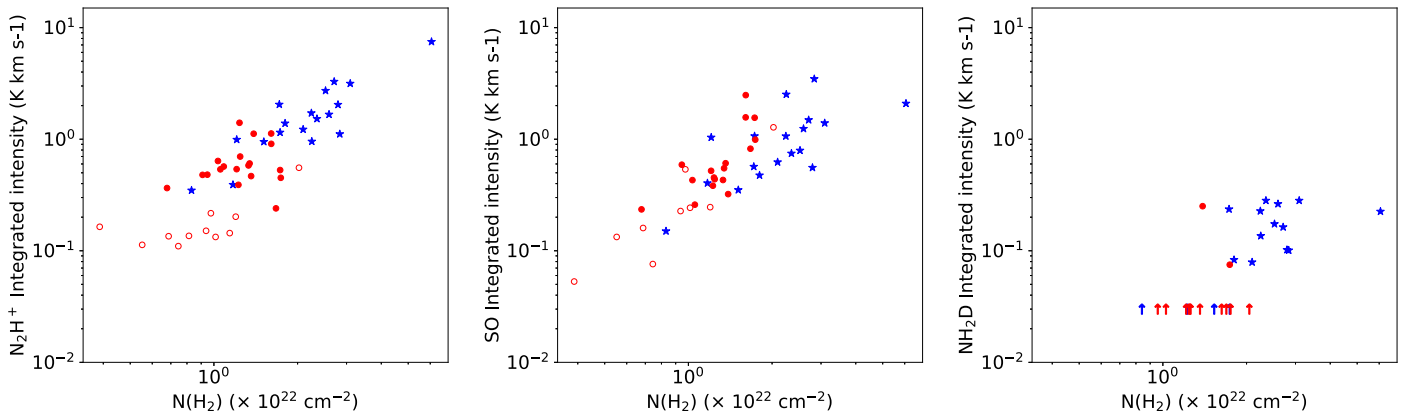


Figure 27. Averaged integrated intensities of three molecular lines (N_2H^+ , SO, and NH_2D) for dense cores as a function of H_2 column density measured with TRAO beam size at the N_2H^+ emission peak position. Blue stars and filled red and open red circles indicate gravitationally bound dense cores with YSOs, prestellar cores, and gravitationally unbound starless dense cores, respectively. Dense cores with (blue) and without (red) YSOs, where NH_2D emission is undetected in our sensitivity, are marked with arrows as the upper limit (rms level at NH_2D integrated intensity map).

three-dimensional PPV data can trace the multiple line-of-sight components in velocity, it provides a much more comprehensive understanding of the velocity-coherent structures in a molecular cloud. As part of the series, previous reports on L1478 in the California molecular cloud (Chung et al. 2019) and IC 5146 (Chung et al. 2021) successfully identified velocity-coherent structures (filaments) and dense cores, and derived their physical properties. Results on the relation between the filament’s criticality and the existence of dense cores for low-mass star-forming molecular cloud L1478 and low- to intermediate-mass star-forming cloud IC 5146 showed that the majority of dense cores are located in the supercritical filaments. The results shown in the high-mass star-forming region Orion B are also found to be consistent with these molecular clouds in previous studies. Therefore, the supercriticality of a filament is supposed to be a necessary condition for the formation of dense cores regardless of the physical environment of all of the clouds.

The second goal of the survey is to understand the kinematic effect of the surrounding filaments on the dense core formation. Based on the nonthermal velocity dispersions obtained from C^{18}O (1–0) and N_2H^+ (1–0) transitions in three series (Chung et al. 2019, 2021 and this study), the observational evidence that the nonthermal velocity dispersions of dense cores are smaller than those of filaments may indicate the dissipation of turbulence during core formation, which supports the colliding scenario in the formation of dense cores in the cloud proposed by Padoan et al. (2001).

Lastly, the survey is designed to investigate the chemical properties of both filaments and dense cores, especially the chemical differentiation between them. Since the early series on L1478, IC 5146, and Orion B focused on the identification of filaments and dense cores and the derivation of physical properties, the chemical understanding will be developed in the next series of papers.

Table 4 summarizes the representative physical properties of the three molecular clouds of the TRAO-FUNS survey that have been analyzed so far. The filament widths of two sources (L1478 and Orion B) at the distances of about 400 pc are smaller than the filament width of IC 5146 at the distance of ~ 700 pc ($W \sim 0.2\text{--}0.7$ pc). That is a similar result to what has recently been reported on the effect of distance on the filament widths (Panopoulou et al. 2022). They show a trend that the mean width of filaments depends on not only the distance of the molecular clouds but also the angular resolution. Note that the widths in

Table 4
Comparison of the Properties of Molecular Clouds Observed by the TRAO-FUNS Project

Property	L1478	IC 5146	Orion B
(1) Distance	450	600–800	423
(2) Width	0.08–0.19	0.18–0.67	0.05–0.26
(3) Fil#	10	14	30
(4) Core#	8	22	48
(5) YSO#	3	40	51
(6) $\langle\sigma_{\text{tot}}\rangle$	0.18–0.31	0.28–0.43	0.31–0.54
(7) $\langle N(\text{H}_2)\rangle$	7–40	22–88	28–145

Note. Refer to Chung et al. (2019, 2021) for the details on scientific results on L1478 and IC 5146, respectively. (1) Distance to the molecular cloud adopted in units of parsecs. (2) Measured widths of filaments in units of parsecs. (3) Number of identified C^{18}O (1–0) filaments. (4) Number of identified N_2H^+ (1–0) dense cores. (5) Number of YSOs associated with the filaments. (6) Total velocity dispersion of filaments measured from C^{18}O (1–0) in units of kilometers per second. (7) Average H_2 column densities of the identified filaments in units of 10^{20} cm^{-2} .

TRAO-FUNS studies are measured from the Gaussian FWHM of the mean radial profile and not corrected for the beam convolution effect. The beam size is also larger than the Herschel data used in Panopoulou et al. (2022). Moreover, André et al. (2022) revisited the issue and argued that the typical width of 0.1 pc in filamentary structures of nearby molecular clouds is a true common scale. We will carefully discuss this in a future study, after analyzing more targets observed on the TRAO-FUNS survey using the same measurement to estimate the filament width.

Table 4 indicates that as the mean H_2 column density of filaments in the molecular cloud increases (in the order of L1478, IC 5146, and Orion B), the numbers of identified filaments, N_2H^+ (1–0) dense cores, and YSOs associated with filaments tend to increase. Similar results are reported by Hacar et al. (2018) who showed that active high-mass star-forming molecular clouds are higher in H_2 number density and have more supercritical fibers than less active low-mass star-forming molecular clouds. The results in those works also indicate that the star-forming activity of a cloud is closely related to the number of filaments and dense cores and essentially to its H_2 density. Moreover, the total velocity dispersion measured from decomposed C^{18}O (1–0) spectrum also increases as the mean H_2 column density increases being consistent with the relation

between the total velocity dispersion and column density (refer to Figure 6 in Arzoumanian et al. 2013).

The forthcoming studies on molecular clouds with various physical environments observed by our TRAO-FUNS survey (e.g., Polaris flare, Taurus, Perseus, Serpens, Aquila) will be helpful to verify the tentative conclusion and to understand the environmental effect on the properties of filaments. Further studies for these clouds using our chemical tracers (e.g., ortho-NH₂D (1₁₁-1₀₁), SO (3₂-2₁), N₂H⁺ (1-0)) will expand our understanding of the evolutionary stages of filaments and dense cores in various star-forming regions.

5. Summary

This paper presents the results of mapping observations of the NGC 2068 and NGC 2071 regions of the Orion B molecular cloud in multiple molecular lines performed with the TRAO 14 m telescope to study the filamentary structures in the clouds and their roles in the formation of dense cores. Our results are summarized as follows:

1. Many of the observed C¹⁸O (1-0) spectra in the clouds are shown to contain multiple velocity components and decomposed into an individual velocity component with a Gaussian fit. This allowed us to identify filaments with similar velocities, so-called velocity-coherent filaments, using the FoF algorithm. A total of 30 filaments were extracted, and their physical properties such as length, width, column density, and mass, were measured. The longest filament is found to have a length of ~ 6.5 pc and the median length for the entire sample of the filaments is 0.8 pc. The median value of the filament widths is estimated to be 0.1 pc with a range of 0.05–0.26 pc. The H₂ column densities of the filaments range from 2.8×10^{21} to 1.4×10^{22} cm⁻². The filament mass is calculated to be in the range of 4 and 842 M_{\odot} with a median of 38 M_{\odot} .
2. We identified 48 N₂H⁺ dense cores using the FellWalker algorithm, and estimated the core masses and virial masses to examine the dynamical state. From the virial analysis for these dense cores, all dense cores with YSOs and half of the starless dense cores are found to be in gravitational bound status.
3. The distributions of the nonthermal velocity dispersions extracted from N₂H⁺ (1-0) and C¹⁸O (1-0) show that the dense cores are found to be mostly in transonic/subsonic motions while their natal filaments are in supersonic nonthermal velocity dispersions (excepting parts of the region in F17b). This may indicate that gas turbulent motions in the filaments around dense cores have been dissipated at the core scale to help form the dense cores in their surrounding filaments.
4. The filaments with N₂H⁺ dense core are mostly found to be gravitationally bound, thermally supercritical, and thus under environments in which dense cores can be formed well. The filaments with larger $M_{\text{line}}/M_{\text{line}}^{\text{th,crit}}$ tend to have more dense cores the majority of which tend to contain YSOs. Therefore, it is well understood that the criticality of the filament can be a key condition for its fragmentation and the formation of dense cores/YSOs in the filament.
5. From a case study for a filament F23, a filament might be forming dense cores in a process of longitudinal fragmentation, in the sense that its mass is far higher

than its thermal critical line mass, and its fragments are quasiperiodically located along the filament with an average of 0.39 pc which is comparable to its theoretical value (four times of the filament width: 0.52 pc) predicted in the gravitational collapse in an isothermal filament considering uncertain factors in its calculation such as the inclination of the filament.

6. We identified infall signatures in at least nine N₂H⁺ dense cores using the observations of HCO⁺ (1-0) and H¹³CO⁺ (1-0), finding that their parent filaments are all in the gravitationally critical status. This may imply that a gravitationally unstable environment in the filaments should help to enhance the evolution of the dense cores to finally form stars there. We find a fragment H1, which is not detected in N₂H⁺ but shows infall signatures over the fragment. It is believed to be in a very early condensation process before the stage of a prestellar core, but not yet enough condensed to be detected with N₂H⁺ (1-0) line, again leading us to believe that the *fertile* environment in the filament is helping produce a future prestellar core.
7. We examined how molecular tracers (NH₂D and SO) are differentiated in the N₂H⁺ dense cores and how this chemical differentiation is related to the physical status of their parent filaments. We find that the NH₂D emission is strongly correlated with the H₂ column density and is usually well detected in the central regions of the N₂H⁺ cores. We find that 13 out of 15 NH₂D bright cores are forming YSOs. These may indicate that NH₂D traces the most evolved status of the dense cores while SO does the least evolved status of the dense cores. It is found that these NH₂D cores are all located in the thermally supercritical filaments, indicating that the criticality of filaments may play a key role in the chemical maturity of dense cores.

Acknowledgments

The authors are grateful to the anonymous referee for the detailed and constructive comments, which helped improve this paper. This work was supported by the Basic Science Research Program through the National Research Foundation of Korea (NRF) funded by the Ministry of Education, Science and Technology (NRF-2019R1A2C1010851), and by the Korea Astronomy and Space Science Institute grant funded by the Korea government (MSIT) (Project No. 2023-1-84000). H.Y. is supported by the Basic Science Research Program through the National Research Foundation of Korea (NRF) funded by the Ministry of Education (NRF-2021R1A6A3A01087238). E.J.C. is supported by the Basic Science Research Program through the National Research Foundation of Korea (NRF) funded by the Ministry of Education (NRF-2022R1I1A1A01053862). S.K. is supported by the National Research Council of Science & Technology (NST)—Korea Astronomy and Space Science Institute (KASI) Postdoctoral Research Fellowship for Young Scientists at KASI in South Korea. T.L. acknowledges supports from the National Key R&D Program of China (No. 2022YFA1603101); the National Natural Science Foundation of China (NSFC), through grants No. 12073061 and No. 12122307; the international partnership program of the Chinese Academy of Sciences, through grant No. 114231KYSB20200009; and the Shanghai Pujiang Program 20PJ1415500.

Appendix A

All Identified C¹⁸O Filaments in the NGC 2068 and NGC 2071 Regions of Orion B and an Analysis of Their Physical Quantities

The online figure set associated with Figure 28 presents the physical properties of each velocity-coherent filament and some schematic methods used to derive some of them. The figure set shows the atlas of filaments identified using the decomposed C¹⁸O (1–0) data. The atlas figure of each filament contains nine panels as follows:

- Distribution of the integrated intensity of a filament.
- Distribution of the systemic velocity of a filament.
- Distribution of the velocity dispersion of a filament.
- Determination of the spine of a filament and radial cuts for deriving radial profiles. Red dots indicate the path of the spine and the cyan curve is the smoothed path that is used for deriving the length and width of the filament. The black lines display radial cuts that are perpendicular to the smoothed spine and are used for drawing radial profiles in panel (e).
- Radial profiles of the intensity along the black lines drawn in panel (d). Black and red thick lines show the averaged profile and its Gaussian-fit result, respectively.
- The distribution of the YSOs and the dense cores over the filament. The filament is depicted with its integrated intensity distribution in color. The gray contours indicate the

- N₂H⁺ (1–0) integrated intensity distribution with contour levels of [0.08, 0.3, 0.8, 2.0, 4.0, 6.0, 8.0, 10.0] K km s⁻¹. The N₂H⁺ dense cores were identified from the FellWalker algorithm. The cyan and green polygon shapes are to indicate the dense cores to be and not to be associated with their surrounding filament, respectively. The asterisks are the YSOs classified in Furlan et al. (2016). Red: Class 0 protostars. Green: Class I protostars. Yellow: flat-spectrum YSOs. Note that the coordinate scales given in this panel are the same as the cases for panels (a)–(d). The red arrow shows the direction measured along the spine of the filament for the variations of integrated intensity, velocity centroid, and nonthermal velocity dispersion given in panels (g)–(i).
- The variation of the integrated intensity along the spine of the filament.
 - The variation of the velocity centroid along the spine of the filament.
 - The variation of the nonthermal velocity dispersion divided by the speed of sound along the spine of the filament. The orange and blue dots are estimated from C¹⁸O (1–0) (for filament) and N₂H⁺ (1–0) (for dense cores), respectively. The inset depicts the number distribution of the nonthermal velocity dispersion with histograms of the same color codes for the filament and cores as those for dots. The vertical blue lines indicate a representative position of the dense cores.

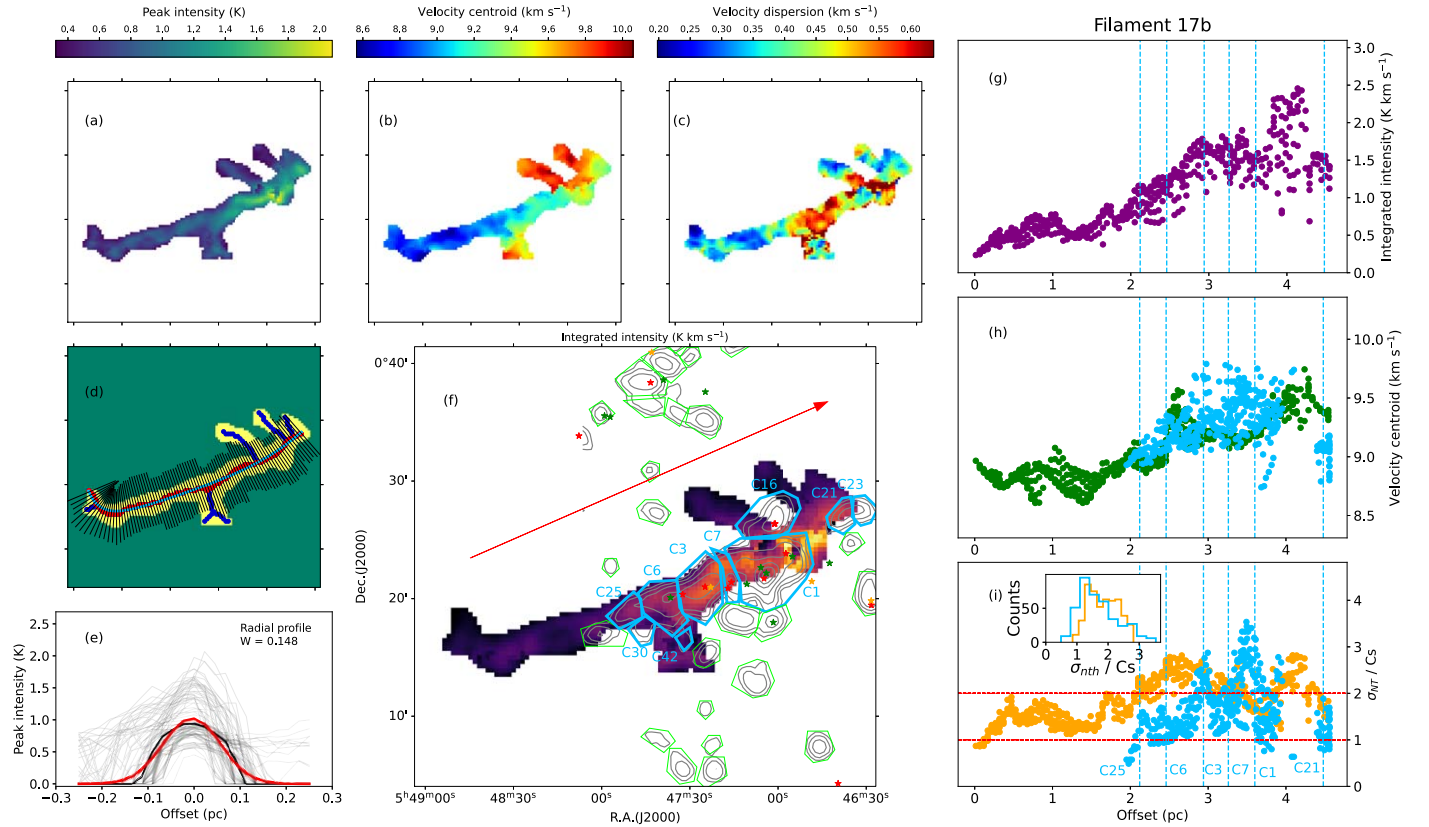


Figure 28. Physical quantities of filament F17b as described in Appendix A. The complete figure set (32 images) is available in the online journal. (The complete figure set (32 images) is available.)

Appendix B

Distribution of N_2H^+ Dense Cores with Respect to $C^{18}O$ Filaments

Here we present supplementary information on the filaments and the 48 N_2H^+ dense cores. Figure 29 shows the distribution of filaments identified from $C^{18}O(1-0)$ and

the N_2H^+ cores described with $N_2H^+(1-0)$ integrated intensity image.

Figure 30 provides a comparison between the $C^{18}O$ spectrum and N_2H^+ spectrum at the position of each dense core to explore the relation between LSR velocities of filamentary structure and that of dense cores along the line of sight. The complete atlas is available as a figure set in the online journal.

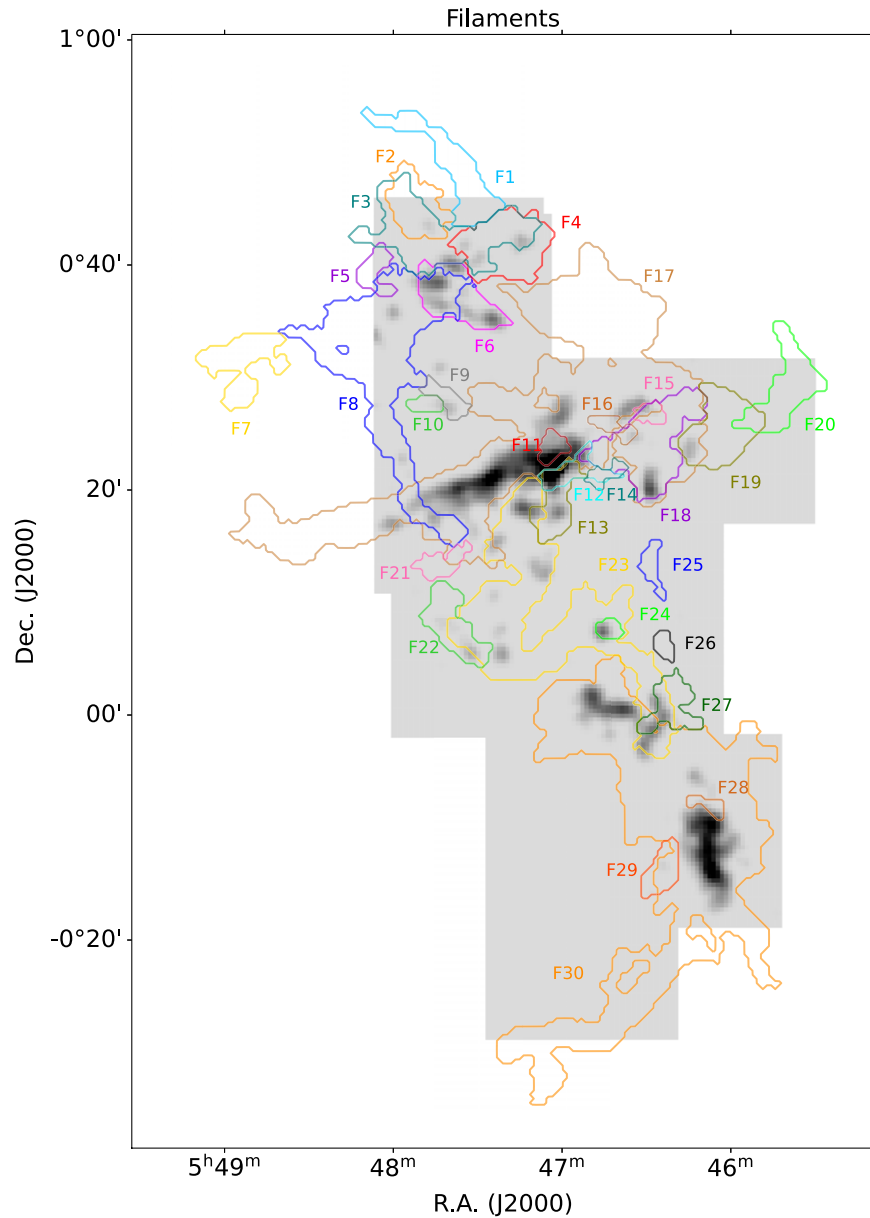


Figure 29. Distribution of filaments and the N_2H^+ cores. The contours in various colors are the same as the filaments presented in Figure 7(a) and the shaded box and gray tones indicate the N_2H^+ observed region and $N_2H^+(1-0)$ integrated intensity.

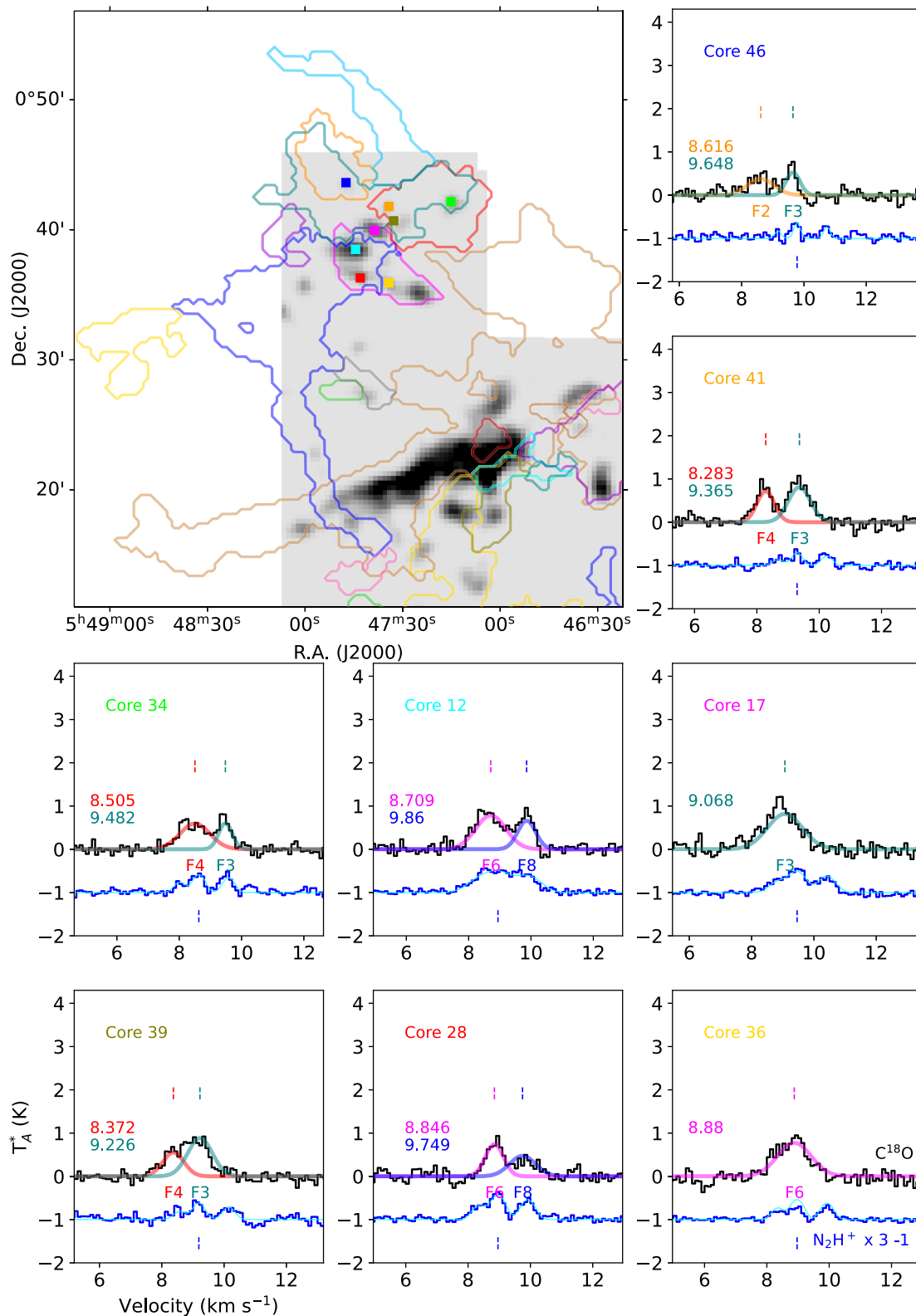


Figure 30. The spectra for the filaments and dense cores. The top-left panel displays the distribution of the filaments (colored contour lines) and the positions of the dense cores (colored square symbols) on the N_2H^+ (1-0) integrated intensity map (grayscale). Eight small panels show the C^{18}O (1-0) spectra (upper black line) at the position of the peak intensity of the dense cores and averaged N_2H^+ profiles (lower blue line) for the dense cores. We multiplied 3 for the N_2H^+ spectrum with -1 K offset for visualization. The color codes of filaments in the top-left panel correspond to those for the decomposed C^{18}O line profile and the filament name in the small panels. The positions of velocity centroids of each decomposed profile are marked with small vertical dashed lines and numbers above the profile. The filament IDs are shown below the profile. The hyperfine structure fit result of N_2H^+ (1-0) is drawn on its profile with a cyan line. The complete figure set (6 images) is available in the online journal.

(The complete figure set (6 images) is available.)

Appendix C CS, HCO⁺, C¹⁸O, H¹³CO⁺, and N₂H⁺ Line Spectra for 48 Dense Cores

We present the distributions of HCO⁺ (1–0), H¹³CO⁺ (1–0), and CS (2–1) in Figure 31 and the averaged spectra of CS (2–1), HCO⁺ (1–0), C¹⁸O (1–0), H¹³CO⁺ (1–0), and N₂H⁺ (1–0) lines for dense cores in Figure 32. As for the CS line, we could not find any significant infall signature toward dense

cores in this study, although the CS line is known to be one of the best infall tracers (Lee et al. 1999, 2001).

Figure 32 shows CS (2–1), HCO⁺ (1–0), C¹⁸O (1–0), H¹³CO⁺ (1–0), and N₂H⁺ (1–0) molecular line profiles for 48 dense cores. All the profiles shown here are the average ones for the spectra over the dense core. We do not present spectra of several dense cores if the transition is not observed or the observed emission has $S/N < 3$. The core names are labeled on the top of each panel.

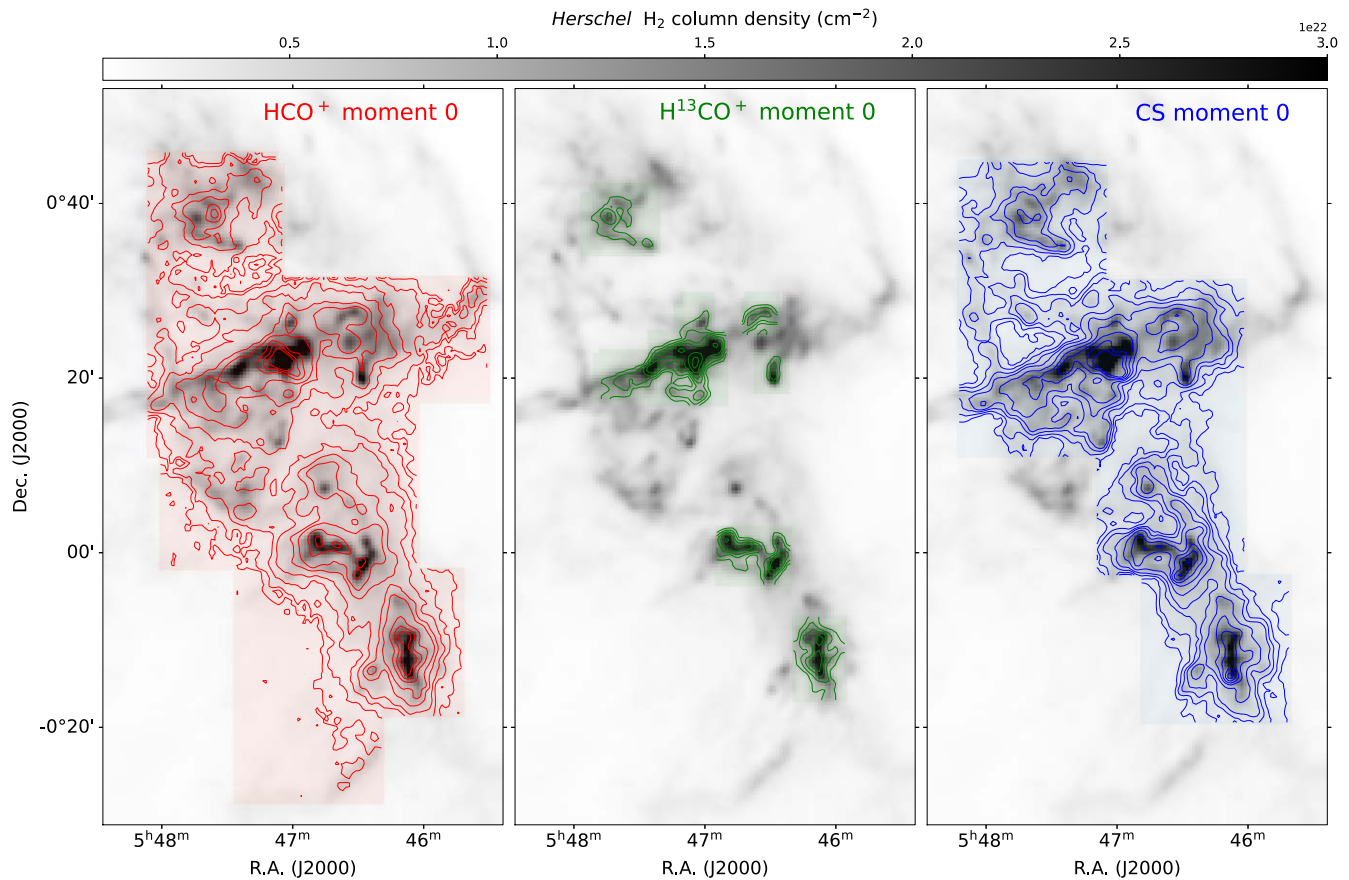


Figure 31. The integrated intensity maps of HCO⁺ (1–0) (red), H¹³CO⁺ (1–0) (green), and CS (2–1) (blue) lines. The contour levels for HCO⁺ (1–0) are $0.041 \text{ K km s}^{-1} \times [5, 10, 15, 20, 30, 40, 70, 100, 130]$, those for H¹³CO⁺ (1–0) are $0.026 \text{ K km s}^{-1} \times [5, 8, 13, 18, 25, 30, 40]$, and those for CS (2–1) are $0.037 \text{ K km s}^{-1} \times [5, 10, 15, 20, 30, 45, 60, 80, 100]$. The grayscale and color-shaded regions in the background indicate Herschel H₂ column density distribution and observing regions for each line, respectively.

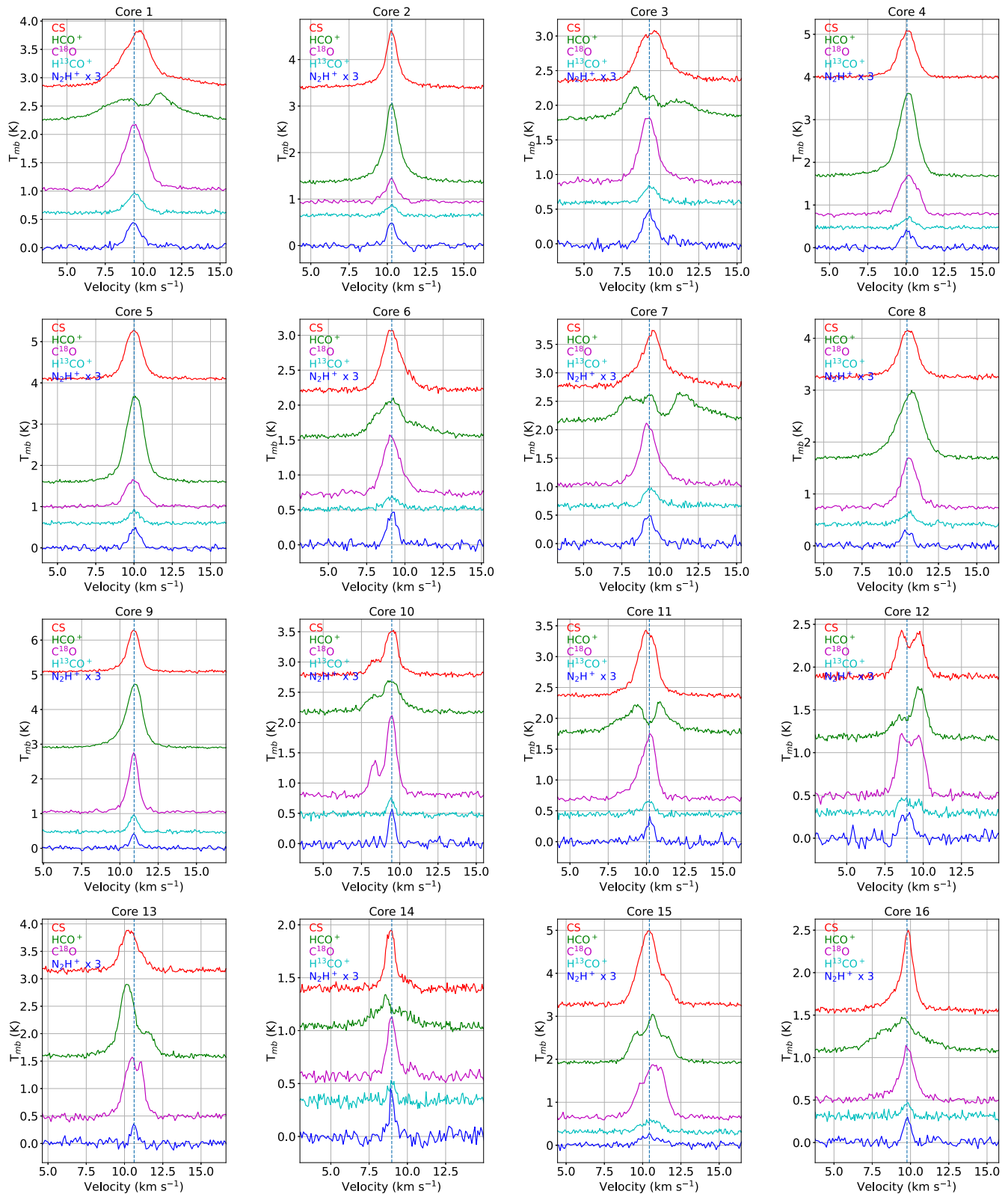


Figure 32. CS (2–1), HCO⁺ (1–0), C¹⁸O (1–0), H¹³CO⁺ (1–0), and the isolated hyperfine component of N₂H⁺ (1–0) line profiles of dense cores. All the profiles shown here are the average ones for the spectra over the dense core. The vertical dashed line is the systemic velocity obtained from N₂H⁺ hyperfine fitting.

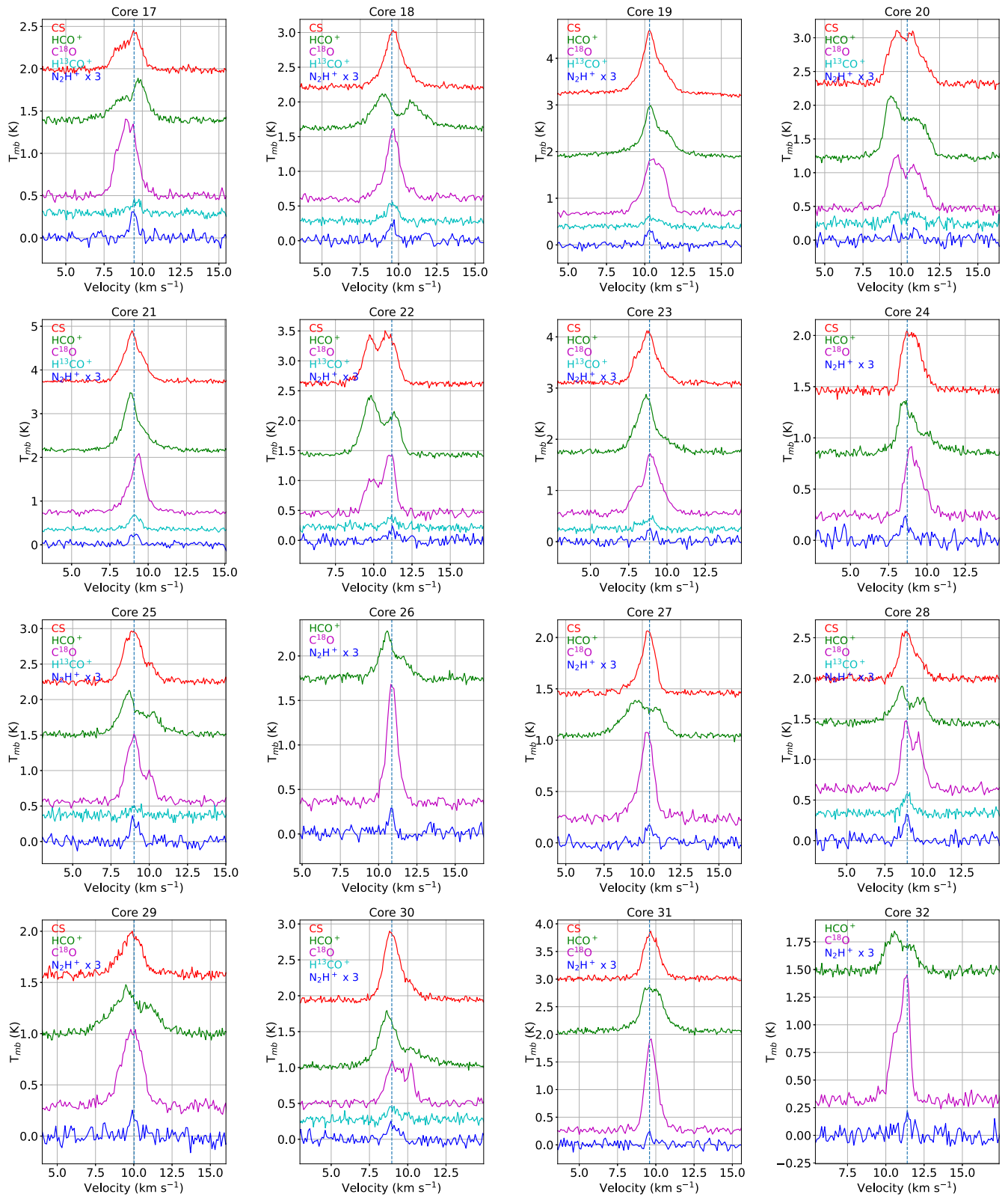


Figure 32. (Continued.)

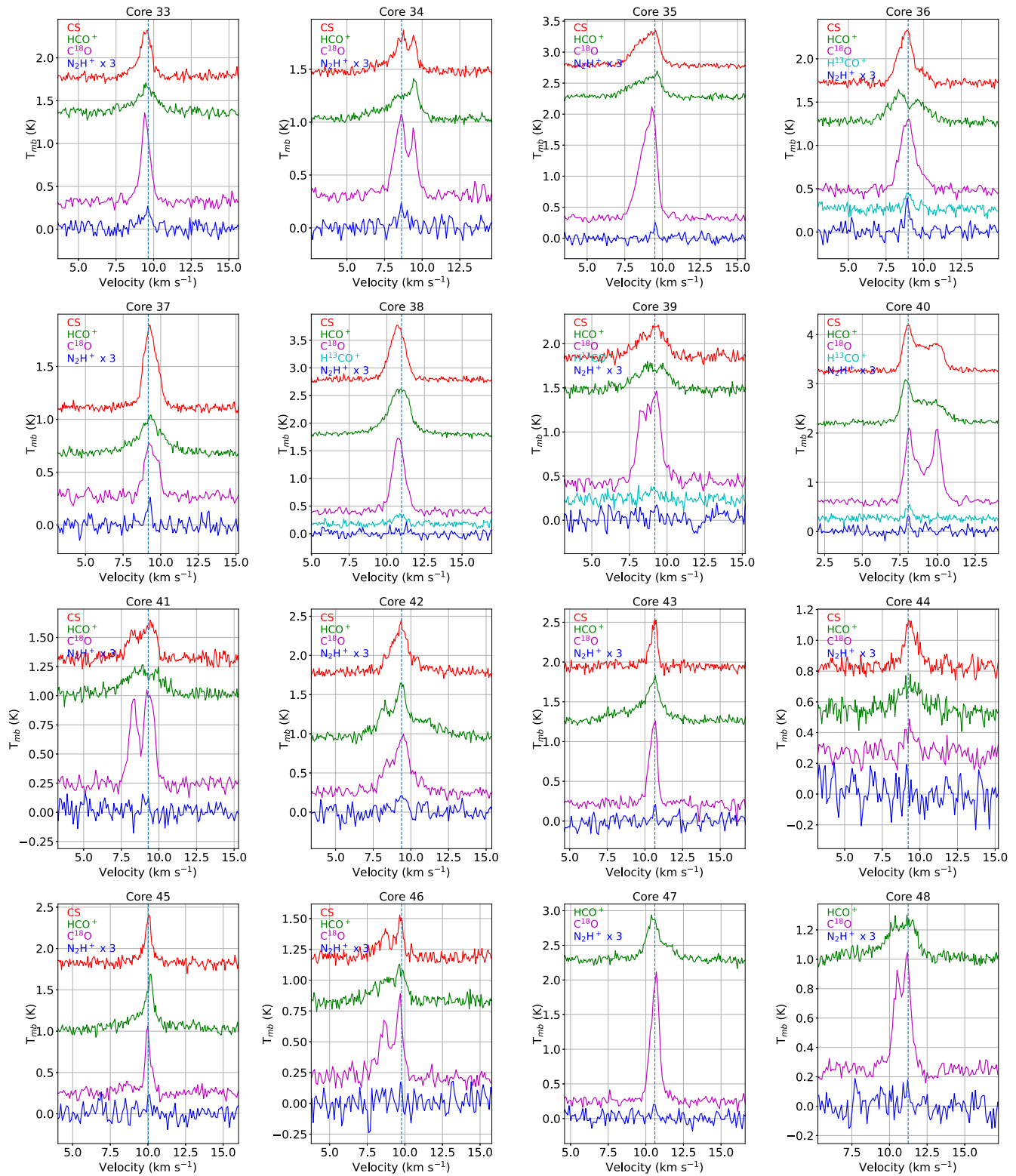


Figure 32. (Continued.)

ORCID iDs

Hyunju Yoo <https://orcid.org/0000-0002-8578-1728>
 Chang Won Lee <https://orcid.org/0000-0002-3179-6334>
 Eun Jung Chung <https://orcid.org/0000-0003-0014-1527>
 Shinyoung Kim <https://orcid.org/0000-0001-9333-5608>
 Mario Tafalla <https://orcid.org/0000-0002-2569-1253>

Paola Caselli <https://orcid.org/0000-0003-1481-7911>
 Philip C. Myers <https://orcid.org/0000-0002-2885-1806>
 Kyoung Hee Kim <https://orcid.org/0000-0001-9597-7196>
 Tie Liu <https://orcid.org/0000-0002-5286-2564>
 Woojin Kwon <https://orcid.org/0000-0003-4022-4132>

Archana Soam  <https://orcid.org/0000-0002-6386-2906>
 Jongsoo Kim  <https://orcid.org/0000-0002-1229-0426>

References

- André, P., Francesco, J. D., Ward-Thompson, D., et al. 2014, in *Protostars and Planets VI*, ed. H. Beuther et al. (Tucson, AZ: Univ. Arizona Press)
- André, P., Men'shchikov, A., Bontemps, S., et al. 2010, *A&A*, **518**, L102
- André, P. J., Palmeirim, P., & Arzoumanian, D. 2022, *A&A*, **667**, L1
- Aoyama, H., Mizuno, N., Yamamoto, H., et al. 2001, *PASJ*, **53**, 1053
- Arzoumanian, D., André, P., Didelon, P., et al. 2011, *A&A*, **529**, L6
- Arzoumanian, D., André, P., Könyves, V., et al. 2019, *A&A*, **621**, A42
- Arzoumanian, D., André, P., Peretto, N., & Könyves, V. 2013, *A&A*, **553**, A119
- Ballesteros-Paredes, J., Hartmann, L. W., Vázquez-Semadeni, E., Heitsch, F., & Zamora-Avilés, M. A. 2011, *MNRAS*, **411**, 65
- Bally, J. 2008, in *Handbook of Star Forming Regions, Volume I: The Northern Sky*, ed. B. Reipurth (San Francisco, CA: ASP), 459
- Bally, J., Langer, W. D., Wilson, R. W., Stark, A. A., & Pound, M. W. 1991, in *IAU Symp. 147, Fragmentation of Molecular Clouds and Star Formation* (Cambridge: Cambridge Univ. Press), 11
- Berry, D. 2015, *A&C*, **10**, 22
- Berry, D. S., Reinhold, K., Jenness, T., & Economou, F. 2007, in *ASP Conf. Ser. 376, Astronomical Data Analysis Software and Systems XVI*, ed. R. A. Shaw, F. Hill, & D. J. Bell (San Francisco, CA: ASP), 425
- Bertoldi, F., & McKee, C. F. 1992, *ApJ*, **395**, 140
- Blum, H. 1967, in *Models for Perception of Speech and Visual Form*, ed. W. Wathen-Dunn (Cambridge, MA: MIT Press)
- Buckle, J. V., Curtis, E. I., Roberts, J. F., et al. 2010, *MNRAS*, **401**, 204
- Caselli, P., Benson, P. J., Myers, P. C., & Tafalla, M. 2002, *ApJ*, **572**, 238
- Caselli, P., Pineda, J. E., Sipilä, O., et al. 2022, *ApJ*, **929**, 13
- Caselli, P., van der Tak, F. F. S., Ceccarelli, C., & Bacmann, A. 2003, *A&A*, **403**, L37
- Chung, E. J., Lee, C. W., Kim, S., et al. 2019, *ApJ*, **877**, 114
- Chung, E. J., Lee, C. W., Kim, S., et al. 2021, *ApJ*, **919**, 3
- Crapsi, A., Caselli, P., Walmsley, C. M., et al. 2005, *ApJ*, **619**, 379
- Evans, Neal 2003, in *SFChem 2002: Chemistry as a Diagnostic of Star Formation*, ed. L. F. Curry & M. Fich (Ottawa: NRC Press), 157
- Fiege, J. D., & Pudritz, R. E. 2000, *MNRAS*, **311**, 105
- Frau, P., Girart, J. M., Beltrán, M. T., et al. 2012, *ApJ*, **759**, 3
- Frerking, M. A., Langer, W. D., & Wilson, R. W. 1982, *ApJ*, **262**, 590
- Furlan, E., Fischer, W. J., Ali, B., et al. 2016, *ApJS*, **224**, 5
- Garden, R. P., Hayashi, M., Gatley, I., Hasegawa, T., & Kaifu, N. 1991, *ApJ*, **374**, 540
- Gibb, A. G. 2008, in *Handbook of Star Forming Regions, Volume I: The Northern Sky*, ed. B. Reipurth (San Francisco, CA: ASP), 693
- Gómez, G. C., & Vázquez-Semadeni, E. 2014, *ApJ*, **791**, 124
- Gritschneider, M., Heigl, S., & Burkert, A. 2017, *ApJ*, **834**, 202
- Großschedl, J. E., Alves, J., Meingast, S., & Herbst-Kiss, G. 2021, *A&A*, **647**, A91
- Hacar, A., & Tafalla, M. 2011, *A&A*, **533**, A34
- Hacar, A., Tafalla, M., Forbrich, J., et al. 2018, *A&A*, **610**, A77
- Hacar, A., Tafalla, M., Kauffmann, J., & Kovács, A. 2013, *A&A*, **554**, A55
- Hanawa, T., Kudoh, T., & Tomisaka, K. 2017, *ApJ*, **848**, 2
- Hanawa, T., Nakamura, F., Matsumoto, T., et al. 1993, *ApJL*, **404**, L83
- Harju, J., Daniel, F., Sipilä, O., et al. 2017, *A&A*, **600**, A61
- Harju, J., Pineda, J. E., Vasyunin, A. I., et al. 2020, *ApJ*, **895**, 101
- Herbig, G. H. 1974, *LicOB*, **658**, 1
- HGBS Team 2020, *Herschel Gould Belt Survey, IPAC*
- Ikeda, N., Kitamura, Y., & Sunada, K. 2009, *ApJ*, **691**, 1560
- Inutsuka, S.-I., & Miyama, S. M. 1992, *ApJ*, **388**, 392
- Jeong, I.-G., Kang, H., Jung, J., et al. 2019, *JKAS*, **52**, 227
- Johnstone, D., Fich, M., Mitchell, G. F., & Moriarty-Schieven, G. 2001, *ApJ*, **559**, 307
- Kauffmann, J., Bertoldi, F., Bourke, T. L., Evans, N. J., & Lee, C. W. 2008, *A&A*, **487**, 993
- Kauffmann, J., Pillai, T., & Goldsmith, P. F. 2013, *ApJ*, **779**, 185
- Kirk, H., Francesco, J. D., Johnstone, D., et al. 2016, *ApJ*, **817**, 167
- Kirk, H., Johnstone, D., & Tafalla, M. 2007, *ApJ*, **668**, 1042
- Koch, E. W., & Rosolowsky, E. W. 2015, *MNRAS*, **452**, 3435
- Könyves, V., André, P., Arzoumanian, D., et al. 2020, *A&A*, **635**, A34
- Könyves, V., André, P., Men'shchikov, A., et al. 2015, *A&A*, **584**, A91
- Kutner, M. L., Tucker, K. D., Chin, G., & Thaddeus, P. 1977, *ApJ*, **215**, 521
- Laas, J. C., & Caselli, P. 2019, *A&A*, **624**, A108
- Lada, E. A., Bally, J., & Stark, A. A. 1991, *ApJ*, **368**, 432
- Lattanzi, V., Bizzocchi, L., Vasyunin, A. I., et al. 2020, *A&A*, **633**, A118
- Lee, C. W., Myers, P. C., & Tafalla, M. 1999, *ApJ*, **526**, 788
- Lee, C. W., Myers, P. C., & Tafalla, M. 2001, *ApJS*, **136**, 703
- Lepp, S., Dalgarno, A., & Sternberg, A. 1987, *ApJ*, **321**, 383
- Lovas, F. J. 2004, *JPCRD*, **33**, 177
- MacLaren, I., Richardson, K. M., & Wolfendale, A. W. 1988, *ApJ*, **333**, 821
- Maddalena, R. J., Moscowitz, J., Thaddeus, P., & Morris, M. 1986, *ApJ*, **303**, 375
- Mathews, N., & Little, L. T. 1983, *MNRAS*, **205**, 123
- Megeath, S. T., Gutermuth, R., Muzerolle, J., et al. 2012, *AJ*, **144**, 192
- Men'shchikov, A., André, P., Didelon, P., et al. 2010, *A&A*, **518**, L103
- Menten, K. M., Reid, M. J., Forbrich, J., & Brunthaler, A. 2007, *A&A*, **474**, 515
- Mitchell, G. F., Johnstone, D., Moriarty-Schieven, G., Fich, M., & Tothill, N. F. H. 2001, *ApJ*, **556**, 215
- Molinari, S., Swinyard, B., Bally, J., et al. 2010, *A&A*, **518**, L100
- Motte, F., André, P., Ward-Thompson, D., & Bontemps, S. 2001, *A&A*, **372**, L41
- Müller, H. S. P., Thorwirth, S., Roth, D. A., & Winnewisser, G. 2001, *A&A*, **370**, L49
- Myers, P. C. 2009, *ApJ*, **700**, 1609
- Myers, P. C., Ladd, E. F., & Fuller, G. A. 1991, *ApJL*, **372**, L95
- Nakamura, F., Hanawa, T., & Nakano, T. 1993, *PASJ*, **45**, 551
- Nishimura, A., Tokuda, K., Kimura, K., et al. 2015, *ApJS*, **216**, 18
- Ohashi, S., Sanhueza, P., Chen, H.-R. V., et al. 2016, *ApJ*, **833**, 209
- Orkisz, J. H., Peretto, N., Pety, J., et al. 2019, *A&A*, **624**, A113
- Padoan, P., Juvella, M., Goodman, A. A., & Nordlund, A. 2001, *ApJ*, **553**, 227
- Pagani, L., Salez, M., & Wannier, P. G. 1992, *A&A*, **258**, 479
- Panopoulou, G. V., Clark, S. E., Hacar, A., et al. 2022, *A&A*, **657**, L13
- Pattle, K., Ward-Thompson, D., Kirk, J. M., et al. 2015, *MNRAS*, **450**, 1094
- Peretto, N., Fuller, G. A., Duarte-Cabral, A., et al. 2013, *A&A*, **555**, A112
- Pety, J., Guzmán, V. V., Orkisz, J. H., et al. 2017, *A&A*, **599**, A98
- Pickett, H., Poynter, R., Cohen, E., et al. 1998, *JQSRT*, **60**, 883
- Pineda, J. E., Harju, J., Caselli, P., et al. 2022, *AJ*, **163**, 294
- Polychroni, D., Schisano, E., Elia, D., et al. 2013, *ApJL*, **777**, L33
- Ramírez-Galeano, L., Ballesteros-Paredes, J., Smith, R. J., Camacho, V., & Zamora-Avilés, M. 2022, *MNRAS*, **515**, 2822
- Roueff, A., Gerin, M., Gratier, P., et al. 2020, *A&A*, **645**, A26
- Sakai, N., Sakai, T., Hirota, T., et al. 2014, *Natur*, **507**, 78
- Schneider, N., André, P., Könyves, V., et al. 2013, *ApJL*, **766**, L17
- Shimajiri, Y., André, P., Braine, J., et al. 2017, *A&A*, **604**, A74
- Shimajiri, Y., André, P., Ntormousi, E., et al. 2019, *A&A*, **632**, A83
- Shimajiri, Y., Kitamura, Y., Saito, M., et al. 2014, *A&A*, **564**, A68
- Shirley, Y. L. 2015, *PASP*, **127**, 299
- Sipilä, O., Harju, J., Caselli, P., & Schlemmer, S. 2015, *A&A*, **581**, A122
- Spezzano, S., Caselli, P., Bizzocchi, L., Giuliano, B. M., & Lattanzi, V. 2017, *A&A*, **606**, A82
- Tafalla, M., & Hacar, A. 2015, *A&A*, **574**, A104
- Tafalla, M., Santiago-García, J., Myers, P. C., et al. 2006, *A&A*, **455**, 577
- Vázquez-Semadeni, E., Gómez, G. C., Jappsen, A. K., et al. 2007, *ApJ*, **657**, 870
- Virtanen, P., Gommers, R., Oliphant, T. E., et al. 2020, *NatMe*, **17**, 261
- Walker-Smith, S. L., Richer, J. S., Buckle, J. V., et al. 2013, *MNRAS*, **429**, 3252
- Wang, K., Zhang, Q., Wu, Y., & Zhang, H. 2011, *ApJ*, **735**, 64
- Wareing, C. J., Pittard, J. M., Falle, S. A. E. G., & Loo, S. V. 2016, *MNRAS*, **459**, 1803
- Wienen, M., Wyrowski, F., Walmsley, C. M., et al. 2021, *A&A*, **649**, A21
- Wilson, B. A., Dame, T. M., Mashedier, M. R. W., & Thaddeus, P. 2005, *A&A*, **430**, 523
- Zhang, G.-Y., André, P., Men'shchikov, A., & Wang, K. 2020, *A&A*, **642**, A76
- Zucker, C., Speagle, J. S., Schlafly, E. F., et al. 2019, *ApJ*, **879**, 125